

12-2018

A Remote Observatory for Geocoronal Hydrogen Emissions

Margaret A. Gallant

Follow this and additional works at: <https://commons.erau.edu/edt>



Part of the [Electrical and Computer Engineering Commons](#)

Scholarly Commons Citation

Gallant, Margaret A., "A Remote Observatory for Geocoronal Hydrogen Emissions" (2018). *Dissertations and Theses*. 427.

<https://commons.erau.edu/edt/427>

This Thesis - Open Access is brought to you for free and open access by Scholarly Commons. It has been accepted for inclusion in Dissertations and Theses by an authorized administrator of Scholarly Commons. For more information, please contact commons@erau.edu.

A REMOTE OBSERVATORY FOR GEOCORONAL HYDROGEN
EMISSIONS

BY
MARGARET A. GALLANT

A Thesis
Submitted to the Department of
Electrical, Computer, Software, and Systems Engineering
In partial fulfillment of the requirements
for the degree of
Master of Science in Electrical and Computer Engineering

12/2018
Embry-Riddle Aeronautical University
Daytona Beach, Florida

© Copyright by Margaret A. Gallant 2018
All Rights Reserved

A REMOTE OBSERVATORY FOR GEOCORONAL HYDROGEN
EMISSIONS

by

Margaret A. Gallant

This thesis was prepared under the direction of the candidate's Thesis Committee Co-Chairs Dr. Edwin Mierkiewicz, Associate Professor, and Dr. William Barott, Professor, and Thesis Committee Member, Dr. Brian Butka, Associate Professor, and has been approved by the Thesis Committee. It was submitted to the Department of Electrical, Computer, Software, and Systems Engineering in partial fulfillment of the requirements of the degree of Master of Science in Electrical and Computer Engineering

THESIS COMMITTEE:



Dr. Edwin Mierkiewicz,
Committee Co-Chair



Dr. William Barott,
Committee Co-Chair



Dr. Brian Butka,
Committee Member



Dr. Jianhu Liu,
Graduate Program Chair,
Electrical and Computer Engineering



Dr. Tim Wilson,
Department Chair,
ECSSE



Dr. Maj Mirmirani,
Dean, College of Engineering



Lon Moeller,
Senior V.P. for Academic Affairs

Acknowledgments

I would not have gotten through this without the guidance of my research advisor, Ed Mierkiewicz, who gave me the blank canvas and the paintbrush but did not tell me how or what to paint nor in which cabinet the paint might be located. I especially thank Ed for his kindness and encouragement and for showing me, by example, how to be a fantastic mentor. Thanks, also, to Ron Oliveresen for being a mentor and a friend and for always encouraging my adventurous side. The lessons I learned while observing and doing research with these two have been invaluable to me.

Many, many thanks to the folks at the UW-Madison Astronomy department for answering our many phone calls and help desk inquiries. Very special thanks to Kurt Jaehnig and Jeff Percival, the genius engineering duo that make this and many other projects possible and fun to work on. Lots of gratitude to the wonderful Susan Nossal and the wise Fred Roesler; without their encouragement, I would not have pursued the scientific path that I did. The unwavering kindness I received from all of you has been truly appreciated.

Thank you to the many friends and family members who have offered their understanding and patience throughout my academic career. Special thanks to Rebecca Griffith for being a fiercely loyal friend and for helping me find creative ways to conquer self-doubt and negativity. I would like to particularly thank the Embry-Riddle Amateur Astronomy Club for providing an outlet for and fueling my curiosity, and I would like to thank the many professors at Embry-Riddle who challenged me to give them my very best effort.

I would not have stood a fighting chance in academia without the lessons my parents bestowed me. Thank you to the strongest woman I know, my mother, Libby

Gallant, for showing me how to be both tenacious and warmhearted and how to make allies instead of enemies. Thank you to my father, Thom Gallant, for helping me with my grade school science projects and igniting a curiosity for the natural world; in many ways, you were my first research advisor.

Finally, I thank my partner in life, crime, and just-trying-to-figure-out-what-to-eat-everyday, Donald Bennett, for his endless support in all of my endeavors, practical or otherwise, and for making me the best grilled cheese sandwiches on both the difficult days and the celebratory ones.

Contents

Acknowledgments	iv
List of Tables	x
List of Figures	xi
Abstract	xiv
List of Acronyms	xv
List of Symbols	xvii
1 Significance of Geocoronal Hydrogen	1
1.1 Thesis Objectives	3
1.2 Getting Started with Atmospheric Physics	3
1.2.1 An Isothermal Atmosphere in Hydrostatic Equilibrium	5
1.2.2 Addressing the Isothermal Assumption	8
1.3 An Explanation on Exospheres	12
1.4 Signatures of Hydrogen	14
1.4.1 Airglow	14
1.4.2 Charge Exchange	16
1.4.3 Mass Spectroscopy	16
1.5 A History of Hydrogen Observations	17
1.6 The INSpIRE Observatory	21

2	Observing Methodology	23
2.1	Geocoronal Observations 101	23
2.1.1	Viewing Geometry	24
2.1.2	Instrument Calibration	25
2.1.3	Annular Summing Technique	27
2.2	Fabry-Perot Interferometry	28
2.3	Tuning the Wavelength with Pressure	35
3	Observatory Systems	38
3.1	System Overview	38
3.2	Control Computer & Software	42
3.3	Uninterruptible Power Supply	43
3.4	AstroHaven Clamshell Dome	45
3.5	Siderostat Control System	48
3.5.1	Siderostat	49
3.5.2	Control Board	50
3.5.3	Environmental Sensors	51
3.6	Fabry-Perot Interferometer	54
3.6.1	Lens Mount	56
3.6.2	Camera Mount	58
3.7	Pressure Control System	58
3.8	Charge Coupled Devices	61
3.8.1	Andor iKon-M934	62
3.8.2	SBIG STF-8300M	63
3.8.3	Astrovid StellaCam-EX	64
4	Observatory Control Software	66
4.1	Overview	66
4.2	A Crashcourse in LabVIEW Terminology	67
4.2.1	Event Driven Interfaces (EDI)	68
4.2.2	Non-Reentrancy	68
4.2.3	Functional Global Variable Clusters (FGVC)	68

4.3	INSpIRE Launchpad	70
4.3.1	Widget Accessibility	70
4.3.2	Automatic Logging	72
4.3.3	Power Outage Monitoring	73
4.3.4	Observatory Shutdown	74
4.4	Hardware Control & Monitoring	74
4.4.1	Environment Monitor Widget	74
4.4.2	Siderostat Control Widget	76
4.4.3	Dome Control Widget	80
4.4.4	Pressure Control Widget	83
4.5	Detector Control	86
4.5.1	Image Display	87
4.5.2	Autosave	89
4.5.3	Data Header Population	90
4.5.4	Andor iKon-M934 Widget	91
4.5.5	SBIG STF-8300M Widget	95
4.5.6	Astrovid Feed	97
4.6	Observing Tools	98
4.6.1	Cluster Widget	98
4.6.2	Scripting Widget	98
4.6.3	Tuner Widget	102
5	System Testing and Future Procedures	108
5.1	First Light: Imaging the Moon	109
5.2	Fabry-Perot Interferometer Fringe Imaging	111
5.3	FPI on the Sky	115
5.4	Remote Testing	115
6	A Case Study on INSpIRE Capabilities	117
6.1	From Spectral Data to Balmer- α Intensity	118
6.2	Radiative Transport Modeling	121
6.3	Model-Data Comparison	122

6.3.1	Seasonal Trend in H- α Intensity Predictions	124
6.3.2	Data Selected	128
6.3.3	Results	129
6.3.4	Implications	135
6.4	Recommendations	140
6.4.1	Assessing Current Models	141
6.4.2	Interhemispheric Collaboration	141
7	Conclusions	144
7.1	Summary of Development	144
7.1.1	Future Expansions of Remote Operations	145
7.2	Summary of Scientific Contributions: Achieved and Expected	146
7.2.1	Recommended Data Collection Strategies for INSpIRE	147
	Bibliography	148
	A Requirements for Remote Operations	155
	B Test Actions	162
	C Sample Header (FIRSTLIGHT.fits)	174

List of Tables

3.1	Necessary Python Modules	42
3.2	UPS Serial Communications Summary	44
3.3	Dome Serial Communications Summary	47
3.4	Summary of Omega Engineering Sensors	52
3.5	PCS Serial Communications Summary	60
4.1	Scripting Actions	100
6.1	lyao_rt + NRLMSISE-00 Model Inputs	126
6.2	2000-2001 Balmer- α Observing Conditions	127

List of Figures

1.1	Layers of the Atmosphere	4
1.2	Models of Temperature	9
1.3	Atmospheric Temperature given Solar Heating	10
1.4	Hydrogen in Hydrostatic Equilibrium	11
1.5	Atomic Hydrogen Energy Levels	15
1.6	Geocoronal Image from the Apollo 16 Far UV Camera/Spectrograph	19
2.1	Fringe to Spectra: Ring Summing	24
2.2	Shadow Altitude	25
2.3	Fabry-Perot Etalons	29
2.4	Fabry-Perot Transmission Function	31
2.5	Dual Etalon Fabry-Perot Transmission	34
2.6	Deviation of N_2 from an Ideal Gas	37
3.1	Image of the INSpIRe Trailer	39
3.2	Cut-out Diagram of the INSpIRe Trailer	39
3.3	INSpIRe Data Communications Diagram	41
3.4	INSpIRe Power Supply Diagram	41
3.5	Dome Motor and Pulleys	46
3.6	Dome Belt Attachment Diagram	46
3.7	Siderostat Control System Block Diagram	49
3.8	Siderostat Diagram and Image	50
3.9	Environmental Sensors Placement	51
3.10	WindSonic Ultrasonic Anemometer	53

3.11 PBO-FPI Optical Trace	55
3.12 The INSpIRe Low-Resolution Etalon	56
3.13 Lens Mount Design	57
3.14 Camera Mount Design	58
3.15 Pressure Control System Racks	59
3.16 Andor FPI Fringe Imager	63
3.17 SBIG and Astrovid Guide Cameras	64
4.1 Function Global Variable Cluster	69
4.2 INSpIRe Launchpad	71
4.3 Widget State Diagram	72
4.4 Daily Summary Report Sample	73
4.5 Environment Monitor Widget	75
4.6 Siderostat Control Widget	77
4.7 Dome Control Widget	81
4.8 Dome Open/Closed States	81
4.9 Pressure Control Widget (Indicators Panel)	83
4.10 Pressure Control Widget (Plots Panel)	84
4.11 New Pressure Target Flow	85
4.12 Image Display Widget	87
4.13 Row/Column Plot Widget	88
4.14 FITS File Header Display	89
4.15 Autosave Dialog	90
4.16 Andor iKon-M934 Widget	93
4.17 Andor Exposure Settings Dialog	94
4.18 SBIG Camera Control Widget	96
4.19 SBIG Exposure Settings Dialog	97
4.20 Cluster Widget	99
4.21 Scripting Widget	101
4.22 Tuning Widget	102
4.23 Tune Settings Dialog	103

4.24	Ringsum Viewer	104
4.25	Optimized Pressure Plot	105
4.26	Ring Center Tool	106
5.1	First Light Image of the Moon	110
5.2	Single Etalon Fringes	112
5.3	Dual Etalon Fringe	113
5.4	Preliminary Tune Testing	114
6.1	Line Profile Statistics	118
6.2	Intensity vs. Shadow Altitude	119
6.3	Diurnal Intensity Trend	120
6.4	Lyao_rt Model Flowchart	122
6.5	Model Adjustments to Time, SZA, Latitude, and Longitude	123
6.6	Modeled Seasonal Intensity Trend	125
6.7	Selected Intensity Data from Pine Bluff Observatory, 2000-2001	130
6.8	Observed-to-MSIS Ratio over Shadow Altitude	131
6.9	Diurnal Difference over Shadow Altitude	132
6.10	Seasonal Trend in Low Shadow Altitude Intensity	134
6.11	Lyao_rt Inputs	138
6.12	Correlation between Intensity and Density	139
6.13	Interhemispheric Intensity	142

Abstract

The Investigating Near Space Interaction Regions (INSpIRe) observatory is an adaptable research facility that is designed to use Fabry-Perot interferometer (FPI) to study the faint Balmer series emissions of the terrestrial upper thermosphere and exosphere, collectively known as the geocorona. This instrumentation is designed to be deployable to a clear-air site, necessitating remote operations of the entire observatory, including control and monitoring. The facility currently employs a siderostat to allow for pointing at sky targets, a pressure-tuned dual-etalon FPI to allow for high spectral resolution ($R \sim 80,000$) measurements, and several charge-coupled device (CCD) imagers for guiding and collecting data. The environment is fully monitored using temperature, humidity, barometric pressure, and wind sensors. The INSpIRe observatory's primary purpose is to conduct a long timeline observing campaign that will contribute to three major areas of geocoronal research: geocoronal physics, structure/coupling, and variability.

After reviewing the theories and history of geocoronal research, an explanation of the observational methodology used in studying hydrogen via FPI is described. The systems design and remote operations software implementation is outlined. Significant progress has ensued since development began in 2014. The basic requirements of remote operations have been completed for a minimum of one FPI, including automatic logging, science data header population, and scripting capabilities. Full remote testing is currently incomplete. Strategies for future implementations and testing are included.

A case study is presented on an original model-data comparison of seasonal trends in Balmer- α emission intensity diurnal variation. This investigation serves as a

demonstration of the scientific contributions that the INSpIRE observatory is capable of providing and shows, for the first, a seasonal trend in the evening-to-morning variation of H- α intensity. Observed diurnal asymmetry from a previously established dataset is found to be highest in the winter and lowest in the summer for the Northern hemisphere during solar maximum. Comparisons between modeled and observed diurnal intensity variation, generated using the Lyman Atmospheric Observations Radiative Transport (lyao_rt) code of *Bishop* [1] and employing the Mass Spectrometer and Incoherent Scatter model (MSIS) thermospheric hydrogen profiles, show good agreement near the equinoxes, but an overestimate of diurnal asymmetry in summer and a severe underestimate in winter. Overall, it is found that the model underestimates the absolute observed intensity by a factor of ~ 2 . This work contributes to and agrees with the previous body of knowledge on geocoronal hydrogen; there is a limited amount of data for studying long timeline trends and the current models of atomic hydrogen do not accurately reflect the observations. Recommendations are provided for data collection with the INSpIRE observatory so as to best answer the current questions of geocoronal research.

List of Acronyms

ADC analog-to-digital converter. 50, 75, 76

ADU analog-to-digital unit. 28, 75

AE-C Atmosphere Explorer-C. 18, 135

AM post-midnight morning. 128

CCD charge-coupled device. xiv, 28, 54–56, 58, 61, 62, 64, 86, 90, 111

COTS commercial off-the-shelf. 51

CTIO Cerro Telolo Inter-American Observatory. 141–143

DOY day of year. 123, 126–130, 133, 137, 139, 140

EDI event driven interface. 68, 74

ERAU Embry-Riddle Aeronautical University. 39, 40, 43, 45, 49

ESS Environmental Sensor System. 48–51, 70, 73–76, 91, 144

FGVC functional global variable cluster. 68, 69, 72, 74, 76, 80, 89, 91, 145, 146

FITS Flexible Image Transport System. 42, 78, 87–92, 109

FPI Fabry-Perot interferometer. xiv, 3, 20–28, 30, 31, 33, 35, 54–56, 58, 61–63, 83, 89, 102, 106, 109, 111–113, 115, 117, 118, 124, 141, 145, 146

FSR free spectral range. 32, 33, 35

FWHM full-width half-maximum. 24, 26, 28, 32–35, 105, 113, 114

GCFI ground-fault circuit interrupter. 41

GUI graphical user interface. 67

GUVI Global Ultraviolet Imager. 20

INSpIRE Investigating Near Space Interaction Regions. xiv, xv, 3, 21, 22, 35, 37–39, 49, 50, 53, 54, 61, 66–70, 73, 74, 76–78, 108–111, 113, 115, 117, 122, 124, 140, 141, 143–147

IP internet protocol. 43

IT Information Technology. 40, 43

KPNO Kitt Peak National Observatory. 53, 141, 142

LOS line of sight. 119, 121, 124, 129

LV LabVIEW. 67, 68, 96

lyao_rt Lyman Atmospheric Observations Radiative Transport. xv, 3, 121–124, 129, 130, 133–138, 140, 142, 146

MSIS Mass Spectrometer and Incoherent Scatter model. xv, 4, 8–11, 19–21, 121, 122, 124, 129, 130, 133–138, 140–142, 146

NRL Naval Research Laboratory. 8, 18, 19

OPD optical path difference. 28

OS operating system. 42, 43

PBO Pine Bluff Observatory. 3, 49, 67, 124, 128, 135

- PCI** peripheral component interconnect. 50
- PCS** Pressure Control System. 41, 55, 58, 59, 69, 70, 73, 83–86, 91, 98, 111, 115, 144–146
- PM** pre-midnight evening. 128
- REDDI** Redline DASH (Doppler Asymmetric Spatial Heterodyne) Demo Instr.. 40
- SABER** Sounding of the Atmosphere using Broadband Emission Radiometry. 20, 21, 141
- SCS** Siderostat Control System. 40, 41, 48–51, 91, 98, 115, 144
- SHS** spatial heterodyne spectrometer. 22, 146
- SZA** solar zenith angle. 122, 123
- TIMED** Thermosphere Ionosphere Mesosphere Energetics and Dynamics. 20, 141
- TPM** Telescope Pointing Machine. 78
- TWINS** Two Wide-angle Imaging Neutral-atom Spectrometers. 20
- UPS** uninterruptible power supply. 40, 41, 43, 70, 73, 74
- UW-Madison** University of Wisconsin. 43, 49, 54, 59, 75, 77
- VI** virtual instrument. 67, 68, 87, 103
- VPN** virtual private network. 43
- WACCM-X** Whole Atmosphere Community Climate Model eXtended. 21, 141
- WHAM** Wisconsin Hydrogen-Alpha Mapper. 20, 141, 143

List of Symbols

Symbol	Description	Unit
A	Airy Transmission	%
A_{sys}	Airy Transmission of a multiple etalon system	%
C_o	ADC zero offset	ADU
C_{ALT}	Counts on the Altitude motor	ADU
C_{AZ}	Counts on the Azimuth motor	ADU
C_{adu}	ADC reading	ADU
E_k	Kinetic Energy	J
E_p	Potential Energy	J
G	Universal Gravitational Constant, equivalent to $6.67 \times 10^{-11} \text{ m}^3 \text{ kg}^{-1} \text{ s}^{-2}$	$\text{m}^3 \text{ kg}^{-1} \text{ s}^{-2}$
H	Scale Height	m
K_{ALT}	Counts per degree on the Altitude motor	
K_{AZ}	Counts per degree on the Azimuth motor	
L	Transducer Separation	m
M_{\oplus}	Earth mass, equivalent to approximately $5.97 \times 10^{24} \text{ kg}$	kg
N	Number of Molecules	molecules
N_A	Avogadro's Constant, equivalent to $6.022 \times 10^{23} \text{ mol}^{-1}$	mol^{-1}
P	Pressure	Pa

Symbol	Description	Unit
P_f	Relative pressure to atmospheric pressure	Pa
P_o	Pressure at the Earth's surface, equivalent to 101325 Pa	Pa
P_{ALT}	Degrees per volt on the Altitude potentiometer	
P_{AZ}	Degrees per volt on the Azimuth potentiometer	
Q	Free Spectral Range	cm^{-1}
Q_λ	Free Spectral Range at a particular wavelength, λ	cm^{-1}
R	Resolving Power	
R_\oplus	Earth radius, equivalent to approximately 6,371 km (3,959 mi)	km
T	Temperature	K
T_c	Temperature at the exobase (about 500 km)	K
V	Volume	m^3
ΔP	Pressure differential	Pa
$\Delta\mu$	Change in Index of Refraction	
Λ	Unitless Proxy for Potential Energy	
Λ_c	Unitless Proxy for Potential Energy at the exobase (about 500 km)	
α	Right Ascension	hr
χ	Hour Angle	hr
δ	Declination	deg
$\delta\sigma_{1/2}$	Full-width Half-maximum in wavenumber space	\AA^{-1}
ϵ	Altitude	deg
η	Molecular Polarizability of the Medium	m^3
λ	Wavelength	\AA
λ_o	Wavelength of incoming light, on-axis	\AA
λ_θ	Wavelength of incoming light, off-axis	\AA
\mathcal{F}	Coefficient of Finesse	
\mathcal{R}	Reflectivity or Reflectance	%

Symbol	Description	Unit
μ	Index of Refraction of the Surrounding Medium	
μ_f	Index of Refraction given a medium at pressure P_f	
μ_o	Index of Refraction given a medium at pressure P_o	
μ_e	Index of Refraction of the Etalon	
ρ	Mass Density	kg m ⁻³
ρ_o	Mass Density at Altitude z_o	kg m ⁻³
σ	Wavenumber	\AA^{-1}
σ_o	Wavenumber of incoming light, on-axis	\AA^{-1}
σ_θ	Wavenumber of incoming light, off-axis	\AA^{-1}
V	Voltage	V
θ	Angle of Incidence	deg
θ_{lat}	Latitude of the observer	deg
θ_{lon}	Longitude of the observer	deg
ζ	Azimuth	deg
a	Empirical Correction for Intermolecular Forces	Pa m ⁶
b	Empirical Correction for Finite Molecular Size	m ³ mol ⁻¹
d	Distance of Travel	m
f	Phase Space Density	m ⁻³
g	Acceleration due to Gravity	m s ⁻²
k	Boltzmann Constant, equivalent to 1.38×10^{-23} J mol ⁻¹ K ⁻¹	J mol ⁻¹ K ⁻¹
l	Etalon Spacing	m
m	Molecular Mass	kg
m_i	Molecular Mass of constituent i	kg
n	Number Density	m ⁻³
n_o	Number Density at altitude z_o	m ⁻³
p_i	Momentum Vector	kg m s ⁻¹

Symbol	Description	Unit
q	Charge	C
q_i	Position Vector	m
r	Radial Altitude, measured from the Earth's center	m
r_c	Radial Altitude of the exobase, measured from the Earth's center to the exobase	m
t	Elapsed Time	s
v	Velocity	m s^{-1}
w	Wind Speed	m s^{-1}
z	Altitude, measured from the Earth's surface	m
z_o	An initial altitude, measured from the Earth's surface	m
A	Cross-Sectional Area	m^2
G	ADC Gain	
m	Order of Interference	
R	Ideal Gas Constant, equivalent to $8.317 \text{ J mol}^{-1} \text{ K}^{-1}$	$\text{J mol}^{-1} \text{ K}^{-1}$

Chapter 1

Significance of Geocoronal Hydrogen

“For the first time in my life, I saw the horizon as a curved line. It was accentuated by a thin seam of dark blue light – our atmosphere. Obviously this was not the ocean of air I had been told it was so many times in my life. I was terrified by its fragile appearance.”

Ulf Merbold,
Astronaut for the European Space Agency

In the early, molten and smoldering, days of the Earth, outgassing due to high surface temperatures resulted in an atmosphere made of hydrogen, helium, methane, ammonia, and water vapor [2]. The high energy of this early atmosphere allowed the lighter constituents to easily escape [2]. After a large part of the early atmosphere escaped, a secondary atmosphere was formed by volcanic gases, including water vapor, methane, carbon dioxide, sulfur dioxide, and several nitrogen compounds [2]. When cyanobacteria made their appearance nearly 2.7 billion year ago, the oxygen previously entangled in water and carbon dioxide molecules could be released into the atmosphere via photosynthesis, and the early ecosystem started down a path that would create the oxygen- and nitrogen-rich atmosphere of today’s Earth [2]. In this way, the lifeforms of the past left the Earth in a more livable state than the state they came into (the author hopes it is not lost on her reader that today’s lifeforms are not headed for the same respectable legacy).

In the modern age, the atmosphere creates a welcome transition between the solidity of the Earth's surface and the harsh reality of free space. The molecules and atoms of our planet held captive in this region are too energetic to be constrained to the surface and, at the same time, not energetic enough to escape gravity. Furthermore, gases are highly compressible, naturally creating a density gradient with the highest density at the surface and falling off exponentially. This innate property of the atmosphere is used daily to human advantage; close to the surface, aircraft utilize the highly compressed atmosphere (and careful engineering) to create lift, whereas satellites at the further end of the atmosphere prefer the lower density for mitigating orbital decay. Human reliance on global navigation and communication systems means that understanding the vertical structure of the Earth's atmosphere is of fundamental importance.

Hydrogen is one of the escape artists of the atmosphere, capable of escaping both the Earth and, distressingly, the full understanding of atmospheric science. Atomic hydrogen density is an integral player in the big picture of solar terrestrial interaction. Resonant charge exchange reactions between atomic hydrogen and atomic oxygen are paramount to the formation and refilling of the plasmasphere after geomagnetic storms [3, 4]. Hydrogen that exists in the upper atmosphere also influences the ring current decay that occurs after geomagnetic storms [5]. Hydrogen is an important input parameter in ionospheric and plasmaspheric modeling studies [6]. However, being a light atom in a nearly collisionless environment, there are a limited number of easily observable interactions involving neutral atomic hydrogen. Yet, the theory of hydrogen vertical structure is well developed (see e.g. [7]). Therefore, a juxtaposition exists: the community believes to know hydrogen, but contradictions between models and observations and a lack of direct evidence continue to confound. The seasonal and solar cyclical trends in hydrogen density and dynamics are particularly understudied because of the lack of long timeline datasets due to the difficulty of observations.

1.1 Thesis Objectives

The primary objective of this work is to develop remote operations requirements and software for the Investigating Near Space Interaction Regions (INSpIRE) observatory. The INSpIRE observatory will be capable of acquiring long term, high-spectral-resolution atomic hydrogen datasets in order to build a baseline for studying exospheric variability. INSpIRE is designed to house two second-generation pressure-tuned Fabry-Perot interferometer (FPI) for the purpose of taking atomic hydrogen observations. The focus of this thesis is to prepare the observatory for the installation of a minimum of one of these FPIs in a remotely operable configuration before the observatory is deployed to a dark-sky location.

The secondary objective of this thesis is to explore the use of Balmer series data sets in studying hydrogen density altitude profiles through model-data comparisons. The modeling study will be integral in demonstrating the long-term capabilities of the INSpIRE observatory and in defining INSpIRE observing strategies. Previously collected atomic hydrogen intensity data from the FPI at Pine Bluff Observatory (PBO) near Madison, Wisconsin will be used to conduct model-data comparisons. The Lyman Atmospheric Observations Radiative Transport (`lyao_rt`) code written by James Bishop [1] will be utilized for this phase of research.

The rest of the introduction section will concentrate on the basic theories of the upper atmosphere that drive this research and give some background on hydrogen research up to this point. The following sections will outline the observational methods and needs of the observatory, the development and testing of the observatory's engineered capabilities, and the modeling study that motivates the observatory's objectives.

1.2 Getting Started with Atmospheric Physics

The Earth's atmosphere is often segmented into layers based on temperature changes as altitude increases, as shown in Figure 1.1. The lowest layer is called the troposphere, which extends from the Earth's surface to about 10 km altitude. This region

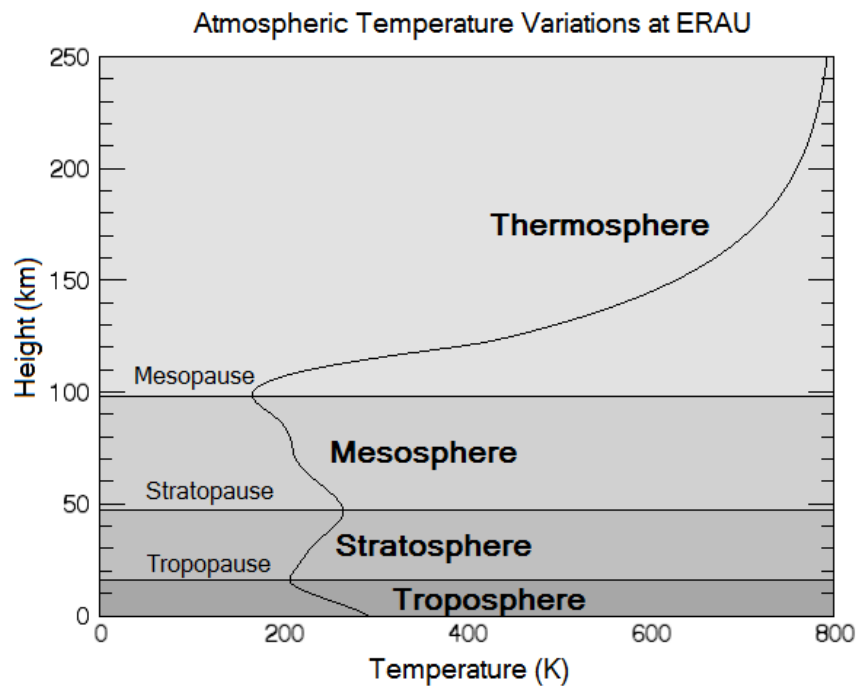


Figure 1.1: A temperature profile ($f_{10.7}=150$, $A_p=15$ e.g. medium solar activity), extending from the Earth's surface at Embry-Riddle Aeronautical University, Daytona Beach, to 250 km above the ground, shows the inversions that mark the layers of the atmosphere. Credit to Grace Butcher and Emma Galligan for model generation using the Mass Spectrometer and Incoherent Scatter model (MSIS).

of the atmosphere contains over 80% of the mass and nearly all of the water vapor content of the atmosphere. Temperature decreases in this region. The next layer, the stratosphere, extends from the tropopause to 50 km altitude. The stratosphere is characterized by rising temperatures due to absorption of solar radiation within the ozone layer that resides in this region. The mesosphere extends from the stratopause to about 85 km, and is characterized by extremely low temperatures (average -85°C) [2]. Many scientists find the mesosphere difficult to study, as it is too high up for aircraft and too low for satellites; only vehicles in transit through the mesosphere, such as rockets, can be used. The thermosphere starts at the mesopause and extends to the exobase, which dramatically changes altitude with temperature (see Section 1.3) but is nominally between 500 km and 1000 km. The thermosphere is characterized by increasing temperature and significantly decreased particle densities. The topmost layer is called the exosphere and extends out to 100,000 km. The Earth's exosphere is sometimes known as the geocorona (see Section 1.5), and thus, the hydrogen that exists in the geocorona is known as geocoronal hydrogen.

The atmosphere below the thermosphere is primarily composed of diatomic nitrogen ($\sim 78\%$) and diatomic oxygen ($\sim 20\%$) [2]. The remaining $\sim 2\%$ are considered trace gases and include argon, carbon dioxide, nitrous oxide, and methane. Starting at the mesosphere, molecular constituents begin to disassociate and decreased total density allows for molecular diffusion. The major species N_2 and O_2 are quickly dominated by atomic oxygen, helium, and hydrogen within the thermosphere and exosphere.

1.2.1 An Isothermal Atmosphere in Hydrostatic Equilibrium

Instead of using temperature, the atmosphere can also be divided into two altitude ranges based on constituent mixing. The homosphere, located between the surface and approximately 100 km, is dominated by eddy diffusion, also known as turbulent mixing, and constituents are well-mixed throughout all altitudes. The upper boundary of the homosphere is called the turbopause and is sometimes considered the lower boundary for outer space, also known as the *Karman Line*. The heterosphere, the

region above the turbopause, is dominated by molecular diffusion, where constituents separate to different altitudes depending on their mass. The homogeneous lower atmosphere can be treated as a well-mixed, but the heterogeneous upper atmosphere cannot be treated as such, and must be assessed per species rather than as a whole. If it is instead assumed that the entire atmosphere is homogenous, an equation for density as a function of altitude can be derived using hydrostatic equilibrium.

In a fluid at rest, the pressure at any point in the fluid is given by the weight of the fluid above that point. Given a column of the atmosphere with cross-sectional area, A , height, dz , and mass density ρ , then the pressure differential, dP , is given by the weight of the overlying column divided by the cross sectional area.

$$dP = \frac{-m_{col}g}{A} = \frac{-(\rho A dz)g}{A} = -\rho g dz \quad (1.1)$$

where acceleration due to gravity is noted as g in ms^{-2} , and ρ is the mass density in kg m^{-3} .

Considering the Ideal Gas Law,

$$PV = NkT, \quad (1.2)$$

where P is pressure in Pa, V is the volume of gas in m^3 , N is the number of molecules, $k=1.38 \times 10^{-23} \text{ J K}^{-1}$ is the Boltzmann constant, and T is the temperature of the gas in K. The volume can be re-written in terms of mass and mass density,

$$V = \frac{mN}{\rho}, \quad (1.3)$$

where m is the molecular mass of the gas in kg.

Substituting (1.3) for V in (1.2), along with a little rearranging, results in the equation of state for an ideal gas.

$$P = \frac{\rho kT}{m} \quad (1.4)$$

Equation 1.4 can be substituted into (1.1), to remove the dependence on pressure.

$$d\rho = -\rho \frac{mg}{kT} dz$$

Two assumptions must be made at this point, that the temperature and acceleration due to gravity are both constant for all altitudes. The latter assumption does not make a huge difference, but the former is non-trivial; the validity of these assumptions will be explored in a later section. If the reader has accepted this, once all of the pressure terms have been grouped on the LHS and all of the altitude terms have been grouped on the RHS, then each side of the equation can be integrated.

$$\int_{\rho_o}^{\rho} \frac{d\rho}{\rho} = -\frac{mg}{kT} \int_{z_o}^z dz$$

$$\ln \rho - \ln \rho_o = -\frac{mg}{kT}(z - z_o)$$

where ρ_o is the mass density at altitude $z=z_o$. Combining terms and applying the exponential reveals the exponential relationship between mass density and altitude for a gas in hydrostatic equilibrium:

$$\rho = \rho_o e^{\frac{-(z-z_o)mg}{kT}} \quad (1.5)$$

For work involving a particular species, it is more convenient to use number density, n , than mass density, ρ , since the mass is only a coefficient. For example, atomic hydrogen has a known mass per atom (approximately 1.67×10^{-27} kg), but trends in density are easily apparent without applying this factor. Since $\rho = m_i n$, where m_i is the mass of a singular unit of the particular species in kg and n is the number density of that species in m^{-3} , (1.5) can be re-written in terms of number density.

$$m_i n = m_i n_o e^{\frac{-(z-z_o)}{H}}$$

$$n = n_o e^{\frac{-(z-z_o)}{H}} \quad (1.6)$$

where n_o is the number density at $z=z_o$ and H is the scale height in m, given by

$$H = \frac{kT}{mg}$$

Atmospheric scale height, H , is the distance over which atmospheric pressure changes by e (i.e. ≈ 2.72 , or the base of the natural logarithm). It is sometimes called the “e-folding distance”.

1.2.2 Addressing the Isothermal Assumption

Equation 1.6 is derived under isothermal and hydrostatic equilibrium conditions. However, it is not a very good assumption that the Earth’s atmosphere is the same temperature at every altitude; this value can vary by 800 K between 100 and 400 km. To compare, over the same altitude range, the acceleration due to gravity varies between 9.81 m s^{-2} at surface level and 7.33 m s^{-2} at 1000 km.

Figure 1.2 shows various models of temperature in the atmosphere. The first widely used model of the atmosphere was the U.S. Standard Atmosphere [8]. It provided reference information for temperature and composition in the lower atmosphere, below 86 kilometers, based on measurements from sounding rockets and weather balloons [8]. The U.S. Standard Atmosphere does not vary with time of day or solar conditions. The Jacchia Reference Atmosphere was one of the first attempts to model the Earth’s atmosphere from the surface to beyond the exobase [9], and allowed for the user to input different exospheric temperatures, essentially modeling the solar conditions via this input. Jacchia is based on a static condition similar to the U.S. Standard Atmosphere, and uses a set of formulas to model the variations within the static conditions. The Jacchia Reference Atmosphere for the static condition is shown in Figure 1.2. Next to the Jacchia model is the Mass Spectrometer and Incoherent Scatter, or MSIS, series of models created by the Naval Research Laboratory (NRL). The most recent in the MSIS series is known as NRLMSISE-00; the ‘E-00’ on the end indicates that it’s the extended altitude version (from the ground to the exobase) from the year 2000 [10]. The NRLMSISE-00 temperature profile is based on incoherent scatter radar measurements, and allows for variation with direct solar conditions rather than wrapping everything up in the exospheric temperature [10]. Figure 1.2

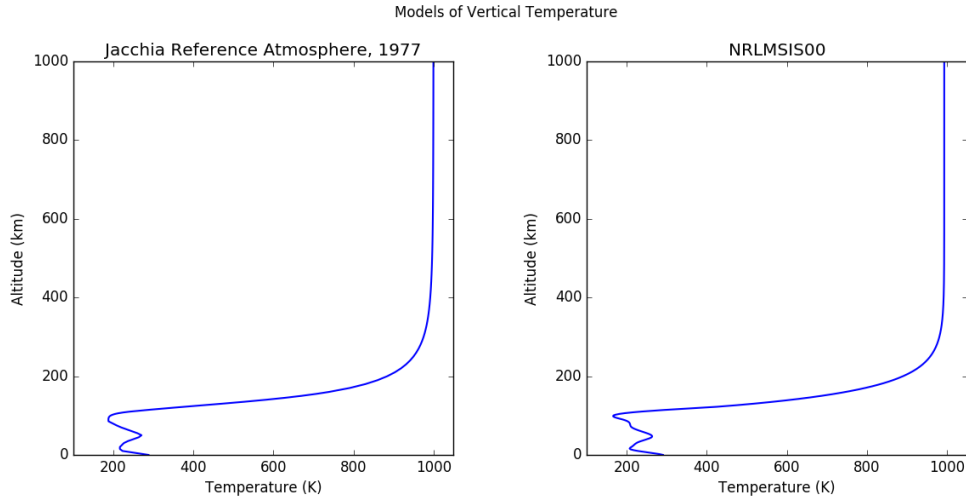


Figure 1.2: The Jacchia Reference atmosphere is smoothed compared to the more realistic NRLMSISE-00.

shows that temperature changes significantly with altitude, the largest swing being between the thermosphere and the exobase.

The temperature of the atmosphere and its constituents is driven by solar heating. In a given location on the Earth, the temperature will increase with direct solar radiation (summer, dayside) and decrease as solar radiation becomes less direct (winter, dayside) or blocked completely by the Earth (nightside). In as little as 12 hours, temperature in the upper atmosphere can vary by 100 to 200 K. Solar heating can also be the result of solar activity. At solar maximum, exospheric temperature can be over 1300 K, and at solar minimum, it can be as low as 600 K. Figure 1.3 includes a selection of NRLMSISE-00 temperature profiles that demonstrate the range of temperature variation due to solar heating.

Because temperature can make such a difference, it is common to write scale height as a function of altitude like so

$$H(z) = \frac{kT(z)}{mg(z)} \quad (1.7)$$

where $T(z)$ is given by models or measurements and $g(z)$ is derived from Newton's law of universal gravitation.

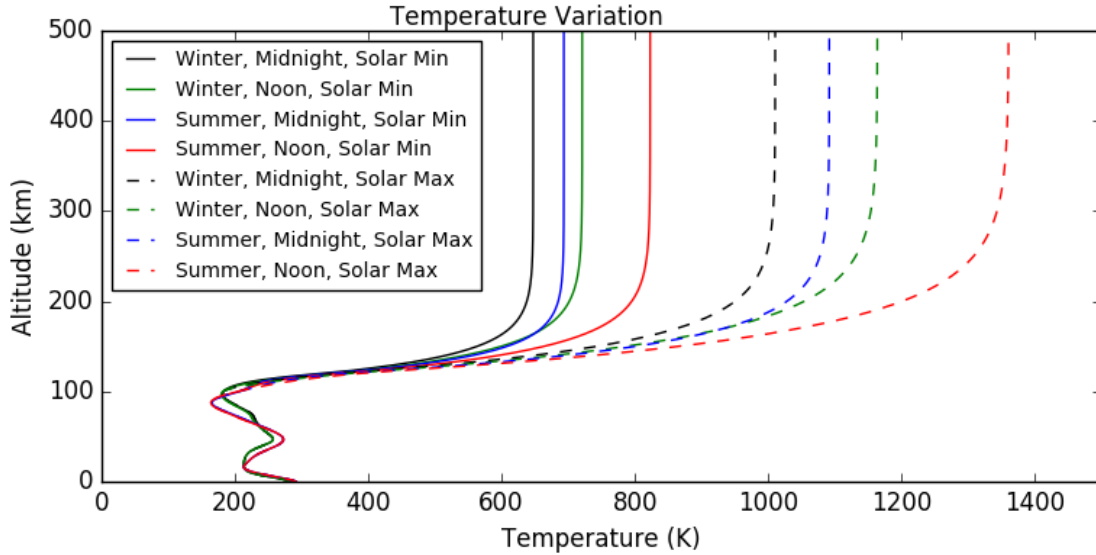


Figure 1.3: Temperatures changes on diurnal, seasonal, and solar cyclical basis can be quite significant in the upper thermosphere. Temperatures are generated with NRLMSISE-00.

$$g(z) = \frac{GM_{\oplus}}{(R_{\oplus} + z)^2}$$

where G is the gravitational constant $6.67 \times 10^{-11} \text{ m}^3 \text{ kg}^{-1} \text{ s}^{-2}$, M_{\oplus} is the mass of the Earth $5.97 \times 10^{24} \text{ kg}$, R_{\oplus} is the radius of the Earth $6.371 \times 10^6 \text{ m}$, and the altitude z is in m.

Atomic hydrogen in hydrostatic equilibrium is plotted in Figure 1.4 starting from the turbopause ($\sim 100 \text{ km}$), at which point each constituent is governed by its own scale height, although there are still interactions between constituents. The initial hydrogen density at the turbopause and temperatures are obtained from MSIS. Three treatments of hydrostatic equilibrium are demonstrated: one with constant temperature and gravity, one with constant temperature and a gravity gradient, and one with both temperature and gravity gradients. It is apparent that the temperature has a much larger effect on the vertical density structure than gravity, even given the simple model of hydrostatic equilibrium. For this reason, the vertical temperature profile is considered highly important to atmospheric density investigations.

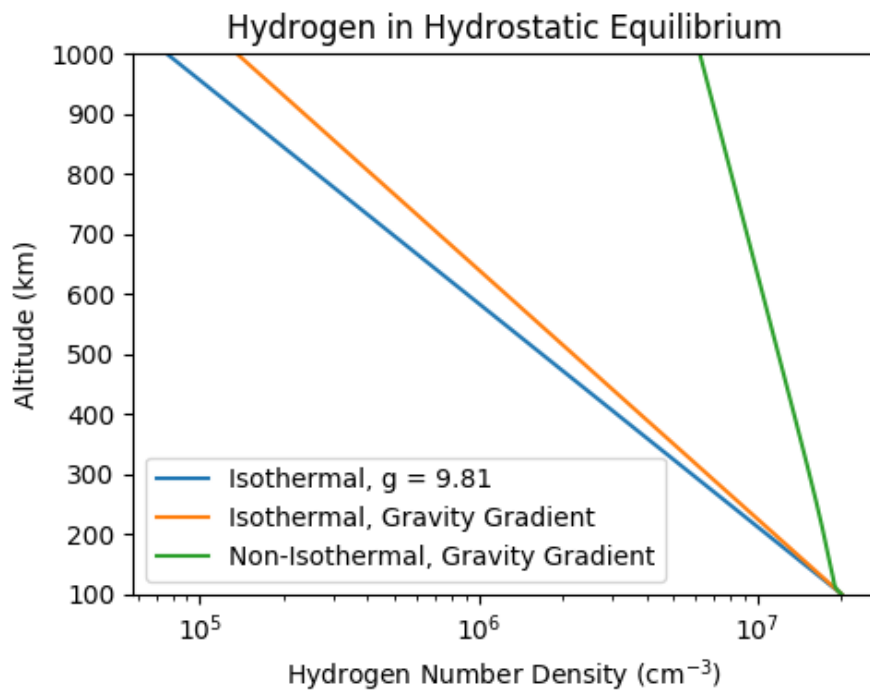


Figure 1.4: Hydrostatic equilibrium is most affected by changes in temperature, and less so by changes in gravity. Non-isothermal temperatures are generated with NRLMSISE-00.

1.3 An Explanation on Exospheres

The topmost, and sometimes only, layer of any atmosphere is called the exosphere and is the most susceptible to external forces, such as solar heating. In this region, the lines are blurred between atmosphere and interplanetary medium and interactions cause mass, momentum, and energy exchange between the two environments. Many planetary bodies in our solar system can claim at least an exosphere if not an entire atmosphere, including Mercury, Earth's Moon, and several asteroids [11]. Exosphere research will be important to a future that includes moon and asteroid resource mining as a key part of the sustainability of space exploration.

Of particular interest to this thesis is the Earth's exosphere, and, henceforth, the term *exosphere* shall refer to the exosphere of the Earth unless otherwise noted. The lower boundary of the exosphere is often called the *exobase*, although *exopause* and *critical radius* are sometimes used. The exobase is defined as the altitude at which the mean free path of an atmospheric species is equal to the scale height or, in other words, the altitude at which particles experience an average of one collision per scale height. The observant will realize that the height of the exobase, because it depends on scale height, is therefore directly dependent on temperature. Because the temperature of the atmosphere at each altitude changes with solar activity and the day-night cycle, the exobase can vary between roughly 500 and 1000 km.

To reframe the concept of the exosphere, exospheric dynamics are largely dominated by particles moving along trajectories rather than particles colliding with one another. Particle trajectories can be sorted into three categories: ballistic, satellite, and escape. A *ballistic* trajectory is one that bounces through the exobase; that is, a ballistic particle enters the exosphere without enough velocity to escape Earth's gravity, so it must come back towards the exobase. A particle in a *satellite* trajectory is in orbit around the Earth at an altitude above the exobase, and an *escape* trajectory describes the path of a particle with enough kinetic energy to leave the influence of Earth's gravity. Because collisions are rare, escape is more likely for particles within this region.

Exospheric dynamics is best outlined by *Chamberlain* [7] and remains the foundational theory on which exospheric models are based. It is outside the scope of this thesis to go into mathematical detail on exospheric theory, but a brief explanation ensues (for a good read, refer to [11]). Density distribution in the exosphere is the fundamental issue, and parameters such as escape flux and temperature come from the initial density calculation. It is initially assumed that the density distribution is spherically symmetric and geophysical effects, such as the day-night cycle or rotation of the atmosphere, are ignored [7].

The basis of the density calculation is the Liouville equation from statistical mechanics, which implies that the density in phase space remains constant along a dynamical trajectory. *Chamberlain* uses “phase space” to mean that the particles are distributed over spatial, q_i , and momentum, p_i , coordinates in six dimensions [7]. *Chamberlain* assumes that the velocity distribution at the exobase is Maxwellian, given the temperature at the exobase, and calculates a corresponding phase space density associated with that Maxwellian distribution [7]. In this way, the density distribution at the exobase is used as an initial condition. If the resulting phase space density is integrated over the momentum space, effectively removing motion from the phase space density, then a volume density emerges that is not unlike the hydrostatic equation derived in Section 1.2.1:

$$n(r) = \int f(q_i, p_i) d^3 p_i = n_o e^{-(\Lambda_c - \Lambda)} \quad (1.8)$$

where $f(q_i, p_i)$ is the density in phase space, r is the distance from the center of the Earth to the particle, and Λ is a unitless proxy for potential energy:

$$\Lambda(r) = \frac{GM_{\oplus}m}{kT_c r}$$

$$\Lambda_c = \Lambda(r_c)$$

where Λ_c is calculated at r_c , the radial distance to the exobase, and T_c is the temperature at the exobase.

The hydrostatic equation, however, is not the end of the story. Dynamics play a large role in the density distribution over altitude and must be accounted for by the use of partition functions. In statistical mechanics, partition functions are used to represent a statistical energy state within a set of states. The energy states of the exosphere are given by the dynamic trajectories: ballistic, satellite, and escaping [7]. The partition function is a complicated integral for which different integration limits will reveal different energy states. The density distribution with altitude is ultimately the sum of the representative partition functions multiplied by the hydrostatic equation [7].

1.4 Signatures of Hydrogen

There are three well-known methods of measuring atmospheric neutral atomic hydrogen density. The first type is indirect, and involves measuring the intensity of airglow emissions. The second type of detection is also indirect using the assumption of charge exchange equilibrium. The third is direct, *in situ* mass spectrometer measurement of neutral hydrogen.

1.4.1 Airglow

Hydrogen airglow is caused by interactions between atomic hydrogen and solar radiation. When a solar photon of the right wavelength (and thus the correct amount of energy) comes into contact with a hydrogen atom, then the hydrogen atom is energized. It cannot remain in the energized state for very long, and so the hydrogen atom releases its newfound energy in the form of another photon. The released photon can be the same wavelength or longer (lower energy) than the original photon; in the case of the released photon having a lower energy, the process is called fluorescence.

Figure 1.5 shows the first four energy levels of atomic hydrogen and a sampling of Lyman and Balmer series transitions. The Lyman series either starts or ends the transition at $n = 1$. If it starts at $n = 1$, then the transition was an absorption; if it ends at $n = 1$, then the transition was an emission. The Balmer series starts or ends

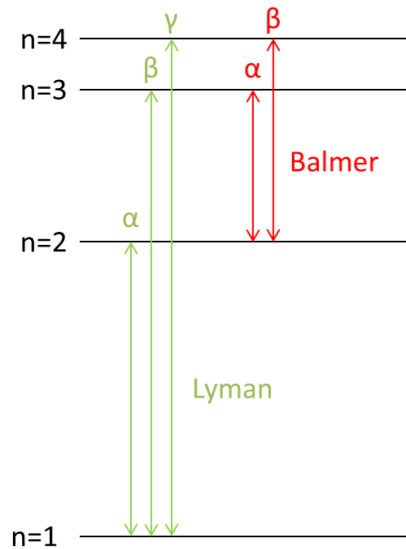


Figure 1.5: The Lyman and Balmer series transitions as depicted on the first four energy levels of an atomic hydrogen atom.

at $n = 2$, and so in order to emit or absorb in the Balmer wavelengths, the atom must already be energized to a higher level than $n = 1$. In the upper atmosphere, incoming solar Lyman- α photons (1216 \AA) always produce Lyman- α emission, since the energy levels are discrete. Solar Lyman- β photons (1026 \AA) create two options: (1) Lyman- β can be fully scattered from $n = 3$ to $n = 1$, or (2) the atom could fluoresce in Balmer- α instead, releasing energy from $n = 3$ to $n = 2$. There's an $\sim 88\%$ chance that Lyman- β will simply scatter, and a $\sim 12\%$ chance that it's converted into Balmer- α . For Lyman- γ (973 \AA), there are three emission options: Lyman- γ ($\sim 84\%$), Balmer- β ($\sim 12\%$), and a transition that isn't shown called Paschen- α ($\sim 4\%$).

The Lyman series of wavelengths are all ultraviolet, which means that they are absorbed by the atmosphere before making it to the ground. The Balmer series emissions are in the visible wavelengths, but the low chance that they will be emitted (roughly 12% for Balmer- α and $-\beta$) means that the emissions are extremely faint. Balmer- α emission intensity measures in the tens of rayleighs ($1\text{R} = 10^6/4\pi \text{ photons s}^{-1} \text{ cm}^{-2} \text{ sr}^{-1}$); for comparison, the moonless night sky has an intensity of 250 R,

and the Northern lights (i.e. aurora) can be as bright as 1000 kR. However, since the Balmer series is visible from the ground, highly sensitive ground-based instruments are able to measure the signature of hydrogen.

The major issue with airglow measurements are that they are, by nature, an integrated observation – any observing column will include airglow emission intensity from the entire column. Airglow observers use radiative transport modeling to account for this and to obtain density information via forward modeling. Radiative transport modeling requires knowing something (or guessing) about the hydrogen concentrations before the predicted intensity can be calculated (see Chapter 6).

1.4.2 Charge Exchange

Neutral hydrogen is involved in a very simple, very important, charge exchange reaction within the thermosphere that involves hydrogen ions, oxygen ions and neutral oxygen:



Although neutral hydrogen concentration can be difficult to measure, the other three concentrations are relatively easier. Ion concentrations are easily measured with ion mass spectrometers *in situ* or using incoherent scatter radar from the ground. Neutral oxygen is more difficult than the ion measurements, but there is a large body of data taken with neutral mass spectrometers and satellite drag measurements [12, 10]. Once an estimate is made for each of the ion and neutral oxygen concentrations, the charge exchange equilibrium equation can be solved for neutral hydrogen. This method is very indirect and requires very good calibration of three independent measurements, otherwise the uncertainty can be very high.

1.4.3 Mass Spectroscopy

The direct measurement of neutral hydrogen concentrations is a concept that has not yet been fully embraced by the atmospheric science community. This method is

ideal and would provide actual data points at individual altitudes, but it has been difficult to pull off until recently. Time-of-flight spectroscopy relies on accelerating ions through a time-of-flight tube and measuring the travel time, given that the length of the tube and the acceleration voltage applied is known [13]. In order to measure neutrals only, any sneaky ions are repelled from the gate using a retarding potential grid and then the neutrals that are allowed to enter the gate are ionized before acceleration.

At the entrance to the mass spectrometer time-of-flight tube, a voltage, V , is applied to the ion, of mass m and charge q , that accelerates it through the tube at velocity v , effectively converting its electric potential energy, E_p , into kinetic energy, E_k :

$$\begin{aligned} E_p &= qV = \frac{1}{2}mv^2 = E_k \\ qV &= \frac{1}{2}m \left(\frac{d}{t} \right)^2 \end{aligned} \quad (1.10)$$

A substitution can be made for velocity such that the time of flight t is the measured quantity and d is the known length of travel.

The issue with hydrogen is that its mass is 1 amu (atomic mass unit), and so the time of flight is the smallest that it could possibly be. A space-ready neutral mass spectrometer with the capability to measure atmospheric hydrogen was successfully introduced for the first time as a cubesat mission called Dellingr, which launched in 2017 [14]. As of writing this, engineering tests have been successful, but no publications have been produced on the results of the mission.

1.5 A History of Hydrogen Observations

Because of the issues with ground-based airglow measurement discussed in Section 1.4.1 regarding the faintness of visible emissions, the signatures of the interaction between atomic hydrogen and solar radiation were not observed until Earthlings had

the ability to take measurements from space. Until this major breakthrough, it was not well known how much hydrogen was present in the Earth's atmosphere nor how far out the population could be maintained.

Observations of atmospheric hydrogen began in the mid-1950s with the NRL Aerobee and Javelin sounding rocket programs. In 1955, ultraviolet Lyman- α scattering from the hydrogen geocorona was first discovered while investigating the extreme ultraviolet spectrum of the night sky. Ten such rocket flights taken between 1955 and 1962 were analyzed with the conclusions that the measurements indicate airglow variation with time and that future "launch dates and times should be carefully planned so as to obtain the best pattern of observations for the fewest number of rocket launches" [15]. Little did they know, the next giant leap in geocoronal hydrogen research would not involve rocketry but instead the lunar surface.

Most recently famous for receiving a National Medal of Technology and Innovation from President Obama in 2012, George Carruthers was the Principal Investigator on the Far Ultraviolet Camera/Spectrograph sent to the moon during the Apollo 16 mission in 1972 [16]. Operated by astronaut John Young, the camera was pointed in various directions, towards and away from the Earth, to take images in the ultraviolet spectrum of the Earth's atmosphere, stars, and yet undiscovered nebulae. Figure 1.6 shows one such image of Earth. In this image, the hydrogen geocorona can be seen glowing in the ultraviolet out to very high altitudes, the Earth's shadow cuts a dark cylinder through the glowing cloud, and aurora are seen on the nightside at both poles. This image inspired many to call this hydrogen cloud the geocorona, as it reminds one of the Sun's corona, the bright glowing halo visible during a total solar eclipse.

The next major advancement was the Explorer series of satellites launched by the United States in the 1970s. Atmosphere Explorer-C (AE-C), launched in 1973, was equipped with an ion mass spectrometer with a mass resolution capable of measuring hydrogen and oxygen ions [17]. Neutral oxygen mass spectroscopy was also collected. The charge exchange method of calculating neutral hydrogen concentration was utilized here. The first analysis to be published on neutral hydrogen results from AE-C looked at data taken between December 1974 and January 1975 and concluded that

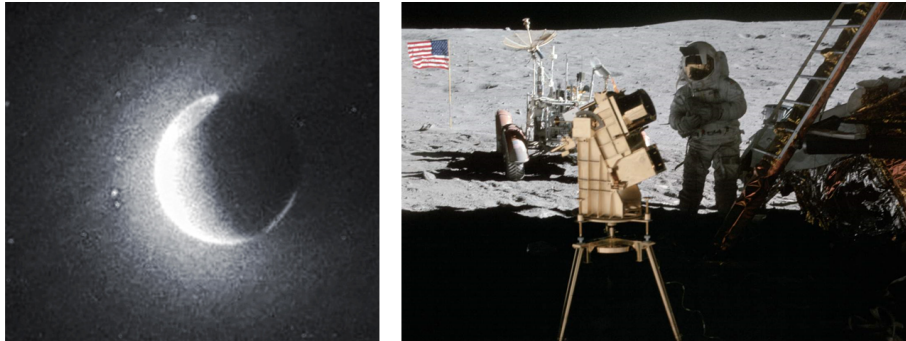


Figure 1.6: (left) The entire geocorona was captured on film for the first time from the moon [16]. (right) Apollo 16 Astronaut Charlie Duke standing near the Far Ultraviolet Camera/Spectrograph in the shadow of the lunar lander (Photo Credit: John Young/NASA).

there is an anti-correlation between hydrogen density and temperature that results in diurnal variation and a doubling of the density from summer to winter conditions [18]. The second analysis was based on data taken in February 1974 and reported evidence of large hydrogen flows from the lower thermosphere to the upper thermosphere [19]. Both of these studies would be used as hydrogen data inputs for the MSIS-83 empirical model of the atmosphere [12].

Around the same time that the NRL started reporting Lyman- α readings via sounding rocket in the 1960s, a series of ground-based observing campaigns began to look for visible airglow from the surface. Using Fabry-Perot interferometry, *Sheglov* found a distinct diurnal variation ($\sim 30\%$ increase from evening to morning) in nighttime Balmer- α observations taken during winter 1962-1963 [20]. Grille spectrometer measurements made by *Tinsley* [21, 22, 23] detected signatures of diurnal variation with Balmer- α observations in the early morning approximately 20% brighter than evening observations given similar solar depression angles and relative solar azimuths. *Tinsley's* result is consistent with the earlier Balmer- α observations of *Sheglov* [20] and was later successfully modeled to obtain estimates of hydrogen density variation [24, 25]. *Tinsley's* modeling work estimated a morning-to-evening hydrogen density ratio associated with the difference in Balmer- α intensity of 1.9 at low solar activity and 1.3 at high solar activity, indicating a solar cycle dependence in the diurnal

variation. Observations of H- α intensity using an FPI by *Shih* in 1985 also show a diurnal intensity variation of nearly 10% from evening to morning given the same viewing geometry, although this was much lower than their theoretical estimate of 30% based on an exobase density diurnal ratio of 1.8 ± 0.3 [26]. In a 2001 study, *Bishop et al.* [27] completed modeled fits to the morning and evening FPI Balmer- α intensity observations of *Harlander and Roesler* [28] and obtained an estimate of diurnal variation in exobase density of ~ 3.0 [27] where MSIS-86 predicted a factor of 1.9 for the same observing conditions [29]. Additionally, *Nossal et al.* has looked at solar cyclical variations over several solar cycles [30] and presented model-data comparisons between Balmer- α intensity data from the Wisconsin Hydrogen-Alpha Mapper (WHAM) and modeled intensity as generated using NRLMSISE-00 as an input to the radiative transport model of *Bishop* [1]. The result agreed with the earlier investigations of *Bishop et al.* [27], that modeled intensities created with MSIS as the thermospheric model of hydrogen underestimate the observed intensity by a factor of ~ 2 .

Airglow measurements have also been taken by space-based instruments. *Waldrop and Paxton* report on a 2002-2007 dataset taken by the Global Ultraviolet Imager (GUVI) on-board the Thermosphere Ionosphere Mesosphere Energetics and Dynamics (TIMED) spacecraft [31]. GUVI Lyman- α observations were compared to the *Bishop* radiative transport model [1] (see Chapter 6) using NRLMSISE-00 as the hydrogen model input. It was found that the model overestimated the observations by an average of 50% during solar maximum and solar minimum conditions. Another set of satellites known collectively as Two Wide-angle Imaging Neutral-atom Spectrometers (TWINS) had in each of their instrument packages a Lyman- α detector, each of them collecting hydrogen airglow data from 2008 to 2013 [32]. An investigation of geomagnetic storm responses of geocoronal hydrogen showed that there was an increase in Lyman- α emissions by 9 to 23% within 11 hours from initial storm onset between eight storms in the study [32].

A second instrument on-board TIMED, the Sounding of the Atmosphere using Broadband Emission Radiometry (SABER), was used to study the emission rates of OH, which is directly related to a reaction between hydrogen and ozone in the region

near the mesopause [33]. Mesospheric SABER data (85-95 km) was used in a model data comparison with the Whole Atmosphere Community Climate Model eXtended (WACCM-X) to confirm temporal trends in neutral hydrogen density predicted by the model [33]. The study found that hydrogen density is highest during solar minimum, winter, and just before sunrise (as opposed to solar maximum, summer, and just before sunset) [33].

To summarize the lessons learned from these studies:

1. Hydrogen density goes through temporal cycles, including diurnal, seasonal, and solar cyclical, where the highest densities correspond to lower temperatures.
2. The standard model of hydrogen density in the Earth's atmosphere, MSIS, is based on a limited number of mass spectrometer measurements and does not accurately reflect airglow or radar observations.
3. Very few direct measurements of neutral atomic hydrogen exist, leaving questions about the variability and dynamics of hydrogen density over altitude, temporal trends, and during geomagnetic activity.

1.6 The INSpIRE Observatory

The INSpIRE observatory is currently located at the Daytona Beach campus of Embry-Riddle. Development of the observatory began in 2014 with the installation of the shipping container housing and the 12-foot clamshell dome. Since then, the observatory has been equipped with a siderostat for light collection, several imaging detectors, and the pressure tuning peripherals for controlling the FPI. Dome, siderostat, instrument calibration, and detector control have been established through remote operations using LabVIEW. Ongoing work includes aligning and coupling the FPI to the siderostat and implementing calibration lamp and flip mirror controls.

The INSpIRE remote observatory is in development with the intent of fulfilling the need for long timeline datasets of hydrogen measurements. The goals of the INSpIRE effort are to

1. establish an adaptable research station capable of contributing to terrestrial and planetary aeronomy,
2. integrate two state-of-the-art second generation FPI and one spatial heterodyne spectrometer (SHS) into a remotely operable configuration,
3. deploy this instrumentation to a dark, clear-air site, establishing a stable, well-calibrated observatory, and
4. embark on a series of observations designed to contribute to three major areas of geocoronal research: geocoronal physics, structure/coupling, and variability.

The INSpIRe observatory provides five instrument ports, two of which are saved for visiting instruments that can be easily swapped out. The three permanent installations are planned to be two FPIs and one SHS. The FPIs will be equipped with a variety of interference filters and calibration lamps for taking data on multiple wavelengths. The SHS adds another set of wavelengths to the observatory's capabilities along with high resolution doppler measurements.

The observatory is designed to be easily deployable, with take down and set up time close to 3 or 4 weeks. Once at a dark, clear-air site, remote operations software developed for this thesis will be utilized to take observations without traveling to the observatory. The remote location has not been officially determined at this point in time, but several options in the midlatitudes of North America are under consideration.

The INSpIRe observatory provides many opportunities for contributing to atmospheric or planetary science. Between two FPIs, the observatory is designed to be able to collect nearly simultaneous Balmer- α and Balmer- β emission intensities in order to better constrain the retrieval of hydrogen density profiles through forward modeling. Additionally, both the SHS and FPIs can be used to collect data on thermospheric winds [34, 35]. FPIs have proven useful, also, for studying the atmospheres or ablative surfaces of other planetary bodies, such as comets or the Earth's moon [36, 37].

Chapter 2

Observing Methodology

“Thus the yeoman work in any science, and especially physics, is done by the experimentalist, who must keep the theoreticians honest.”

Michio Kaku,
Theoretical Physicist

2.1 Geocoronal Observations 101

Observations of geocoronal Balmer series emissions using a Fabry-Perot interferometer (FPI) must be taken on cloudless nights close to new moon. Observing starts with instrument calibration, where the FPI is set up for a particular wavelength observation. Next, pointing on the sky and data collection occurs. Interspersed between data collection on the sky, calibration images should also be taken periodically. An observing log is kept for each observing session, where the observer can keep track of acquisition time, pointing geometry, observing room conditions, and sky conditions for each observation. The log is important for in-depth data analysis, which is accomplished at a later time.

During observations, some high level data analysis is performed to assess data quality as it is taken. Since the FPI produces an annular fringe pattern (see Figure 2.1), the technique for converting the fringe pattern into a spectrum is called ‘annular

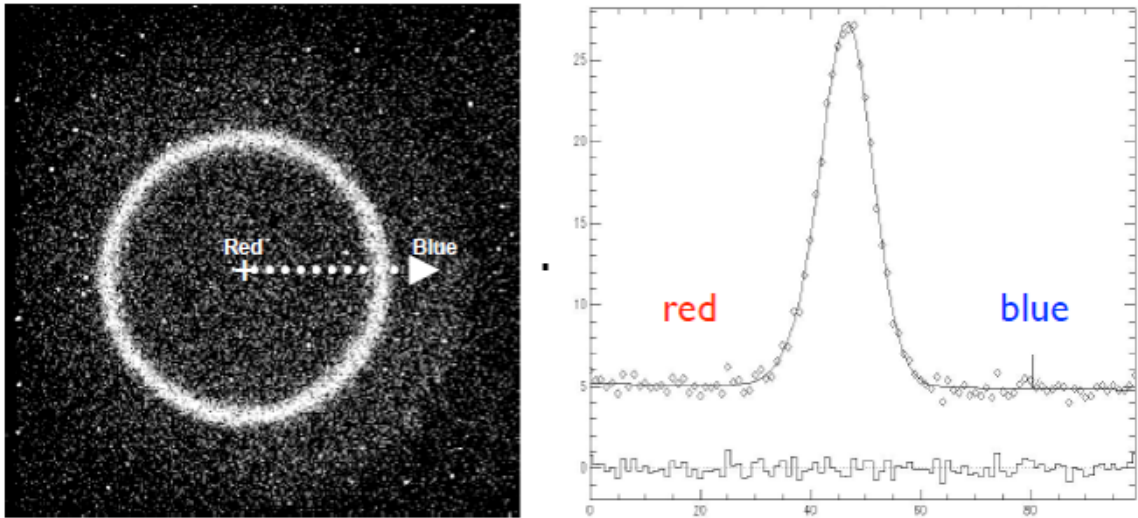


Figure 2.1: (left) An image of an H- α fringe pattern through an FPI. The image is spattered with bright spots caused by cosmic ray hits. (right) Spectra generated from the H- α fringe. Figure credit to [38].

summing’ or ‘ring summing’ (see Section 2.1.3). The spectral window starts at the center of the ring pattern, and decreases in wavelength as the radius of the annuli increases, as in Figure 2.1. A well-tuned FPI fringe has a full-width half-maximum (FWHM) corresponding to the FPI’s designed resolving power (see Section 2.2).

2.1.1 Viewing Geometry

Since Balmer series emissions occur on the sunlit side of the Earth’s atmosphere, geocoronal hydrogen observations are highly dependent on solar zenith angle (the angle between the zenith and the Sun’s depression angle). Solar Lyman- β , the photon that is (mostly) responsible for Balmer- α emission, is absorbed at 102 km. This altitude is known as the ‘black level’, and the Earth’s shadow plus the black level creates a cylinder of radius equal to the radius of the Earth plus 102 km. Singly scattered emission is assumed to originate on the outside of this cylinder, in the sunlit atmosphere. The altitude of the crossing point of the ground-based instrument’s line of sight with this cylinder is known as the shadow altitude of the observation (see Figure 2.2). Observations have shown that emission intensity varies strongly with

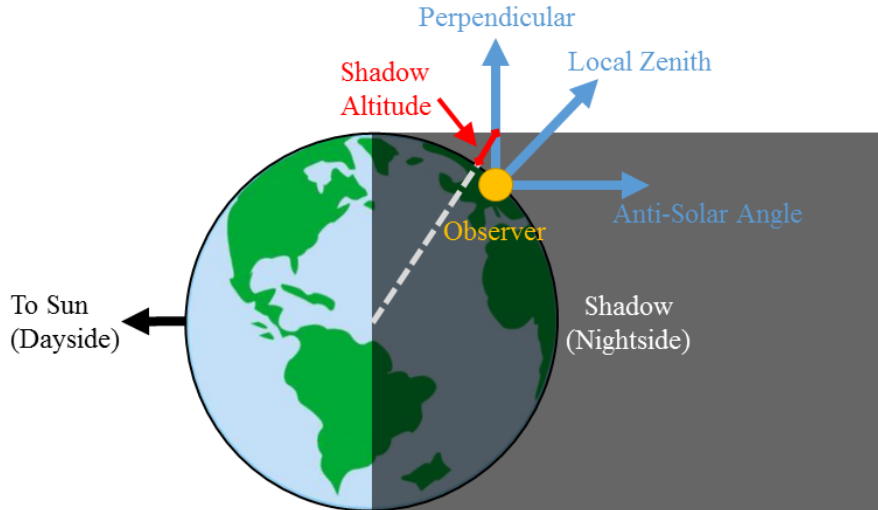


Figure 2.2: Geocoronal hydrogen emissions have been shown to vary strongly with a parameter called ‘Shadow Altitude’, which is the altitude of the crossing point between the observer’s line of sight and the Earth’s shadow.

shadow altitude, varying between $\sim 2 R$ at midnight to $\sim 15 R$ ($1R = 10^6/4\pi$ photons $s^{-1} cm^{-2} sr^{-1}$) near the dawn or dusk terminator [39].

A common observing pattern is to point at zenith for the entire observing session; in this case, the Earth will rotate the observer through its shadow from dusk to dawn. Every observation (taken every 5 to 10 minutes) corresponds to a different shadow altitude. Shadow altitude starts low at dusk, increases towards midnight, and then decreases towards dawn. If it is assumed that no scattering is coming from below the shadow altitude, then over a night of observations, an altitude profile of the H- α airglow is built up. At low shadow altitudes, this is an integration over a larger column than at high shadow altitudes, so the expected trend is to see higher intensity at dusk and dawn, and lower intensity at midnight (see Chapter 6 for further details).

2.1.2 Instrument Calibration

Setting up an FPI for data collection requires the usual powering up and initialization of various equipment (e.g. camera, lamp, focusing lens, filter wheel, etc.), but the most time-consuming part of the process is pressure tuning. The tuning procedure,

when done manually, can take up to one hour to complete. The goal of pressure tuning is to find the optimal pressure difference between the dual etalons that will result in a high quality FPI fringe (low FWHM, high peak intensity) for a particular wavelength. Night-to-night variability of the optimal pressure for a particular wavelength is close to 1 or 2 torr, so often the observer has a good idea of the expected optimal pressure. Optimal pressure for a particular wavelength can change with the temperature of the observing room, so it's important to calibrate the pressure at least once per observing session, if not multiple times in a given night. More detail on FPI theory can be found in Section 2.2 and the theory of pressure tuning can be found in Section 2.3.

Pressure tuning starts with a calibration source. Calibration lamps that emit at the wavelength of interest are used as the source, although their light must be diffused by reflection or some other method before entering the FPI aperture. A bright, annular fringe pattern should result from looking at the calibration source. Pressure is iterated over an array of values, usually five pressure values, centered on an initial guess from the observer. At each new pressure value, an image of the calibration source is taken and saved. After all of the tuning images are taken, the observer runs a tune analysis that converts the fringe pattern in each image to spectral space (see Section 2.1.3) and calculates the FWHM and peak transmission intensity. The FWHM and peak intensity are then plotted against pressure and a parabola is fit to find the extrema. The optimal pressure is the one that results in the lowest FWHM and the highest peak intensity, or in other words, the sharpest peak.

In order to understand the instrument behavior at the time of data collection, a final image of the calibration source is taken using the optimal pressure. This final image is the key to wavelength calibration during data analysis. Given a long observing session, the observer should consider taking multiple calibration images during the session. It should also be noted that changing wavelengths during an observing session requires going through the pressure tuning process from the beginning.

A second calibration is necessary for converting pixel counts on the detector into absolute intensity in rayleighs. The traditional source for geocoronal Balmer- α investigations is the North America Nebula, a large, diffuse H- α target [38]. This requires that the observing system has the ability to precisely point at the same patch of the

nebula for each calibration in order to get consistent results.

2.1.3 Annular Summing Technique

The ring summing, or annular summing, technique is based on one basic principle of the FPI fringe pattern: equal area annuli translate to equal spectral bins. The fringe pattern is divided into equal area annular bins, taking care to choose an area that corresponds to a radial width of two pixels or greater for every bin to satisfy Nyquist's sampling theorem. The ring center and ring sum algorithms are based on work done by *Coakley et al.* [40] and *Mierkiewicz et al.* [38], but have since been optimized and translated into Python 3.

Bins must be centered on an accurate ring center corresponding to the center of the fringes on the detector. A bad center can distort the output spectra. An initial center guess is required from the observer as an input to the ring center algorithm. This can be done by overlaying a circle of a given radius on top of a fringe image and then changing the center of the overlaid circle until it lines up with the fringes. Generally, though, the center from a previous observation will give a good enough center guess, as long as the optics and CCD have not been moved. Once an initial center is given, the ring center algorithm goes through a coarse and a fine grid search, where the center is varied and a ring sum is performed given the new center. The best center results in the narrowest spectral emission line width. In the coarse grid search, a 5 x 5 grid of 0.5 pixel resolution is used, and in the fine grid, a 7 x 7 grid of 0.1 pixel resolution is used. In this way, the ring center algorithm outputs an optimal subpixel center.

Once a fine-grid center is achieved, ring summing can ensue. Pixels on an imaging sensor tend to be square, which does not translate smoothly into circular patterns. Each pixel in the array is assigned an annulus area, calculated by assuming a circle of radius equal to the distance between the pixel and the ring center. For each pixel, the calculated area is divided by the area chosen to be the area of the annular bins. The result of this, rounded down to the nearest integer, is the bin number that the pixel will be assigned to. For each bin, any pixel counts that are outside of three standard

deviations are thrown out: this filtering is done twice to be certain that all hot pixels are removed. After hot pixel removal, all of the pixels in each bin are summed up and divided by the area of the bin, so that a line profile can be plotted in average pixel counts over bin number. Since the bins represent equal spectral intervals and the modern charge-coupled device (CCD) is good at converting photons into analog-to-digital unit (ADU) space at a linear rate, this output is good enough to calculate a FWHM (in bin space) and a peak transmission intensity (in ADU space) to calibrate the instrument in real-time. However, during in-depth data analysis, the bin numbers will be mapped to their spectral intervals and the average pixel count will be mapped to absolute intensity using a known-intensity calibration source (like an H- α emission nebula).

2.2 Fabry-Perot Interferometry

The instrument of choice for ground-based geocoronal hydrogen work is the Fabry Perot Interferometer, or FPI, which offers high sensitivity when the target emissions are spatially extended and diffuse, e.g. atmospheric or nebulous emissions [41]. The FPI is an interferometer, first invented in 1901 by Charles Fabry and Alfred Perot [42], that relies upon multiple reflections between two partially reflective plates. One pair of plates makes up one *etalon*, and the pair is spaced some known distance apart. Figure 2.3 shows a ray diagram of a beam incident on an etalon at an angle of θ .

The inward-facing surfaces of the pair are coated with a partially reflective coating of reflectance, \mathcal{R} . The coating allows some amount of the light to be transmitted and the rest to be reflected, resulting in multiple beam interference given one incident beam. In Figure 2.3, the etalon spacing is a constant l , the refractive index of the etalons are given as μ_e , and the refractive index of the surrounding medium is given as μ .

Constructive interference will occur when an integer multiple, m , of the wavelength of the incoming light, λ , is equal to the optical path difference (OPD). From Figure 2.3, the optical path difference is given by the red reflected rays minus the green transmitted rays; all of the black rays are the same for both outgoing beams up to

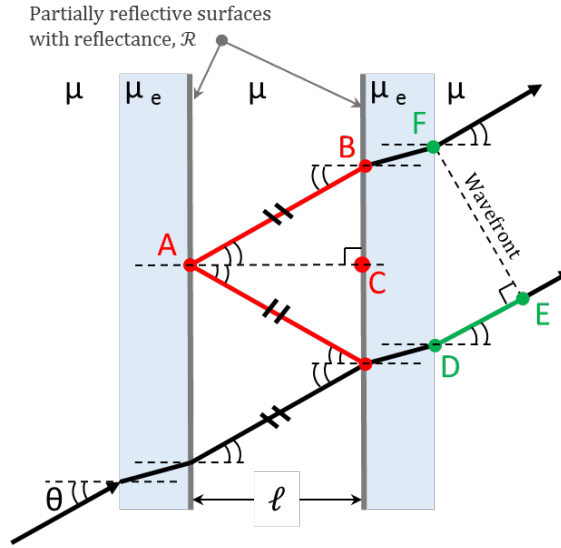


Figure 2.3: A ray diagram of a beam incident with an etalon at angle θ .

the wavefront.

$$\begin{aligned} m\lambda &= \text{OPD} \\ m\lambda &= 2\overline{AB} - \overline{DE} \end{aligned} \quad (2.1)$$

The reflected ray, \overline{AB} , is the hypotenuse of the right triangle $\triangle ACB$. Taking the cosine of $\angle BAC = \theta$ reveals an expression for the distance traveled by the reflected rays.

$$\overline{AB} = \frac{\mu l}{\cos \theta} \quad (2.2)$$

The transmitted ray, \overline{DE} , is a side of the right triangle $\triangle FED$, opposite of $\angle DFE$. Taking the sine of $\angle DFE = \theta$ gives the following relationship.

$$\overline{DE} = \overline{FD} \sin \theta$$

It turns out that $\frac{1}{2}\overline{FD}$ is equivalent to \overline{BC} , which is one of the sides of right angle $\triangle ACB$. Now taking the tangent of $\angle BAC = \theta$ results in an expression for \overline{FD} .

$$\overline{FD} = 2\mu l \tan \theta$$

This means that \overline{DE} is equivalent to

$$\begin{aligned}\overline{DE} &= (2\mu l \tan \theta) \sin \theta \\ \overline{DE} &= 2\mu l \frac{\sin^2 \theta}{\cos \theta}\end{aligned}\tag{2.3}$$

Gathering (2.2) and (2.3) and substituting them into (2.1) gives the general equation for constructive interference in a Fabry-Perot Interferometer.

$$\begin{aligned}m\lambda &= 2 \left(\frac{\mu l}{\cos \theta} \right) - 2\mu l \frac{\sin^2 \theta}{\cos \theta} \\ m\lambda &= \frac{2\mu l}{\cos \theta} (1 - \sin^2 \theta) \\ m\lambda &= \frac{2\mu l}{\cos \theta} \cos^2 \theta \\ m\lambda &= 2\mu l \cos \theta\end{aligned}\tag{2.4}$$

If l , μ , and m are held constant, then (2.4) becomes a relationship between wavelength and angle of incidence. The angle of incidence is ideally equivalent to the outgoing angle of refraction. At $\theta = 0^\circ$, the transmitted wavelength is maximized for the given spacing, index of refraction, and order:

$$\lambda_o = \frac{2\mu l}{m}$$

where λ_o is the wavelength that will pass through the system on-axis. Using the above expression, (2.4) can be re-written in terms of λ_o .

$$\lambda_\theta = \lambda_o \cos \theta\tag{2.5}$$

The wavelength λ_θ is what will pass through the FPI given any off-axis angle. As the

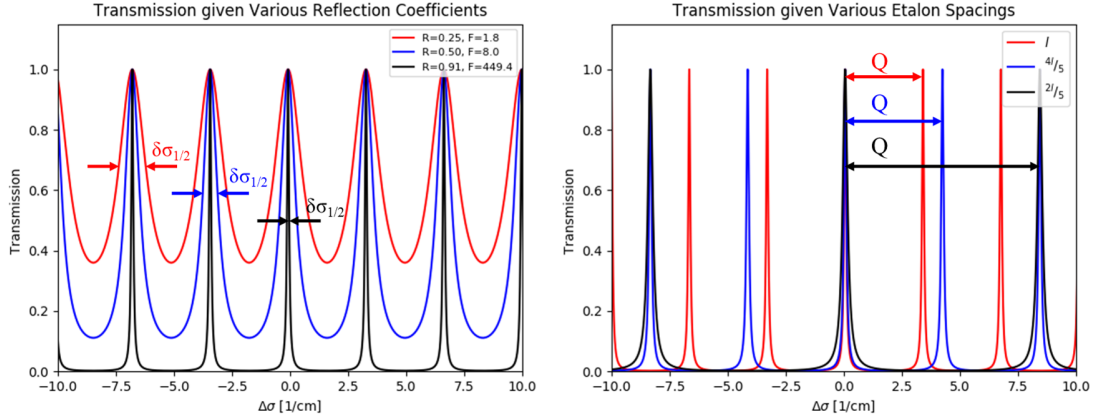


Figure 2.4: Varying the parameters of the FPI transmission function can change the transmission peak width and location.

incident angle approaches a maximum, the wavelength decreases; therefore the center of the interference pattern, the point on the image plane that intersects the optical axis, is where the reddest wavelengths pass through, and bluer wavelengths are found further off-axis.

A similar relationship can be defined for wavenumber, $\sigma = 1/\lambda$, where σ_o is the wavenumber that passes through on-axis and σ_θ is the wavenumber of any transmitted light that is off-axis.

$$\sigma_o = \sigma_\theta \cos \theta \quad (2.6)$$

This means that a transmission peak of order m will be located at the on-axis wavelength or wavenumber for an on-axis angle of incidence, but for off-axis angles of incidence, the transmission peak will fall at a bluer wavelength or wavenumber.

As seen in Figure 2.4, the transmission as a function of wavenumber, σ , for a Fabry-Perot etalon optical system is modeled by an Airy function, A [41].

$$A(\sigma) = \frac{1}{1 + \mathcal{F} \sin^2(2\pi\mu l \sigma \cos \theta)} \quad (2.7)$$

where \mathcal{F} is the *coefficient of finesse* given reflectance between the plates, \mathcal{R} ,

$$\mathcal{F} = \frac{4\mathcal{R}}{(1 - \mathcal{R})^2} \quad (2.8)$$

The transmission peaks are periodic with wavenumber or wavelength given a particular index of refraction μ , etalon spacing l , and angle of incidence θ . The wavenumber distance between transmission peaks is called the free spectral range (FSR) and is denoted by the symbol Q in cm^{-1} [41].

$$Q = \frac{1}{2\mu l \cos \theta} \quad (2.9)$$

The FSR in terms of wavelength, Q_λ in cm is given by

$$Q_\lambda = \lambda^2 Q \quad (2.10)$$

If $\theta \approx 0$ and $\mu \approx 1$, then the FSR is reduced to $Q = 1/2l$. This is the case for Figure 2.4, where it can be seen in the right panel that changes in l create changes in Q .

The sharpness of the transmission peak is determined by both the spacing and reflectance of the etalon, and is called the FWHM of the peak, denoted by $\delta\sigma_{1/2}$ [41].

$$\delta\sigma_{1/2} = \frac{Q(1 - \mathcal{R})}{\pi\mathcal{R}^2} \quad (2.11)$$

Or in terms of wavelength, the FWHM becomes

$$\delta\lambda_{1/2} = \frac{Q_\lambda(1 - \mathcal{R})}{\pi\mathcal{R}^2} \quad (2.12)$$

The left panel in Figure 2.4 shows how reflectivity affects the transmission function and the FWHM of each peak. FWHM is considered the spectral resolving limit, or the smallest separation between two resolvable peaks. It is common practice to discuss the FWHM in terms of *resolving power* when it comes to Fabry-Perot interferometry. Resolving power, R , is the ratio between the desired observation wavenumber (or wavelength) and the FWHM of the system in wavenumber (or wavelength) [41].

$$R = \frac{\sigma}{\delta\sigma_{1/2}} = \frac{\lambda}{\delta\lambda_{1/2}} \quad (2.13)$$

The resolving power is a common way of comparing the capability of one FPI to another. High resolving power means that the FPI was built to resolve small differences in the spectral dimension. Low resolving power FPIs cannot resolve small differences as well, but are capable of obtaining more signal per spectral bin. In many cases, higher resolving power is preferred.

To obtain high resolving power, the FPI designer should choose to maximize the etalon reflectivity and minimize the FSR by maximizing the etalon spacing. However, these design choices result in many transmission peaks in a given spectral range (corresponding to lower FSR), similar to the red line in the right panel of Figure 2.4. If the observer wishes to isolate a specific emission line and uses such a system tuned to the correct wavelength, then the resulting spectra will contain both her desired signal and any undesired signals corresponding to the surrounding transmission peaks. In order to avoid the unwanted emissions, multiple etalons of varying FSR can be utilized.

The transmission function of n etalons in series, A_{sys} , can be computed by taking the product of the transmission function for each etalon.

$$A_{sys} = (A_1)(A_2) \cdots (A_n) \quad (2.14)$$

This means that the resulting transmission is highest at the spectral ranges where each of the etalon's transmission peaks align. On the other hand, this also means that wherever each etalon's transmission peaks are out of phase from one another, there will be lower transmission. This concept can be used to suppress unwanted signal. In fact, in a dual etalon system, the first etalon in the light path is often called the suppression etalon, and the second etalon is called the resolving etalon. Figure 2.5 uses (2.14) to model the transmission function of a dual etalon FPI.

The resolving etalon ensures that the FWHM of the transmission peaks are low so that high resolving power is obtained, and the suppression etalon maintains a larger FSR so that the desired emission line can be isolated from undesired signals. The dual etalon system described in Figure 2.5 is an ideal representation of the INSpIRe FPI, inherited from Pine Bluff Observatory. Note that both etalons in Figure 2.5

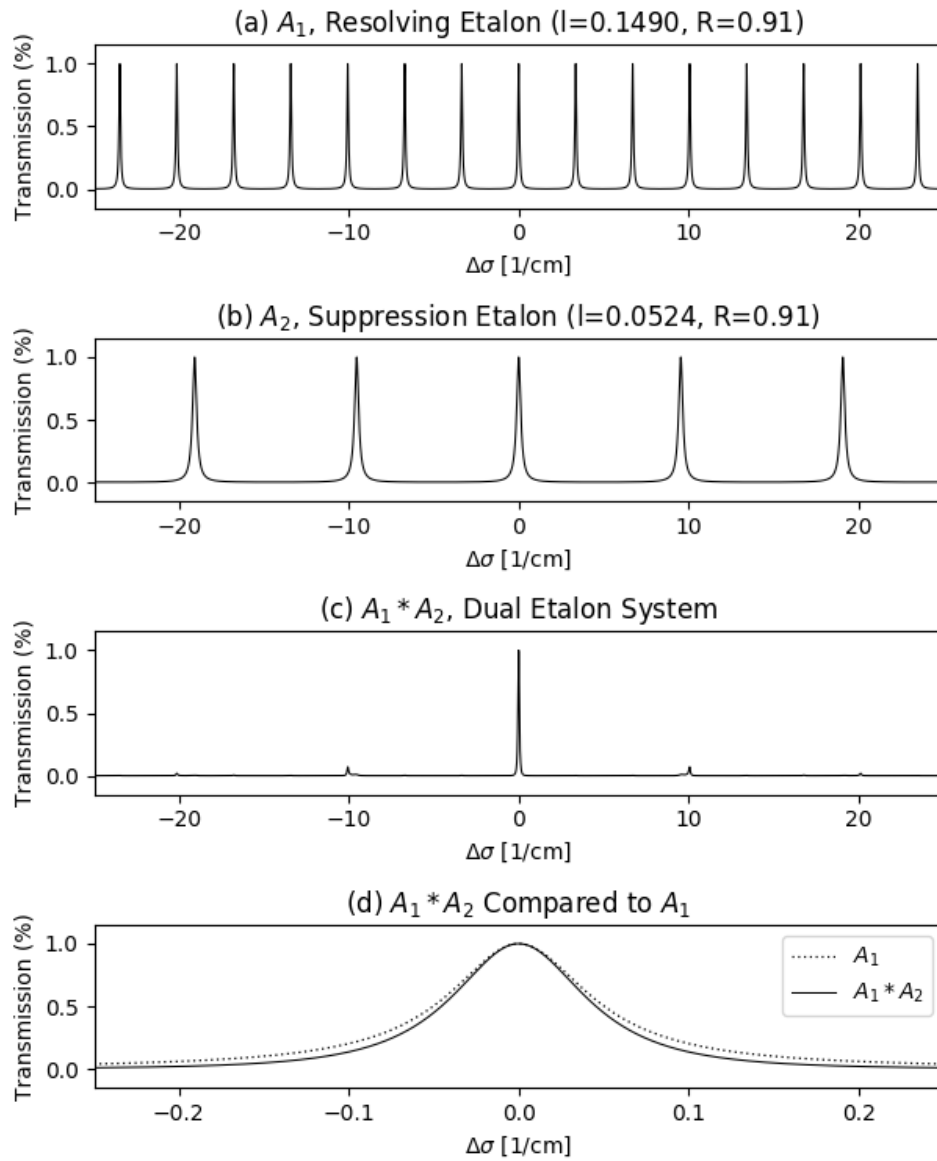


Figure 2.5: The theoretical transmission of the resolving etalon (a) and suppression etalon (b) is shown alongside the transmission function of the dual etalon system (c). Not only does the combination of the two etalons increase the FSR, but it also decreases the FWHM for higher resolution measurements, as visible in (d).

have a reflectivity of $R = 0.91$ and are tuned to the same wavenumber, so the only difference between the two is the fixed spacing of the etalons. When both etalons are combined, the transmission function shows a strong peak at the tuned wavenumber, and very weak peaks near the FSR of the suppression etalon. These weaker peaks create artifacts in the observed spectra that are often called *ghosts*, but for the most part, the higher orders are suppressed. The polyetalon system also has the advantage of decreasing the FWHM of the resulting spectra, as seen in (d) of Figure 2.5, due to the multiplication of the Airy function.

2.3 Tuning the Wavelength with Pressure

The polyetalon system only works if the entire system can be aligned to a particular wavelength. Furthermore, careful tuning of the etalons can result in a sharper transmission peak and higher resolution data can be obtained. FPI tuning commonly involves physically changing the etalon spacing l or the angle of incident light θ via very precise motors. In geocoronal hydrogen research, the FPI is tuned by changing the optical etalon spacing μl via pressure variations. This is done by changing the pressure of the medium that surrounds the etalons while the etalons remain physically unmoved, thus changing the refractive index of the medium rather than the physical spacing. Variations to the refractive index using this method are so minuscule compared to the physical etalon spacing that the FSR of each etalon is considered to be constant. The Investigating Near Space Interaction Regions (INSPIRe) observatory uses diatomic nitrogen (N_2) as the etalon chamber medium.

If the etalon was placed in a vacuum with $\mu = 1$, then the optical etalon spacing is simply l , the physical distance between the plates. However, if one were to fill the space between the plates with some medium, such as a gaseous substance, then the optical spacing becomes a function of the index of refraction of the medium, μl . For the case where $\mu \approx 1$, the Lorentz-Lorenz equation can be simplified to a linear relationship between refractive index μ and number density of the medium n .

$$\mu - 1 = 2\pi n\eta \quad (2.15)$$

where η is the molecular polarizability of the medium ($\approx 1.71 \times 10^{-30} \text{ m}^3$ for diatomic nitrogen [43]). Experimentally, it is easier to control the pressure than number density of an enclosed space, so it is convenient to substitute pressure for number density using the assumption that the gas is ideal.

$$\mu - 1 = 2\pi\alpha \left(\frac{P}{kT} \right)$$

Assume the medium is enclosed in a constant volume and held at constant temperature; given two pressure values, $P_o = 1 \text{ atm}$ and $P_f = P_o + \Delta P$, a system of two equations appear that depend on refractive index μ_o and $\mu_f = \mu_o + \Delta\mu$.

$$\begin{aligned} \mu_o - 1 &= 2\pi\alpha \left(\frac{P_o}{kT} \right) \\ \mu_f - 1 &= 2\pi\alpha \left(\frac{P_f}{kT} \right) \end{aligned}$$

If the two equations are divided, the constants cancel out, leaving a linear relationship between $\Delta\mu$ and ΔP .

$$\begin{aligned} \frac{\mu_o + \Delta\mu - 1}{\mu_o - 1} &= \frac{P_o + \Delta P}{P_o} \\ \Delta\mu &= \frac{\mu_o - 1}{P_o} \Delta P \end{aligned} \tag{2.16}$$

For diatomic nitrogen, the refractive index $\mu = 1.000294$ at standard pressure $P = 1 \text{ atm}$ [44]. This means that a pressure change of $\Delta P = 1 \text{ atm}$ above standard pressure will give a change $\mu = 2.94 \times 10^{-4}$ in the refractive index above the vacuum value.

Since most gases are not ideal, the error in the assumption that pressure can be substituted for number density is illustrated by the Van der Waal relationship between pressure and number density. For diatomic nitrogen, the empirical constants are $a = 1.370 \text{ Pa m}^6$ and $b = 0.0387 \text{ m}^3 \text{ mol}^{-1}$.

$$P = \frac{nVRT}{N_A \left(V - \frac{nVb}{N_A} \right)} - \frac{n^2 a}{N_A^2} \quad (2.17)$$

In (2.17), n is number density in m^{-3} , V is volume in m^3 , $R = 8.317 \text{ J mol}^{-1} \text{ K}^{-1}$ is the ideal gas constant, T is the temperature in K, and $N_A = 6.022 \times 10^{23} \text{ mol}^{-1}$ is Avogadro's constant. The pressure P is thus calculated in Pa, but Figure 2.6 shows pressure in mmHg, since this is the unit that is commonly used in the INSpIRe observatory. Figure 2.6 illustrates the deviation from an ideal gas for diatomic nitrogen (N_2), the gas that the INSpIRe observatory uses as a medium between the plates of each etalon. For this work, the deviation from an ideal gas is acceptable.

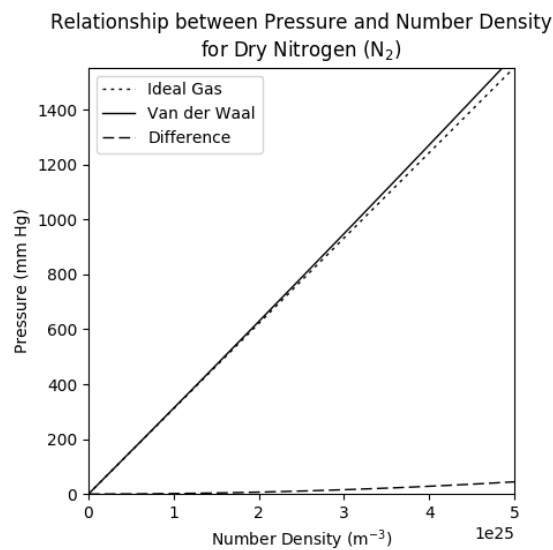


Figure 2.6: Van der Waal's equation (see Equation 2.17) represents the non-ideal gas. When this equation is substituted into the relationship between number density and pressure, we see that the difference isn't very large and so the ideal gas law is a good approximation.

Chapter 3

Observatory Systems

“I guess the question I’m asked the most often is: ‘When you were sitting in that capsule listening to the count-down, how did you feel?’ Well, the answer to that one is easy. I felt exactly how you would feel if you were getting ready to launch and knew you were sitting on top of two million parts – all built by the lowest bidder on a government contract.”

John Glenn,
American Astronaut

3.1 System Overview

The Investigating Near Space Interaction Regions (INSpIRe) observatory is housed in a custom 40-foot shipping container that sits on a concrete pad, shown in Figure 3.1. The shipping container was selected for its ease of ability to relocate. In shipping the observatory to its remote location, all non-optical components can be disassembled and secured inside of the container, including the dome. More sensitive equipment will be securely packed in crates and shipped separately.

The observatory is split into two rooms (see Figure 3.2), separated by an interior wall and door: one control room and one instrument room. The control room is where the control computer and electronics boxes are located. This room is separate so that light and heat from the control room during local control operations do not



Figure 3.1: The INSpIRE Observatory at Embry-Riddle Aeronautical University (ERAU). Photo credit: Maggie Gallant, October 2016.

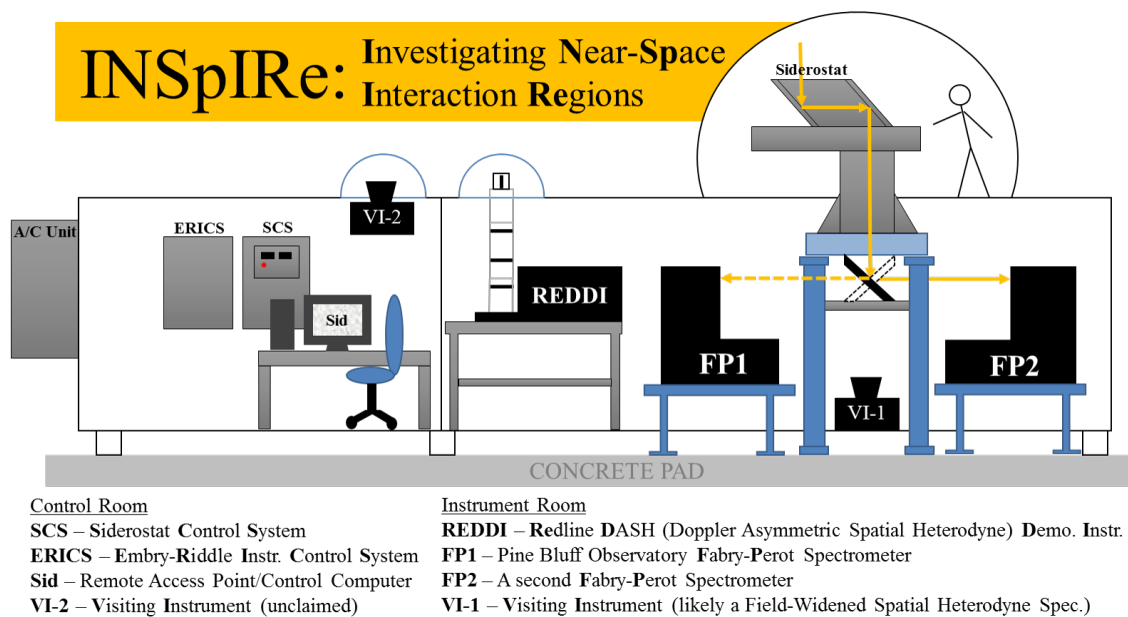


Figure 3.2: Five potential instruments are shown here, as well as the siderostat, electronics box locations, and control computer.

interfere with data collection in the instrument room. The instrument room is fitted with several holes in the floor that allow instrument stands and the siderostat pier to be bolted to the concrete pad and isolated from the housing structure to minimize instrument or siderostat vibrations. Vibrations could occur due to wind, the air conditioning unit or vacuum pump kicking on or people walking around inside the observatory. The instrument room is directly below the dome and siderostat, and the siderostat beam is brought down into the instrument room through a baffle for further redirection. Three piers hold up the siderostat and baffle.

The structure was designed to provide ports for five instruments. The siderostat assembly, coupled with a fold mirror, is capable of providing light to instruments on either side of the assembly and, given a fold mirror that can fold out of the way, straight down to an instrument below. There are also two small, clear plastic, immovable domes that reside in the ceiling of each the control room and the instrument room. The clear dome in the instrument room is already home to an instrument named Red-line DASH (Doppler Asymmetric Spatial Heterodyne) Demo Instr. (REDDI) which has been used to study the red OII line for signatures of thermospheric wind speeds from Daytona Beach [45].

Much of the selection and design of the various components that make up the observatory are based around the concept of remote operations. The objective is to be able to control all the necessary components from one centralized operations machine. The control computer, fondly referred to as ‘Sid’, is the point of contact for all operations. Figure 3.3 shows the data communications and connections between all of the major subsystems. Not all of the connections are directly made with the computer. For example, the siderostat and environmental sensors are routed through the Siderostat Control System (SCS).

The shipping container is connected to the campus electrical system (120 V provided) and ethernet (via fiber). There are electrical outlets and ethernet connections along the wall opposite the doors. An ethernet switch, provided by the ERAU Information Technology (IT) department, provides ethernet to each of the wall ports; the switch was installed with its own uninterruptible power supply (UPS) to ensure that remote operations are not suddenly lost in the event of a power outage. The

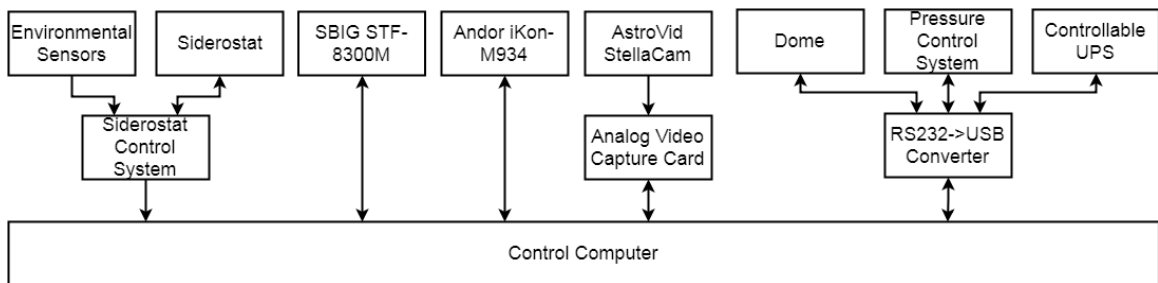


Figure 3.3: A diagram of the data communications shows that the control computer is the final point of contact for remote operations; it has access to all of the subsystems status updates and controllable features.

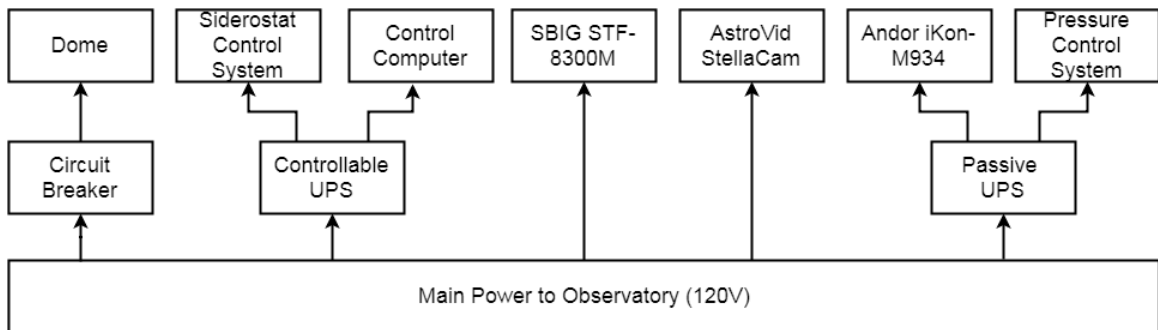


Figure 3.4: Power outages are a concern for a remotely operable observatory, so the important subsystems are powered through backup batteries. Technically, all of the systems connected to the main power are on a circuit breaker, but power to the dome is particularly dependent on the circuit breaker.

control computer and SCS are both connected to a remotely monitored UPS. A third UPS is installed in the instrument room and provides power outage protection for the Pressure Control System (PCS) and the Andor camera. The dome is powered via a connection to a covered GCFI power outlet on the roof of the observatory; when not in use, the dome gets powered down by flipping the circuit breaker to the roof outlet inside the observatory. Figure 3.4 shows a simple block diagram of the power connections.

Table 3.1: Necessary Python Modules

Module	Description
argparse	For interpreting command line arguments
astropy	For handling FITS files
cv2	Computer Vision library
datetime	Class for handling time variables
lmfit	Class for curve-fitting
math	Class for various math operations
matplotlib	Plotting library
numpy	Array operations library
os	Useful for handling paths in any OS
pylab	Supplementary plotting library
scipy.optimize	Data optimization library
scipy.interpolate	Data interpolation library
sys	Systems file operations library
re	Regular expressions library
timeit	Useful for execution timing

3.2 Control Computer & Software

In order to operate the observatory remotely, all of the subsystems need to be able to communicate with one central computer. The computer selected for the task is a Dell Optiplex 7020. Equipped with an Intel i5 QuadCore processor and 8 GB of RAM, the Optiplex 7020 works quickly and adequately in remote operations. Although the operating system (OS) is Windows 7 64-bit, compatibility with software and hardware systems has not been an issue.

The control computer is outfitted with LabVIEW 2017 and Python3 for developing and running control software. The observatory control software is dependent on three other software packages that are installed on the control computer: (1) a Flexible Image Transport System (FITS) file handling library called ‘gfitsio’, (2) the free FITS file viewing software ‘DS9’, and (3) the free media player ‘VLC’. Additionally, there is a suite of Python modules that must be installed, outlined in Table 3.1. Lastly, the siderostat control widget is dependent on a custom parameter calculator, the shadow code, which generates various pointing geometry parameters from the time, observer location, and local pointing measurements. The shadow code was written by Jeff

Pervical at University of Wisconsin (UW-Madison).

Windows Remote Desktop (native to Windows OS) is used to remote in to the control computer. ERAU IT gave the computer a static internet protocol (IP) address for this purpose and set up virtual private network (VPN) access for student observers (currently only the author of this thesis) to allow remote operations from off-campus. When the observatory is moved to its remote location, a new static IP will need to be assigned and VPN access provided for observers.

3.3 Uninterruptible Power Supply

Although three UPSs are in use at the observatory, only one of them is currently monitored. One of the concerns of remote operations is that the operations computer has to be powered on and accessible when it's needed, and a sudden power outage would immediately remove access to the operations computer. If a power outage occurs, the operator needs to be able to access the control computer long enough to put subsystems into a safe state before power is totally lost. For this reason, the control computer power is routed through a UPS that has monitoring capabilities. The Tripp-Lite SmartOnline SU1500XL provides six outlets on support from a 1200 watt UPS.

Communications with the UPS is accomplished over a serial connection. Table 3.2 gives two examples of commands that request information from the UPS. With the use of just these two commands, the user is able to determine whether the UPS is on battery (using the 'STO' command) and then if it is on battery, how much battery is remaining (using the 'STB' command). However, there are many other commands that can output or set parameters. For example, one setting determines whether or not to shut down the UPS after a certain number of seconds on battery, and another will run a test of the system on battery by impeding the input voltage for 10 seconds.

The control computer UPS will run on the internal battery for an estimate of ~15 minutes. This implies that operators need to know as soon as possible when the observatory experiences a power outage so that equipment can be powered down safely. This limits the remote site of the observatory to locations where personnel can

Table 3.2: UPS Serial Communications Summary

Serial Settings	
Baud Rate	2400
Parity	None
Data Bits	8
Stop Bits	1
Hardware	Off

Useful Serial Commands		
Command	Outputs	Notes
'~00P003STB'	Battery Condition	0=Good, 1=Weak, 2=Re- place
	Battery Status	0=OK, 1=Low, 2=Depleted
	Battery Change	0=Floating, 1=Charging, 2=Resting, 3=Discharging
	Seconds on Battery	[seconds]
	Estimated Minutes Remaining	[seconds]
	Estimated Charge Remaining	[%]
	Battery Voltage	[0.1 V]
	Battery Current	[0.1 A]
	Temperature	[° C]
	Battery Level	[%]
	'~00P003STO'	Output Source
Output Frequency		[0.1 Hz]
Output Number of Lines		[# of lines]
Output Voltage		[0.1 V]
Output Current		[0.1 A]
Output Power		[W]
Output Load		[%]

be called to help out in an emergency.

3.4 AstroHaven Clamshell Dome

The dome, used to protect the siderostat from external conditions, is a 12-foot clamshell-style AstroHaven Enterprises dome, pictured in Figure 3.1. It is constructed from fiberglass using a closed-mold vacuum infusion process, making it lightweight and able to stand up to very strong winds. It has a three-foot-tall base with a small entrance/exit hatch, and two leaves that move up and down on either half of the dome to open or close it. The dome was shipped to Daytona Beach in summer 2014 and assembled and installed over two days with the help of two ERAU professors, four ERAU students (the author included), and one visiting astronomer from NASA Goddard Spaceflight Center. The dome was craned on to the top of the shipping container by Bryson Cranes. The shipping container is only 10 ft wide, so custom shelves were built out on either side of the shipping container to accommodate the 12-foot diameter of the dome.

The leaves of the dome are controlled via a belt and pulley system driven by a motor (see Figure 3.5). As in Figure 3.6, two separate belt systems exist: (1) the inner leaf is controlled directly by the motor through a belt system that is constrained at the bottom edge of the leaf, goes through a pulley at the top of the base, and then is connected to the motor, and (2) the outer leaf is indirectly controlled by the motion of the inner leaf, since its belt is constrained at the bottom edge of its leaf, goes through a pulley at the top of the inner leaf, and is also constrained at the top of the base. When closing the dome, or moving the leaves upward, the motor is actively increasing tension to the belt system. When opening the dome, the motor gradually releases tension from the belt system, and allows gravity to pull the leaves downward. When the leaves are not moving, the motor and pulley system lock to passively maintain tension and hold the leaves in place. If the dome is fully closed or fully open, a limit switch is activated to shut off power to the motor.

A nice feature of this dome is that it came with remote control capability. The available functionality includes opening and closing each half of the dome individually



Figure 3.5: The motor and pulley system, located on the inside of the dome.

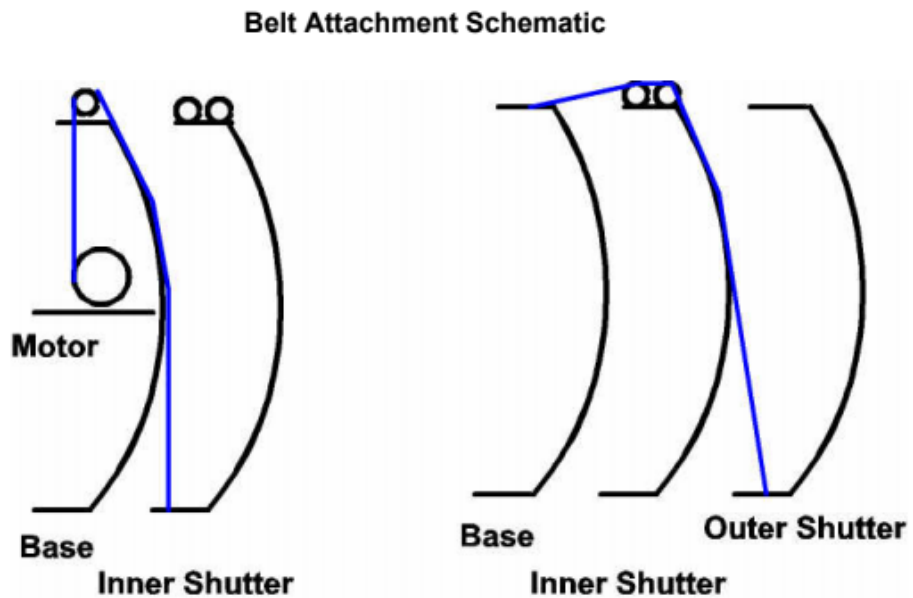


Figure 3.6: Two separate belt systems exist for each the inner leaf and the outer leaf. The inner leaf belt system is driven by a motor, and the outer leaf belt system is indirectly driven by the motions of the inner leaf. Credit to AstroHaven Enterprises.

Table 3.3: Dome Serial Communications Summary

Serial Settings	
Baud Rate	9600
Parity	None
Data Bits	8
Stop Bits	1
HW	Off

Serial Commands	
'A'	Move WEST leaf UP
'a'	Move WEST leaf DOWN
'B'	Move EAST leaf UP
'b'	Move EAST leaf DOWN

Serial Command Responses	
'A'	Successful WEST UP movement
'a'	Successful WEST DOWN movement
'B'	Successful EAST UP movement
'b'	Successful EAST DOWN movement
'X'	WEST UP movement hit limit
'x'	WEST DOWN movement hit limit
'Y'	EAST UP movement hit limit
'y'	EAST DOWN movement hit limit

Serial Idle Responses	
'0'	Both WEST and EAST are at UPPER LIMIT
'1'	EAST is open and WEST is at UPPER LIMIT
'2'	WEST is open and EAST is at UPPER LIMIT
'3'	Both WEST and EAST are open

via incremental steps and reporting the state of the dome: whether it's fully open, partially open, or fully closed. Serial communication is accomplished via RS-232 connection. Because there are separate commands for each half of the clamshell, only one half of the dome may be moved up or down at any given time. Also, the state of the dome is reported automatically, but only when the user is not currently sending commands. The manufacturer suggests sending the same command repeatedly until the dome is in the desired configuration. For example, to move the west half of the dome from open to closed, the user would type 'A' repeatedly into a serial terminal until the limit switch is tripped, at which point the serial terminal will respond with 'X' instead of echo-ing 'A' to indicate that the leaves are fully closed. There is no serial feedback in between the open or closed configurations, so visual feedback of the dome would be necessary if the user wanted to have one half of the dome somewhere in between the two states. A table of the serial settings and serial commands can be found in Table 3.3.

Through testing, it has been discovered that when the weather is very hot and humid, the rubber edges at the top of the outer leaves tend to stick together. If this happens and the motors are told to release tension from the belt system, then slack is introduced into the system and the only thing holding the leaf up is the fact that it's sticking to the leaf on the opposite side. Given time or enough slack, the outer leaf will release due to its own weight and free-fall until it makes up the slack in the belt. In order to prevent unnecessary stress on the belt system, it is preferred that the outer leaf go into free-fall for the shortest possible distance. Because of this, the normal procedure for opening the dome requires a "pre-open" step, where one half of the dome is opened by exactly one step, or about three inches, in order to help separate the halves and let any slack in the belts tighten before any further movements occur.

3.5 Siderostat Control System

The Siderostat Control System (SCS) is what directs communications between the control computer and the siderostat motors and between the Environmental Sensor System (ESS) and the control computer. A block diagram of the subsystem can be

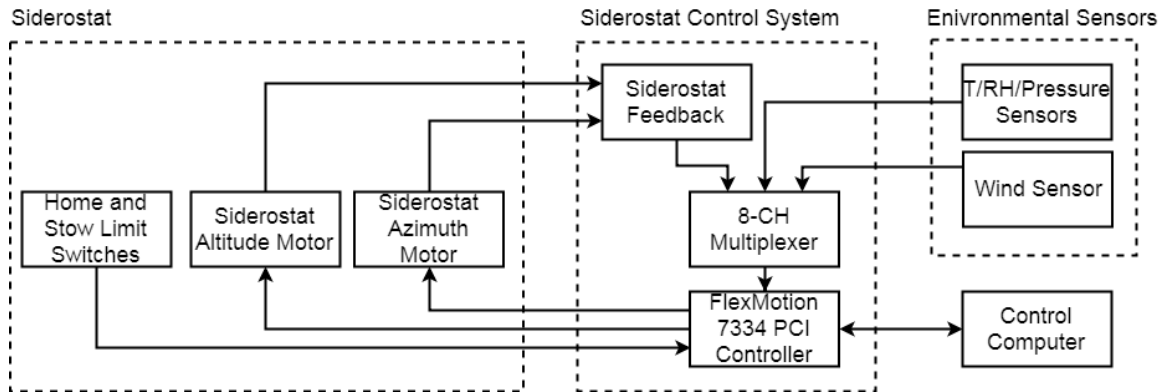


Figure 3.7: The SCS is made up of three major components: (1) the Siderostat Control System electronics box, (2) the siderostat, and (3) the environmental sensors that monitor the observing conditions.

seen in Figure 3.7.

3.5.1 Siderostat

The INSpIRe siderostat (see Figure 3.8) is effectively a 16" telescope when used with a 16" focusing lens at the base, but unlike standard telescopes, it uses two plane mirrors in a periscope configuration to fold light into the observatory. It has two rotation axes controlled by stepper motors: one that rotates the first mirror in the optical path about the yaw axis to control altitude, and one that rotates the entire siderostat to control azimuth. Each axis has a 'Home' and a 'Stow' state, where 'Home' (Alt: -102° , Az: 98°) and 'Stow' (Alt: 90° , Az: -73°) are defined by the machine coordinate system origin. The siderostat and SCS electronics box were repurposed by UW-Madison Systems Engineer Kurt Jaehnig for use in the INSpIRe observatory. It's original use was at the UW-Madison Pine Bluff Observatory (PBO) to collect galactic Hydrogen- α data. The siderostat, SCS, and ESS were installed in December 2015 by Jaehnig with the assistance of ERAU students and faculty.

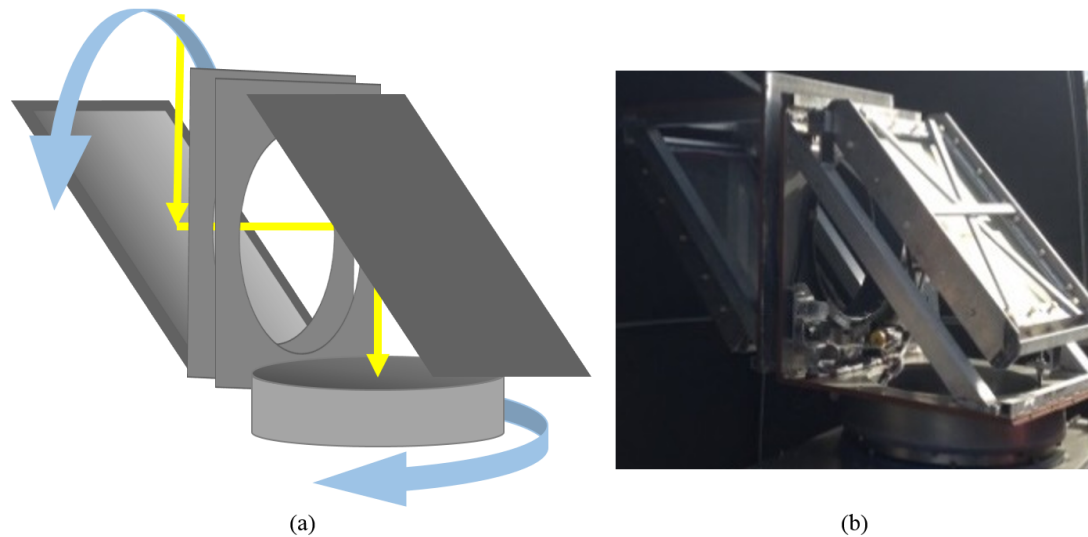


Figure 3.8: (a) The siderostat consists of two plane mirrors and two rotational stages. The first mirror in the optical path rotates about the yaw axis, and both mirrors (the whole siderostat) are rotated to control the heading. (b) An actual image of the INSpIRe siderostat, after installation in Daytona Beach.

3.5.2 Control Board

At the heart of the SCS is a National Instruments Flex Motion 7334 peripheral component interconnect (PCI) controller. The 7334 has a 68-pin Motion I/O port, with room for up to four axes of motion. The main features of the Flex Motion board used by the siderostat are the motor clockwise and counter-clockwise movement commands and the forward, home, and reverse limit monitoring on two axes. There are also four analog data inputs (and four corresponding analog calibration inputs) to the 12-bit analog-to-digital converter (ADC) on-board the 7334 PCI. An 8-channel multiplexer that feeds into these ADC inputs allows up to 32 different analog measurements, which are used to monitor SCS power and feedback from the ESS (see Section 3.5.3).

The Flex Motion 7334 PCI controller came with a library of commands that are wrapped and callable in LabVIEW. Modular code blocks exist for turning the stepper motor a certain number of steps, homing or stowing it by using the ‘Home’ or ‘Stow’ limit switch feedback, and reading out the ADC.

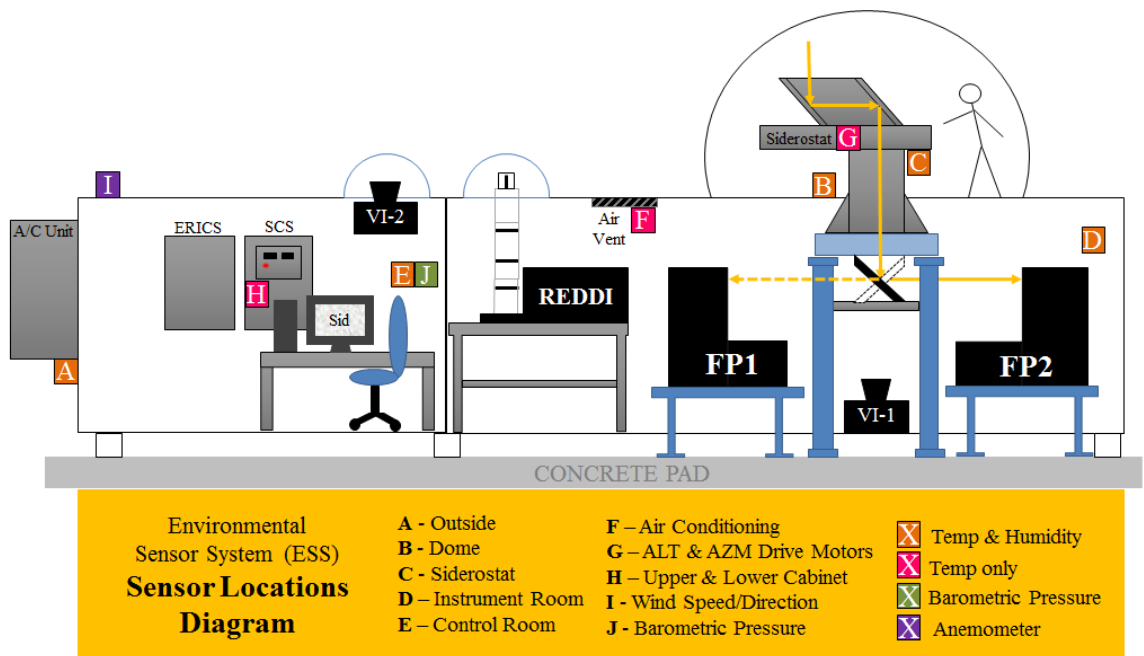


Figure 3.9: The ten sensor locations within and around the observatory are shown here.

3.5.3 Environmental Sensors

As part of the SCS, the ESS uses three types of environmental sensors to monitor the indoor observatory environment and the environment outside of the observatory. Figure 3.9 shows the location of each sensor. There are five combined temperature and humidity sensor boxes, three temperature sensor boxes, one barometric pressure sensor box, and one anemometer. In all, the ESS provides 18 different measurements regarding the observatory environment. The temperature, temperature/humidity, and pressure sensors are all commercial off-the-shelf (COTS) parts from Omega Engineering. The wind sensor is an ultrasonic anemometer from Gill Instruments Limited.

Omega Environment Sensors

The Omega Engineering sensors come in a variety of flavors, as outlined in Table 3.4. One of the varieties, the HX93A, is outdoor-rated, and two of these are installed: one under the air conditioning unit and one in the dome. The HX93A measures

Table 3.4: Summary of Omega Engineering Sensors

Model	Type	Range		Qty	Locations*
		Max	Min		
HX93A	Rel. Humidity	3%	95%	2	A, B
	Temperature	-20° C	75° C		
EWS-RH	Rel. Humidity	5%	95%	3	C, D, E
	Temperature	-15° C	60° C		
EWS-TX	Temperature	-18° C	57° C	3	F, G, H
EWS-BP-A	Bar. Pressure	528.3 torr	812.8 torr	1	J

* Reference Figure 3.9

both relative humidity and temperature, providing outdoor weather statistics. The other dual sensor is indoor-rated; there are three EWS-RH sensors: one in the dome shielded by the siderostat, one in the instrument room, and one in the control room. These provide information about the observing environment. There are also three temperature-only sensors, located at the air conditioning vent in the instrument room, inside the siderostat, and inside the siderostat control system electronics box. These three sensors are most useful in monitoring the state of the air conditioning unit and the state of the siderostat electronics. The temperature sensor at the air conditioning vent shows how often the air conditioning unit powers on and off throughout the day; because the thermostat does not automatically switch between heating and cooling, it is a useful gauge for determining when the thermostat should be adjusted. The last sensor available for monitoring is the EWS-BP-A, which measures barometric pressure inside the observatory. This gives a measure of the current atmospheric pressure for comparison to measurements from the pressure control system.

Currently, the Omega sensors installed at locations A and G (refer to Figure 3.9) are not available for monitoring. The HX93A located under the air conditioning unit is outdoor-rated up to 95% humidity, but it has been outputting erroneous humidity values over 100%. Temperature values from the outdoor sensor are still reasonable. The HX93A has since been discontinued and a suitable replacement has not yet been identified. The plan for replacement is to switch the HX93A sensors at locations A and B when the observatory is deployed to its remote site in a much drier climate, so as not to break both sensors while it resides in Florida. The EWS-TX located at

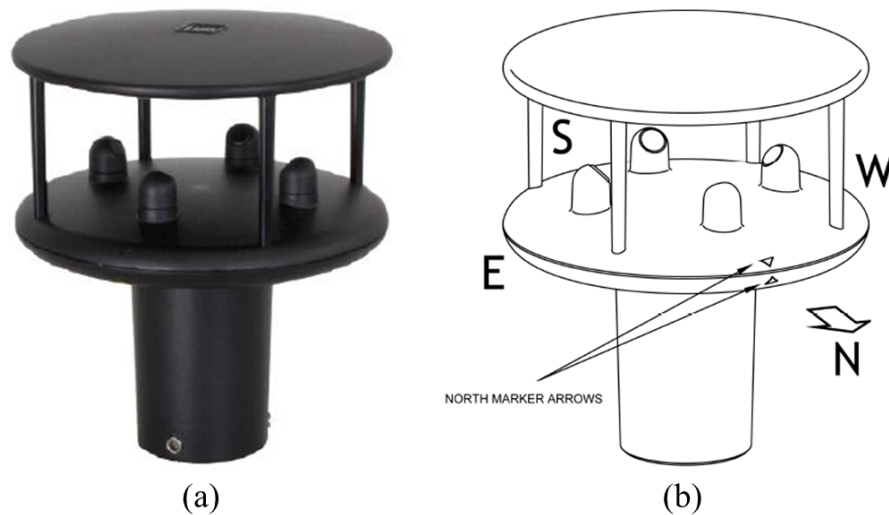


Figure 3.10: (a) A stock image of the anemometer in anodized aluminum. Credit to Gill Instruments Limited. (b) A diagram of the ultrasonic transducers in the N-S, E-W configuration. Credit to Gill Instruments Limited.

the siderostat motors in the dome has also started outputting erroneous values to the tune of -100° C. A likely cause for this issue, although it is not confirmed, is that a family of wasps has moved in to the sensor housing. Luckily, the EWS-TX has not been discontinued and we can buy an identical replacement for this sensor.

Wind Sensor

Wind speed, particularly gust speed rather than sustained, is important to monitor while observing. Although the sky may be clear of rain or clouds, high wind speeds can be hazardous to the equipment or local observers. One of the possible locations for the INSpIRE remote site is Kitt Peak National Observatory (KPNO), where wind speeds are known to exceed 45 MPH from time to time. For this reason, a two-dimensional ultrasonic sensor from Gill Instruments Limited was selected for its ability to measure wind speeds from 0 to 60 ms^{-1} (0-134 MPH). The WindSonic Ultrasonic Anemometer (see Figure 3.10) uses two pairs of ultrasonic transducers to measure wind speeds in perpendicular directions, and then does a vector calculation to determine the horizontal wind speed and direction. Each transducer in the pair

transmits an ultrasonic pulse to the other transducer, so that the time of flight between the transducer pair is measured in both directions, t_1 and t_2 (e.g. from North to South and from South to North). The distance between the transducers, L , is also known, and so the wind speed, w , between one transducer pair is given by

$$w = \frac{L}{2} \left(\frac{1}{t_1} - \frac{1}{t_2} \right) \quad (3.1)$$

The wind speed is calculated between each pair and then vector analysis determines the true wind speed and direction. Note that this calculation is independent of temperature, pressure, or humidity changes. However, the ultrasonic transducers are sensitive to disruptions in the transducer pair's transmission path, including raindrops. To prevent this, the WindSonic sensor housing includes a roof to keep rain from entering the transmission path. The major drawback of ultrasonic sensors are that the physical structure of the transducers and housing can redirect wind flow, but Gill Instruments Limited states that their anemometer has been experimentally calibrated in a wind tunnel to minimize this effect.

The WindSonic analog output has two channels: one for wind speed in meters per second and one for wind direction between 0 and 359 degrees. If the wind speed measures below 0.05 ms^{-1} (0.11 MPH), then the wind direction output is no longer reliable. According to Gill Instrument Limited, the WindSonic's default action in this case is to output the last known valid wind direction value.

3.6 Fabry-Perot Interferometer

The first FPI has been inherited from the UW-Madison group and re-purposed for use in the INSpIRE observatory. This FPI is the first of two planned installations to share the siderostat beam. It was originally a photomultiplier tube scanning FPI, but it was refurbished with a charge-coupled device (CCD) [40], and used in several observing campaigns [46, 47]. Ultimately, the retrofit did not take full advantage of the CCD imaging technique, and further re-designs were completed in 1999 [48].

Figure 3.11 traces the optical path of the FPI, assuming that the FPI were directly

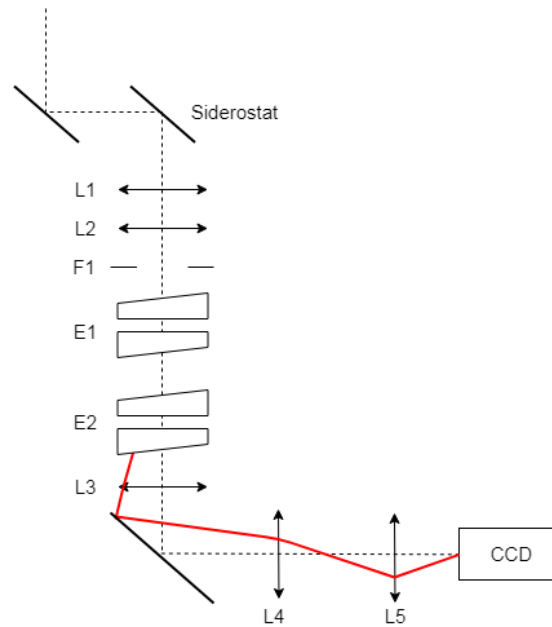


Figure 3.11: All of the optical elements of the Fabry-Perot interferometer (FPI) laid out in the optical path. The red ray trace shows the path of a ray that exits the fringe-imaging lens (L3) right at the edge.

under the siderostat. In actuality, the FPI is not directly under the siderostat beam, and there would have to be a series of fold mirrors in between L2 and F1. The FPI consists of two pressurized chambers, two 6-inch etalon pairs (E1 & E2), a 6-inch fringe-imaging lens (L3), a 10-inch fold mirror, a field lens (L4), a telephoto lens (L5), and a CCD detector. The three pressure chambers are connected vertically and are separated from each other by fused silica glass windows. The two etalon pairs each sit in their own chamber, which are held at a known pressure using the PCS (see Section 3.7). Since FPI fringes are imaged at infinity, the L3 attempts to minimize vignetting at the edges of the image by reducing the beam size. The fold mirror then transforms the vertical optical path into a horizontal optical path by folding the beam towards the detector. The beam is collimated at L4 and brought into focus by L5, so that the detector can capture the image of the fringe pattern.

The first step of alignment was to define the optical axis. This was done using a laser beam and several precisely-machined pinhole apertures to limit the beam size and centering of the optical axis. Throughout this process, optics are introduced one

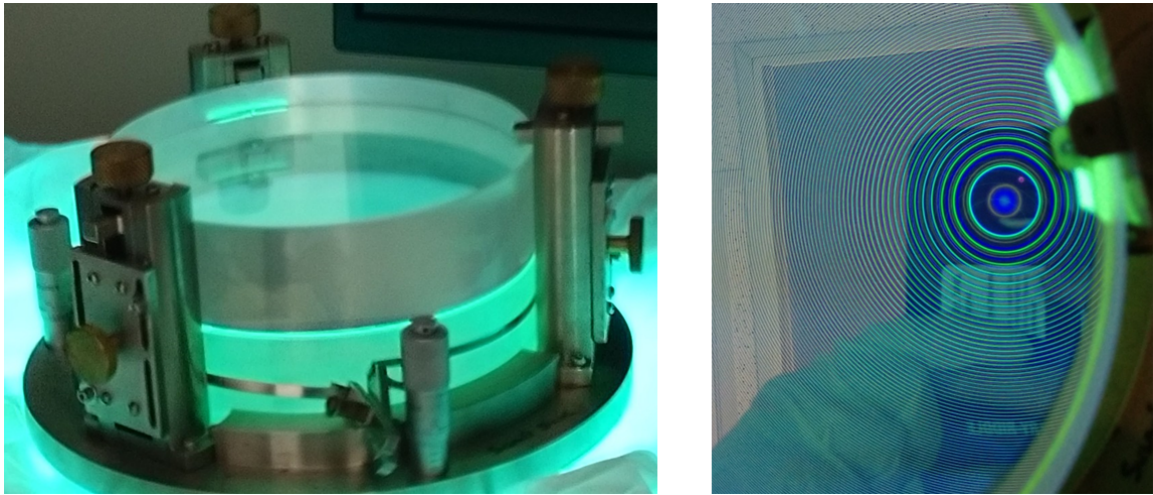


Figure 3.12: The low-resolution FPI etalon before installation. (Left) The etalon is sitting on a mercury lamp. (Right) Green and blue mercury emission fringes as seen through the etalon and imaged by the color CCD on the author's smartphone. Fringes are imaged at infinity, so the annuli are concentric and centered on the lens of the imager.

at a time and the system is re-aligned at each step. An auto-collimation technique was used to ensure that the collimating optics were placed at the correct focal length. The etalons were installed last; first the low-resolution etalon, and then the high-resolution etalon. Preliminary testing after each etalon installation can be found in Chapter 5.

In order to align the optical elements of the FPI to a defined optical path, two mounting assemblies had to be designed and machined: one for the 6-inch fringe-imaging lens (L3), and one for the detector.

3.6.1 Lens Mount

The 6-inch fringe imaging lens was originally sitting in a holder with fine-tuning set screws to help translate the lens perpendicular to the optical axis. The custom lens holder was somehow lost in the FPI move from Wisconsin to Daytona Beach, and so a new lens holder had to be designed. There were no pictures of the original lens holder, but the basic requirements were understood. The lens holder needs to securely hold

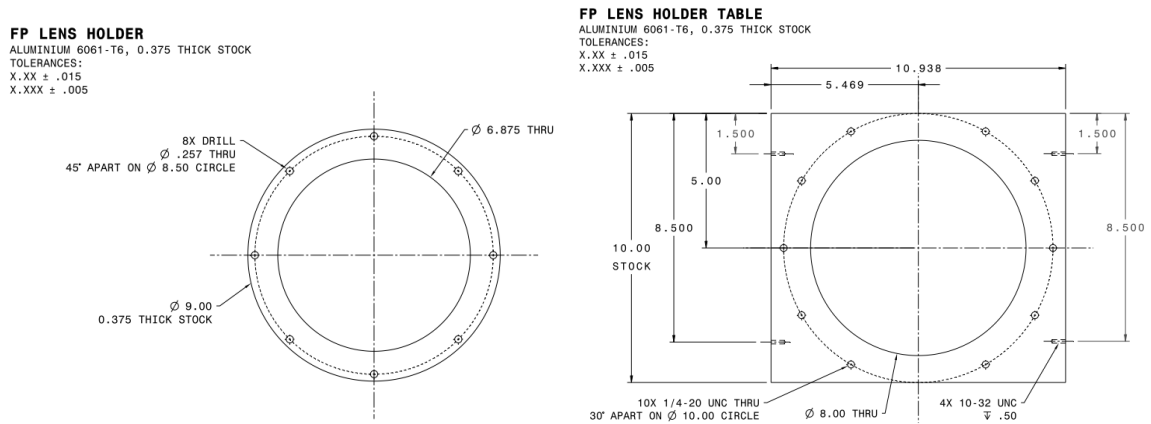


Figure 3.13: (left) The lens holder is meant to hold the 6-inch fringe-imaging lens securely by a lip around the edge of the lens. (right) The lens holder table holds the lens holder with enough tolerance to allow 0.5 inches of translation in all directions. Not to scale.

the lens so that it does not fall (it would fall on to another optical element and most likely hurt itself and the other optics), and the lens holder needs to provide some mechanism for translating the lens.

The design turned out to be a set of two plates, shown in Figure 3.13. The top plate would hold the lens by the lip of its housing; the lens housing simply sits down in a hole in the plate. The bottom plate would support the top plate and allow the lens and lens housing to drop down into a larger hole. The hole in the bottom plate needed to be large enough to allow the top plate to translate by 0.5 inches in every direction and the hole needed to be small enough that the top plate would not fall through when translated. The lens housing was measured to be 6.865 inches in diameter, and so the hole in the bottom plate was designed to be 8 inches in diameter to allow for the desired translation. To secure the top plate once it is translated as needed, there are holes in the bottom plate that allow a table clamp to be secured over the top plate and fastened to the bottom plate. The holes are placed so that at maximum translation three table clamps can still be used at once.

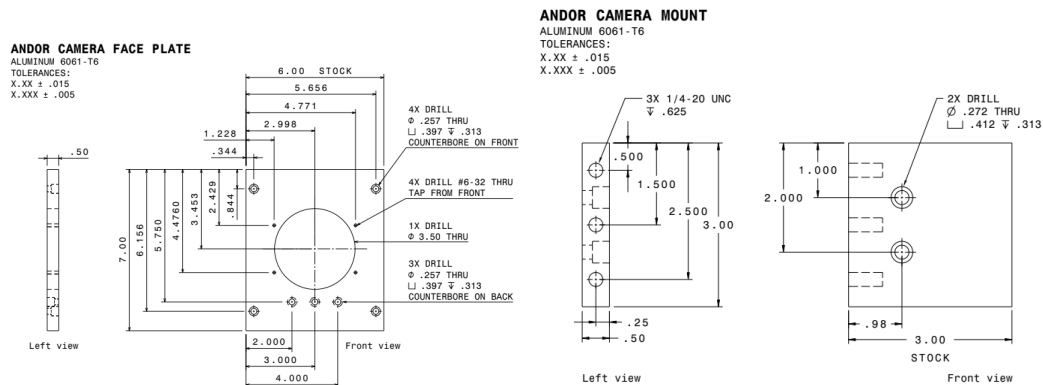


Figure 3.14: (left) The camera mount face plate includes tapped holes for securing the camera to the face plate and a large thru-hole for the telephoto lens to fit through. (right) The camera mount shelf attaches to the face plate below the camera and provides some extra support. Not to scale.

3.6.2 Camera Mount

The original camera mount was cleverly designed to translate perpendicular to the optical axis using two plates with slot attachments; to translate the camera, move the plates along the slots. The top plate is equipped with a box that holds the camera. The FPI fringes were originally imaged with a Photometrics CCD attached to the FPI after the mirror fold. A new detector was selected to replace the outdated detector, and the new detector (the Andor iKon-M934) has a different mounting hole pattern. Therefore, a new face plate to mount to the camera mount holes was required.

Figure 3.14 shows the new face plate design. The new face plate was designed to fit flush with the original mounting box and use the same screw holes as the original plate. Tapped holes allow the camera face to mount to the plate, and a thru-hole allows the camera to see through the plate. A shelf was placed below the camera to provide extra support, since the iKon-M934 is a rather long detector.

3.7 Pressure Control System

The FPI etalons sit in sealed chambers that are pressurized by the Pressure Control System (PCS). The PCS was developed for FPI instrument control by Kurt Jaehnig



Figure 3.15: The PCS consists of a pneumatics rack (top) and an electronics rack (bottom). The physical user interface is on the bottom rack.

at UW-Madison and a set of control commands was written in Forth by Jeff Percival, also at UW-Madison. The electronics rack consists of a Mosaic Industries QED-Flash v4 microcontroller board and two Heise high-precision pressure transducers, alongside a physical user interface with indicator LEDs, an LCD screen, and valve and target pressure controls. The electronics rack is connected to the pneumatics rack, which transmits signals from the microcontroller or the physical user interface to close or open valves. The pneumatics rack is connected via gas lines to the two pressurized etalon chambers. The valves in the pneumatics rack either let gas in from a tank of dry nitrogen (N_2) or exhaust gas from the chambers. With this method as is, the chambers can only achieve atmospheric pressure or higher. To go below atmospheric pressure, a vacuum pump is necessary. The PCS includes a line to connect a vacuum pump, but does not include the feature to automatically turn the vacuum pump on or off when needed.

The system simply closes and opens gas or exhaust valves until the readings from the pressure transducers match the given target pressure. It checks and adjusts

Table 3.5: PCS Serial Communications Summary

Serial Settings	
Baud Rate	9600
Parity	None
Data Bits	8
Stop Bits	1
HW	Off

Start-up Commands

```

'dcpc.init'
'start.up'
'hex'
'9600 0 task: dcpc.bg'
'0\0 0\0 0\0 dcpc.bg build.standard.task'
'decimal'
'cfa.for sntp.loop dcpc.bg activate'

```

Common Commands

'st'	Display status report
'ap <target value>'	Set Chamber A pressure to <target value>
'bp <target value>'	Set Chamber B pressure to <target value>
'a.src.dac'	Set CHA control source to computer control
'a.src.pot'	Set CHA control source to physical interface control
'a.loop.open'	Open CHA pressure circuit (inhibit pressure changes)
'a.loop.close'	Close CHA pressure circuit (enable pressure changes)

continuously in closed loop mode. In this way, the loop setting (closed or open), enables or inhibits pressure changes in the system. Additionally, if the system is in ‘DAC’ control mode, the target pressure comes from the microcontroller. If the system is in ‘POT’ control mode, the target pressure comes from the physical user interface. Both the loop mode and the control mode are able to be set via serial communications (see Table 3.5). When in ‘DAC’ control mode, the target value can be set by using a serial command. Each chamber, chamber A and chamber B, are individually controlled and can be in closed loop mode simultaneously. In order to get feedback over serial communications, the command ‘st’ will elicit a status response from the controller. The response is a full report of the available information at the time of response, which includes statistics for both chambers, as well as information about which gas lines are connected and a timestamp.

3.8 Charge Coupled Devices

Data collection is truly dependent on having a controllable charge-coupled device (CCD) to capture the FPI fringes. There are two CCDs as part of the INSpIRE observatory that can be used to collect data. These are the Andor iKon-M934 and the SBIG STF-8300M. A third CCD, the Astrovid StellaCam, only outputs in analog video and is best used as a guide camera, to display to the user what the siderostat is pointed at.

The imaging sensor of a CCD is divided into light-sensitive capacitor cells, known as pixels, that convert photon counts into stored charge. The effectiveness of the material of the CCD in converting photons into electron charge is parameterized by the quantum efficiency of the CCD at every wavelength. No CCD is 100% efficient, but higher efficiency is desired at the wavelengths to be observed. Once charge is accumulated in each cell, the charge in each cell of the first row is read out, and then the charge in each cell of the next row, and so on. Positive voltage is applied to transfer charge from one cell to its neighbor to “move” the rows towards the voltage readout. Because of this process, CCDs are susceptible to read noise, either from pixel-to-pixel inconsistencies in the charge amplifier readout, or from charge that gets

left behind in the transfer process (the image will look brightest on the readout end of the chip). Another useful parameter for assessing the quality of a CCD is its dark current, which represents the amount of electrical noise in the system even when there aren't any photons to interact with the capacitors. This is measured by taking images with the camera's shutter closed and is ideally close to zero. Higher chip temperatures increase the dark current, so camera cooling can mitigate this effect. Even though various sources of noise must be accounted for, since its popularity among astronomers exploded in the 1990s, the CCD has vastly improved the quality and efficiency of data collection in astronomy.

3.8.1 Andor iKon-M934

The iKon-M 934, as seen in Figure 3.16, has a 1024 by 1024 pixel sensor with a pixel size of 13 microns (sensor size is 13.3 by 13.3 mm). The quantum efficiency at the visible spectrum is around 95%. It has several readout modes with varying readout rates (and corresponding read noise) for use in different applications. The fastest readout (for focus or calibrating camera settings) reads the full chip in ~ 0.3 seconds with a readout noise of $18.0 e^-$, while the slowest readout setting reads the full chip in 20 seconds with a readout noise of $2.9 e^-$. With the included air circulation cooling system, the chip can get down to -80° C below ambient temperature, bringing the dark current down to $0.0003 e^- \text{ pix}^{-1} \text{ s}^{-1}$.

The Andor detector has three modes of operation. The first is single image mode, where it takes one image when it is told to do so. The next is series mode, where it takes a specified number of images when it is commanded. The third is video mode, where it takes a continuous stream of images until told to stop.

The Andor camera was selected for use with the FPI for two reasons: (1) this model has been used in the past to take FPI fringe images on another system with great success [37] (and therefore the INSpire group is familiar with its mounting and cooling mechanisms), and (2) Andor is known for providing good quality data at a mid-level price point compared with competitors (\sim \$30k). Andor offers a Software Development Kit with a library of commands wrapped in LabVIEW.

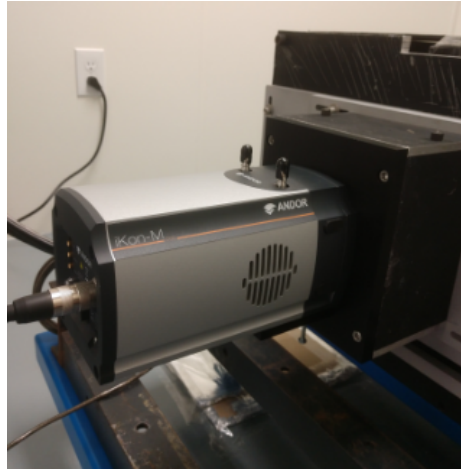


Figure 3.16: The Andor iKon-M934 detector in its camera mount and attached to the exit of the FPI.

3.8.2 SBIG STF-8300M

The SBIG STF-8300M chip consists of 5.4 micron pixels in a 3326 by 2504 pixel configuration (sensor size is 17.96 x 13.52 mm), making this a fairly large, high resolution chip. The peak quantum efficiency is 56% close to 5500 Å. There's one readout setting, which reads the full chip in ~ 0.8 seconds with an associated read noise of $9.3 e^-$. The cooling system has a cooling delta of about $35^\circ C$ from the ambient temperature. When the chip is cooled to $0^\circ C$, the dark current is $0.15 e^- \text{ pix}^{-1} \text{ s}^{-1}$.

The SBIG detector has very similar modes of operation to the Andor camera. It can either grab one image, a specific number of images, or a continuous stream of images. Instead of calling the last mode 'video mode', SBIG calls it 'focus mode'. It's also equipped with an external filter wheel filled with eight different Baader Planetarium imaging filters: clear, luminance, R, G, B, H- α , SII, and OIII. The installed filters cannot be used for FPI observations, except for the clear filter, so this camera is currently set up as a guide camera instead of an FPI imager.

SBIG cameras are known in the astronomy community for providing fair quality data for a very low price point ($\sim \$2k$). However, the read noise, quantum efficiency, and dark current fall short of the Andor iKon-M934. SBIG does not provide a library of LabVIEW commands, but does provide drivers that can be wrapped in LabVIEW.

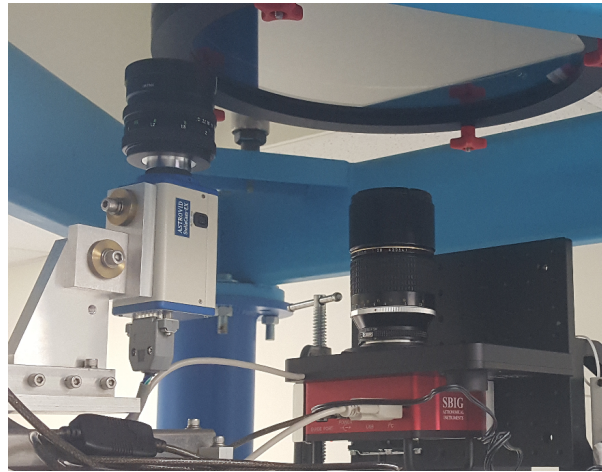


Figure 3.17: The SBIG STF-8300M and the Astrovid StellaCam-EX mounted beneath the siderostat beam.

The SBIG is not currently in use, but it occasionally works well as a guide camera in the case that higher quality data output than the Astrovid output is desired. See Figure 3.17 for an image of the camera mounted under the siderostat. The SBIG STF-8300M was used to take our first light image of the moon during initial siderostat pointing tests (see Chapter 5).

3.8.3 Astrovid StellaCam-EX

Astrovid is currently out of business and no longer has a working website, so not all of the same technical specifications are available for this CCD. The imaging sensor is a Sony ICX248AL with an array of 811 x 508 pixels of size 8.4 microns (sensor size 7.95 x 6.45 mm). Since the StellaCam series of CCDs were meant to be integrating/video cameras, the sensor can read out very quickly, at about 0.02 seconds per full chip. Read noise and dark current measurements are not available. Peak response of the chip is around 95% in the visible spectrum for the Sony ICX248AL, but this does not take into account the StellaCam chip housing, which includes a glass window.

The Astrovid camera is legacy equipment; it outputs analog video in NTSC format and was previously used with a small CRT TV set. In order to get it working in a remotely operable sense, the composite video output was routed through a capture

card that would provide a USB connection to the control computer. Signal from the capture card is obtainable using open source VLC software. The Astrovid camera works very well as a simple guide camera (see mounting configuration in Figure 3.17 but is not suitable for capturing and saving images.

Chapter 4

Observatory Control Software

“The good news about computers is that they do what you tell them to do. The bad news is that they do what you tell them to do.”

Ted Nelson,
American Information Technology Pioneer

4.1 Overview

One of the primary tasks for this thesis is the development and implementation of operations software that allows all Investigating Near Space Interaction Regions (IN-SpIRe) observatory systems to be controlled remotely. The user requirements are given in Appendix A. The objective is to control every hardware component from the same software package, keep a log of every available sensor reading, and record the same sensor readings at every onset of data collection. This way, the astronomer will have complete control over the observations and never miss a recording or record data incorrectly. Another major goal of remote operations is to set up an observing script planner, so that the astronomer can set up a night of observing in advance and simply let it run. This will take advantage of the fact that full observatory control will already be available from the same computer.

The INSpIRe siderostat (inherited from Pine Bluff Observatory (PBO)) was previously operated using a LabVIEW interface, so to stay consistent, the INSpIRe software package is also written in LabVIEW. Where preferred, some Python scripts have been written for image processing and plot customization; these scripts are easily called from LabVIEW. Each graphical user interface (GUI), including the INSpIRe Launchpad and all widgets, is developed in LabVIEW.

The hub of remote operations is called the INSpIRe Launchpad. All available hardware control is organized into widgets that are run from the Launchpad. The INSpIRe Launchpad is responsible for recording sensor information to a daily log file and monitoring power outages. Daily reports and emergency alerts are automatically distributed via e-mail from the Launchpad. Generally, each widget is responsible for sending commands to its associated hardware and displaying and recording any available sensor data from the hardware. Some widgets are not associated with any hardware and are meant to be used as a tool for observing.

4.2 A Crashcourse in LabVIEW Terminology

LabVIEW, sometimes referred to here as LV, is a National Instruments software product that is often used in the application of hardware control and monitoring, especially for National Instrument hardware products. LV aims to make it easier for the average programmer to build user interfaces for their systems using modular code blocks. The fundamental building block of any LV code is the virtual instrument (VI). A VI has a block diagram, where the true programming is executed in flowchart style, and a front panel, the window that the user can interact with while the VI is running. Within the block diagram, the programmer has access to hundreds of functions that can be dragged and dropped into place. Wires are used to connect the functions, and execution follows the wire connections from left to right; whereas, in the usual text-based programming language, execution would go from the top line to the bottom line. On the front panel, the programmer can choose from a wide array of controls and indicators to be used to input or output various datatypes: strings, booleans, integers, floats, arrays, and clusters. These datatypes are common among

other programming languages. The LV cluster is akin to the struct datatype in C; clusters are a user-defined set of variables that can be of mixed datatypes.

4.2.1 Event Driven Interfaces (EDI)

In LV, the event driven interface (EDI) structure includes three stages that happen in sequence: the set-up procedure, the main loop, and the clean-up procedure. In more advanced interfaces, the main loop runs in parallel with other loops, which could be useful for continuous monitoring of hardware or certain controls on the front panel. The main loop includes an event structure, which waits for user interaction or other events to trigger corresponding code blocks.

4.2.2 Non-Reentrancy

Most of the INSpIRe software control consists of main VIs (usually EDIs) that call subVIs to accomplish specific tasks. SubVIs are VIs that get called by another VI and are most useful when built as modular code blocks that can be used repeatedly. The only problem with repeatedly calling code blocks, especially from multiple parallel loops, is that they might be called at the same time. LV solves this problem by automatically setting all VIs to be non-reentrant, meaning that the code block cannot be run in one part of the code while it is currently running in another part of the code. This is extremely handy when it comes to accessing configuration files, storing data, and hardware communications, so that commands to memory or the system do not interfere with one another and can be handled one at a time.

4.2.3 Functional Global Variable Clusters (FGVC)

The Launchpad and widgets each communicate data to each other through their functional global variable cluster (FGVC). FGVCs are a type of VI used to get or set data without error by never allowing both actions at the same time, due to non-reentrancy. The structure of an FGVC, see Figure 4.1, takes advantage of a concept called shift registers, which are a type of node that keeps data stored between iterations of a while

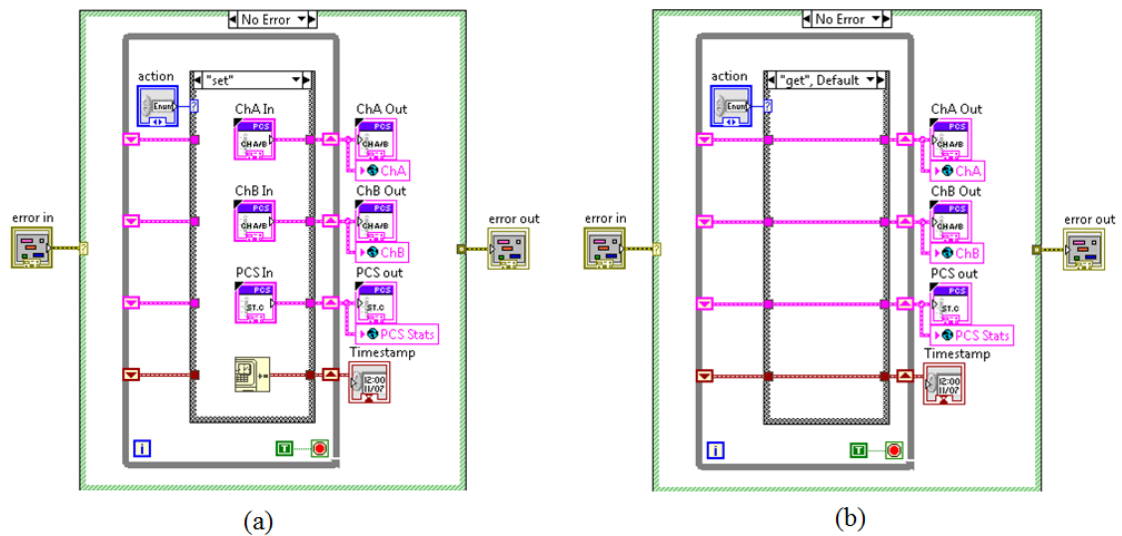


Figure 4.1: This is the functional global variable cluster (FGVC) for the Pressure Control Widget. When ‘set’ is chosen as the action, all of the data available from the Pressure Control System (PCS), along with a timestamp, is stored to the shift register. The next time the FGVC is called to ‘get’ information, the uninitialized shift register will output the last stored value in memory.

or for loop. Shift registers are commonly used in applications that loop through updates to a particular variable, such as counting or appending to an array. However, in an FGVC, the memory location of the shift register is simply used to store or access the variable one time. Because the shift register is uninitialized before the loop is run, the last value stored to the shift register will be used when it comes time to access the memory location.

Each widget in the INSpIRE control software has its own FGVC that is updated at regular intervals whenever the widget is running. The major FGVCs also include a timestamp that is updated whenever the the FGVC was last updated. The Launchpad grabs sensor data from each FGVC at regular intervals to record to the daily log file. Any Detector Widgets, widgets that are responsible for data collection detectors, also grab sensor data from FGVCs during data collection and save it to the science data file header.

4.3 INSpIRe Launchpad

The INSpIRe Launchpad (see Figure 4.2) acts as the principle point of operations for the entire observatory. It accomplishes four major functions: (1) provides access to all subsystem widgets, (2) records all available status feedback from running subsystem widgets at regular intervals, (3) monitors the power supply, and (4) triggers all running subsystems to stow to an appropriate safe state upon exit. At runtime, Launchpad automatically opens the Environmental Sensor System (ESS) and PCS widgets in hidden mode (see further in this section for information on hidden widgets), begins recording status feedback at an interval of two minutes, and begins monitoring the uninterruptible power supply (UPS).

4.3.1 Widget Accessibility

Launchpad includes well-labeled buttons for all of the available widgets and features. Each widget that is accessible from Launchpad can enter one of three states: (1) a stowed state where the widget is not waiting for user interaction or attempting to communicate with any hardware, (2) a running and visible state where the widget is monitoring the feedback from its hardware while waiting for user interaction and the widget's front panel is accessible to the user, or (3) running and hidden, which is similar to the running and visible state except that the front panel is not accessible. Refer to Figure 4.3. The INSpIRe Launchpad keeps track of what state each widget is currently in. When a widget is in the stowed state, its corresponding LED indicator on Launchpad will be turned off; if the widget is running, in visible or hidden state, the LED will be lit up. In Figure 4.2, both the Environment Monitor and the Pressure Control widgets are shown on the Launchpad as running. If a widget is stowed, then clicking on its button on the Launchpad will trigger its running and visible state. If a widget is running and hidden, then clicking on its button will change its state to running and visible without interrupting any actions it might currently be taking. Clicking on a widget's Launchpad button while it is visible will simply bring the widget's front panel to the foreground of the user's monitor space (this may be useful in the event that multiple windows are open on the user's monitor). To put a running

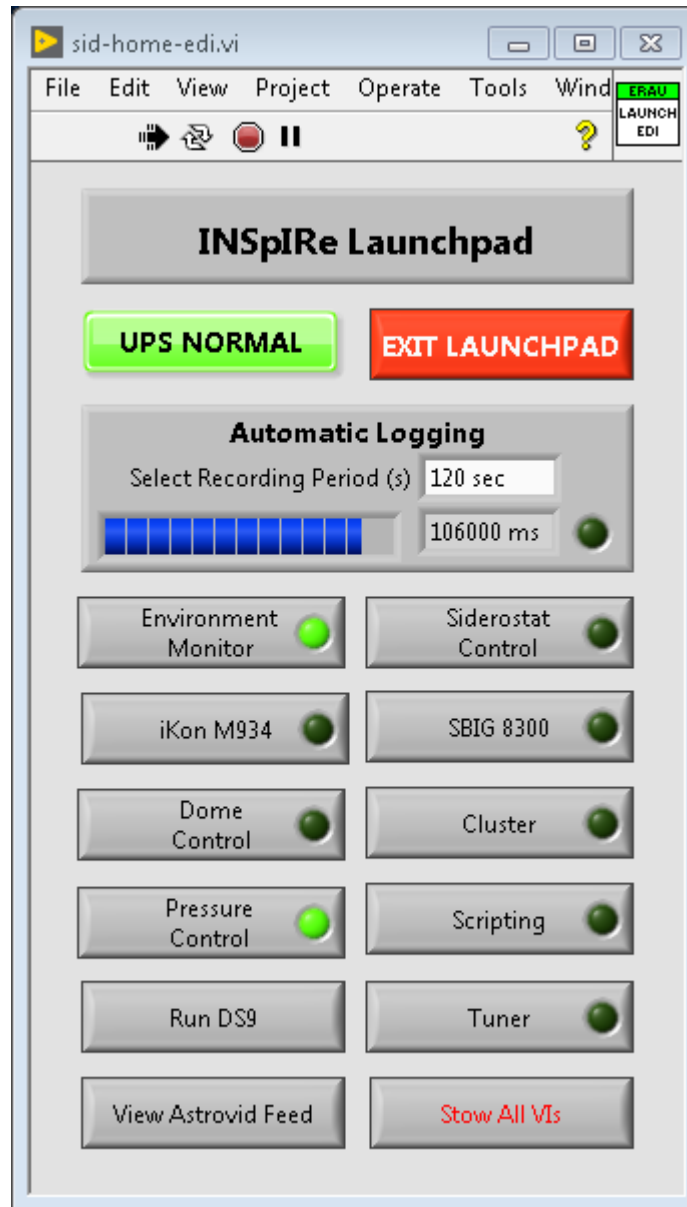


Figure 4.2: The Launchpad is the main widget from which all other widgets can be accessed. The LED indicators on the Environment Monitor and the Pressure Control widgets are lit up, which means those two widgets are currently running.

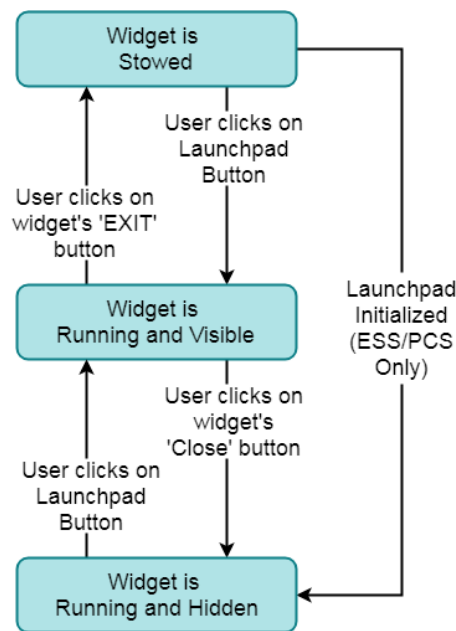


Figure 4.3: Each widget can be in one three states at any given time. This diagram depicts the user actions that change the widget’s state from one to another.

and visible widget into a hidden state, the user only needs to close the window (by pressing the ‘X’ in window’s title bar). Note that this user action does not stow the widget. Each widget features a bright red ‘EXIT’ button that will place a running widget into its stowed state.

4.3.2 Automatic Logging

While Launchpad is waiting for user interaction, it is also working in parallel to record the status of the various hardware components whose widgets are currently running. The default time interval between recordings is two minutes. It is recommended that all widgets that are contributing to the recording update their data readings at a faster rate than the recording function. The front panel of the launchpad displays a timer that counts down to the next recording event. When the countdown reaches zero, all of the available FGVCs are read out and the values are appended to a text file. At each recording event, the date on the computer is checked: if the date corresponds to a log file that has already been created, then the data is appended;

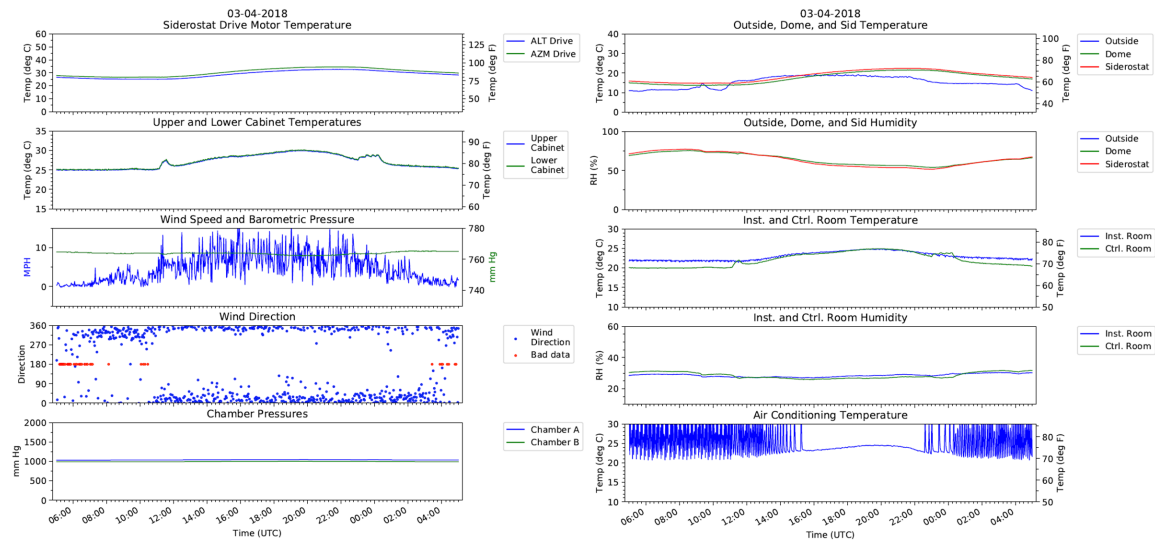


Figure 4.4: The daily summary report from March 4, 2018.

if the date corresponds to an unmade log file, then a new log file is created before appending the data. In this way, a new log file is created every 24 hours and stored to an appropriate year and month folder. This recording mechanism has been in place since June 2016, although the amount of data stored has increased since then as new hardware is integrated. The same event that triggers the creation of a new log file also triggers the circulation of the daily summary report. The daily summary report consists of two pages of 24-hour time plots of various ESS and PCS parameters from the previous 24 hours of recordings, as in Figure 4.4. Once created, the report is sent out via email to a list of recipients, which is kept as a config file on the control computer for easy access. The daily summary is a way of keeping an eye on the status of the INSpIRE observatory outside of operations.

4.3.3 Power Outage Monitoring

Another function of the Launchpad is to monitor the uninterruptible power supply (UPS) that routes power to the control computer. Feedback from the UPS is accessible via serial communications over an RS-232 connection. When Launchpad is initialized, this connection is set-up with the appropriate serial settings and Launchpad starts

to send requests for feedback from the UPS. A request for information about the battery is sent every four seconds. If the battery is on backup, this triggers an event in Launchpad's EDI. Launchpad then requests more information from the UPS about the battery's power level and its estimate of the minutes remaining before the UPS battery gives out. Next, the requested information is sent out to the same list of recipients that receives the daily summary report with a subject line that reads "ALERT: UPS is on Battery". When the power outage is over and the UPS is once again receiving power from the main observatory power line, the same event is triggered. The UPS is once again entreated for information and that information is sent out in an email with the subject "ALERT: UPS is back to normal". Often, the most important information from this alert system is the timestamp that is sent out with the battery information, so that the exact time of power outage onset is known no matter what time the email was received by the recipient (not always the same between recipients).

4.3.4 Observatory Shutdown

Finally, Launchpad is required to be able to run each of the currently running widget's shutdown procedures sequentially. This can be done in one of three ways: the 'EXIT LAUNCHPAD' button will run observatory shutdown and then close the Launchpad; the 'X' button in the titlebar will run observatory shutdown and then close the Launchpad; and the 'Stow All VIs' button will run observatory shutdown and keep the INSpIRE Launchpad running. Each of them triggers a user dialog box so that the shutdown procedures are displayed before they are committed to. The user can look over the procedures and then decide to go ahead with shutdown or cancel shutdown.

4.4 Hardware Control & Monitoring

4.4.1 Environment Monitor Widget

The Environmental Sensor System (ESS) is read out at regular intervals by the Environment Monitor, or ESS, widget. This widget is responsible for updating the FGVC

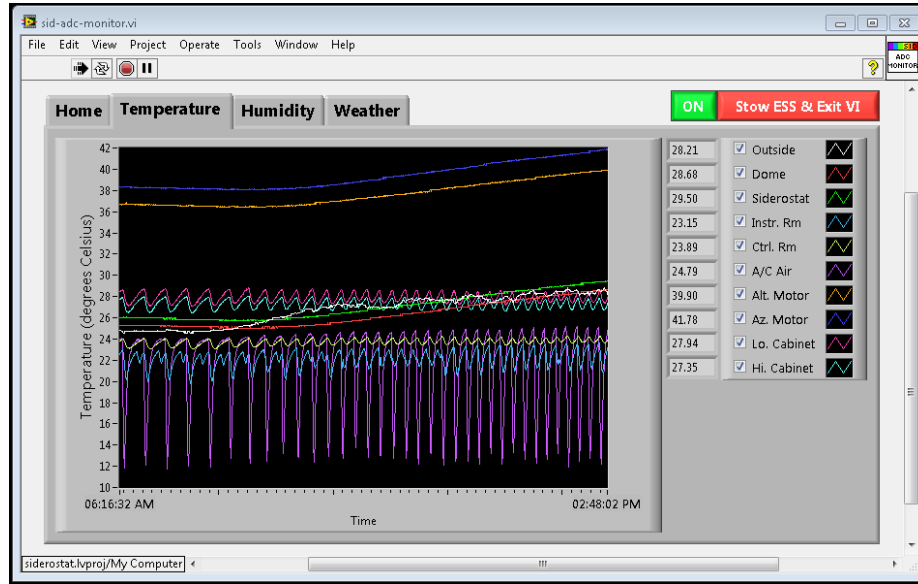


Figure 4.5: The Temperature tab within the ESS widget shows 10 different temperatures over an 8 hour period of readings.

for the ESS. The default update interval is 30 seconds, but the user may safely decrease this time to 3 seconds with the limitation being the time it takes for the analog-to-digital converter (ADC) to be read out for all eight multiplexer channels.

The following readout and conversion scheme was designed and implemented by Jeff Percival at University of Wisconsin (UW-Madison). First, 12-bit analog-to-digital unit (ADU) values are read from the ADC and converted into voltages with a user-defined offset and gain adjustment (calibrated by Percival). The ADU to voltage conversion is given:

$$V = G \left(\frac{V_{\max} - V_{\min}}{2^{12} - 1} (C_{\text{adu}} + C_o) \right) \quad (4.1)$$

where V is the desired voltage reading, G is the gain adjustment, V_{\max} and V_{\min} are the maximum and minimum voltages that can be represented (+10 and -10, respectively, for this system), C_{adu} is the ADC reading in ADUs, and C_o is the ADC zero offset in ADUs (the offset is adjusted to 3 ADUs). After a voltage is obtained for all ADC inputs on each multiplexer channel, the array is converted into engineering units through a linear conversion:

$$x = JV + K \quad (4.2)$$

where x is the value of the reading in engineering units, J is the conversion rate appropriate for the engineering units, and K is the zero offset. The values of J and K have been calculated for each channel and are stored in a configuration file on the control computer. For each read, the configuration file is accessed so that the conversion can be completed.

Percival created the original user interface for this widget. The author's contributions were to modify this user interface so that it is more compact and meets the general requirements for INSpIRe widgets. The first modification was to change the set-up and exit schemes so that Launchpad would be able to see that the widget is running and externally force the widget to shutdown when needed. Another modification was to develop an FGVC for storing ESS data and to build it into the readout mechanism. Additionally, error logging was added to the main loop to catch readout errors from the ADC. Changes were made to the front panel to maximize ESS plot readability while minimizing screen space; tabs are utilized so that plots of temperature, humidity, and other weather statistics are grouped together by unit and displayed in a large, readable format. See Figure 4.5 for a depiction of the 'Temperature' tab. The plot displays the last 1024 readings (equivalent to about 8 hours and 32 minutes if set to readout every 30 seconds) and allows the user to select which channels they'd like to see displayed.

4.4.2 Siderostat Control Widget

The siderostat is used to collect light from specified targets on the sky. In order to move to a target in sky coordinates, the control software has to read in a user-defined target, translate the given sky coordinates to machine coordinates, and then execute the corresponding motions on the altitude and azimuth motors. There are three coordinate systems: (1) right ascension (in hours) and declination (in degrees), which are commonly used by astronomers and are independent of Earth rotation or time of night; (2) absolute altitude and azimuth in degrees from the local horizon and

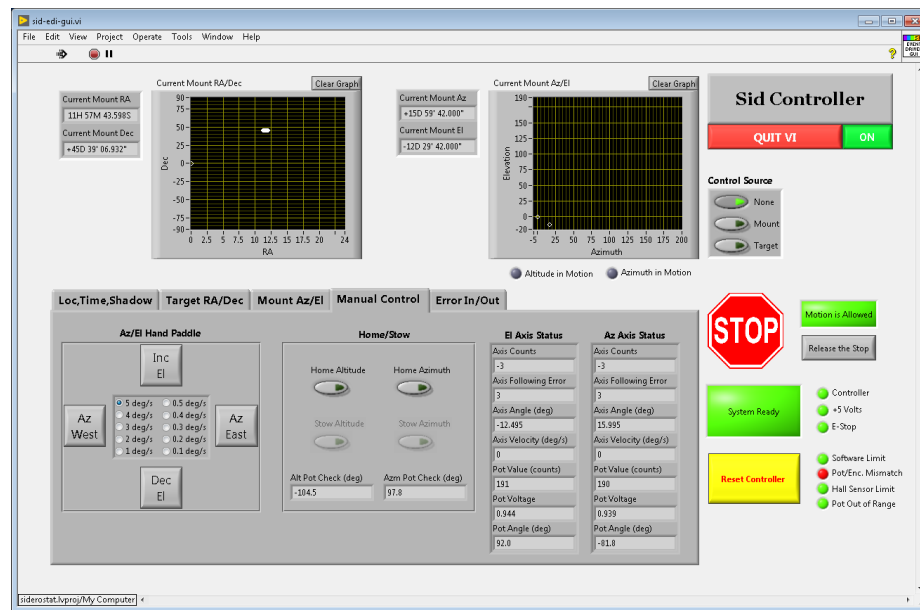


Figure 4.6: The Siderostat Control Widget has three modes of operation and a fancy global inhibitor that stops motion in case of emergencies.

local North; (3) relative altitude and azimuth in steps on the motor.

The siderostat control widget was developed originally by Jeff Percival while the siderostat hardware was being developed at UW-Madison by Kurt Jaehnig. The control widget has two easy-to-read charts of the current coordinates of the siderostat pointing in both right ascension and declination and in azimuth and altitude. There are three modes of control: (1) target tracking in sky coordinates, (2) target tracking in machine coordinates, and (3) manual handpaddle mode. See Figure 4.6 for a view of the manual control tab in the siderostat control widget. Note, Percival also programmed in a global inhibitor, which stops siderostat motion in the case that a hard limit has been reached or in the case that the user would like to stop motion.

An important modification to this widget for use in the INSpIRE observatory was the implementation of a pointing coordinates transformation, also written by Percival, for later data analysis. The transformation, ominously referred to as the Shadow Code, includes astronomically important values for geocoronal research, such as the solar sky coordinates, shadow altitude, and galactic coordinates. Additionally, modifications were made to this widget as necessary to incorporate the information

from the siderostat into the automatic logging and Flexible Image Transport System (FITS) file population mechanisms of the INSpIRE control software.

Percival designed and implemented the coordinate transformations that occur between the various coordinate systems. From right ascension, α , and declination, δ , to altitude, ϵ , and azimuth, ζ is a straightforward but tedious calculation, which first requires conversion from local time to local sidereal time (based upon your local latitude, θ_{lat} , and longitude, θ_{lon} , and an epoch, usually January 1st, 2000 at 12 hours UT) in order to find the Hour Angle, χ , of the object. The HA determines how close to the meridian (the imaginary north-south line above the local horizon) the object is. Once the RA, Dec, and HA are known, then the following formulas are used to calculate altitude and azimuth:

$$\epsilon = \sin(\delta) \sin(\theta_{\text{lat}}) + \cos(\delta) \cos(\theta_{\text{lat}}) \cos(\chi)$$

$$\zeta = \cos^{-1} \left(\frac{\sin(\delta) - \sin(\epsilon) \sin(\theta_{\text{lat}})}{\cos(\epsilon) \cos(\theta_{\text{lat}})} \right)$$

if $\sin(\chi)$ happens to be positive, then the azimuth is first subtracted from 360° . This calculation is executed by Percival's Telescope Pointing Machine (TPM) once per second on the current input to the target right ascension and declination control. The TPM has also been used at other observatories, including the Wisconsin H-Alpha Mapper, the South African Large Telescope, and the WYIN Observatory.

If the siderostat is placed in control mode (i.e. actively tracking a given target), the current input to the right ascension and declination controls on the front panel become the new active target. The converted altitude and azimuth coordinates are transformed into counts on the stepper motor and then a command is given to the motors to move that number of steps. The angle-to-counts conversion is a linear transformation based on the home position coordinates, in both the angular coordinate system and the stepper motor counts coordinate system, and a scalar in units of counts per degree. Each of these values are stored in a configuration file which is accessed as needed. The counts per degree scalar is set by the motors, and the home

position is used as an offset. However, Percival uses this constant offset to “hide a multitude of sins” (as said by Percival in private communication), so the home position isn’t *quite* the home position. It’s also the offset between the siderostat’s orientation and the north celestial pole.

$$C_{AZ} = \frac{1}{K_{AZ}} (\zeta_{TARGET} - (\zeta_{HOME} + \zeta_{NORTH}))$$

$$C_{ALT} = \frac{1}{K_{ALT}} (\epsilon_{TARGET} - \epsilon_{HOME})$$

where C_{ALT} and C_{AZ} are the number of counts from the home position to the target in either axis, and K_{ALT} and K_{AZ} are the scalar number of counts per degree on either axis. The constant offset in the azimuth axis is adjusted by any offset in the north-south alignment of the system, but this is not an issue in the altitude axis. No matter the position of the siderostat, $\zeta_{HOME} = 9^\circ$, but at ERAU, $\zeta_{NORTH} = 17^\circ$, so the total offset in azimuth is 26° . (This also affects the azimuth stow position. In a normal orientation, the stow position would be -90° azimuth, but with the ζ_{NORTH} offset, it becomes -73° at ERAU. This is also stored in a configuration file.)

Meanwhile, two potentiometers are tracking the movements of each axis’s stepper motor. The potentiometer readings are used in tandem with the home and stow limit switch readings to determine whether the motors are in bounds or out of bounds. Another simple linear equation dictates the conversion from volts directly to degrees with a catchall constant offset:

$$\zeta_{TARGET} = P_{AZ} V_{AZ} - (P_{AZ} + 90^\circ - \zeta_{NORTH})$$

$$\epsilon_{TARGET} = P_{ALT} V_{ALT} + (90^\circ - P_{ALT})$$

where P_{ALT} and P_{AZ} are the scalar for degrees per volt for each axis and V_i is the voltage reading from each potentiometer. The constant offset is a combination of the

degrees per volt scalar, a constant 90° offset due to the geometry of the siderostat, and the north-south alignment in the case of azimuth only. The offset for potentiometer readings at ERAU turns out to be -217° . This is stored to a configuration file.

Percival's code covers many coordinate systems and includes a series of transformations to convert between them. The only caution is that each of these linear transformations has to be updated when the observatory is deployed to a new site. The good news is that a small offset in the north-south alignment of the siderostat will not break the system, since it can be fixed in software.

4.4.3 Dome Control Widget

The major responsibilities of the dome widget, shown in Figure 4.7, are to report the current status of the dome and allow the user to open and close the dome. At runtime, the dome widget initializes the serial connection with the dome and begins reporting its status. When the widget is stowed, a user dialog box will inform the user that the dome will not be automatically closed upon stowing and that the user should place the dome in a safe place before stowing the widget.

When powered on and not in use (idle mode), the dome will output a continuous stream of feedback characters to inform the recipient of the state of each half of the dome (see Table 3.3). The dome widget listens for and translates the dome's feedback into a cartoon depiction of the dome, as seen in Figure 4.7. This status is also saved to the dome's FGVC. There are four states that the dome can report, and a fifth state that represents the absence of data (lost or absent connection). The five states are shown in Figure 4.8. The only hard feedback from the dome is whether or not the shutter has hit a limit switch; in other words, there is no way to tell how much the shutter is open if it is in between fully closed and fully open. Anytime that the dome widget sends commands to the dome, the appropriate 'East/West is Moving' LED indicator lights up to show that the dome is currently being commanded to move and the status caption changes to either 'Opening...' or 'Closing...' instead of the usual status caption.

The user has access to four options for moving the dome via the dome widget. One

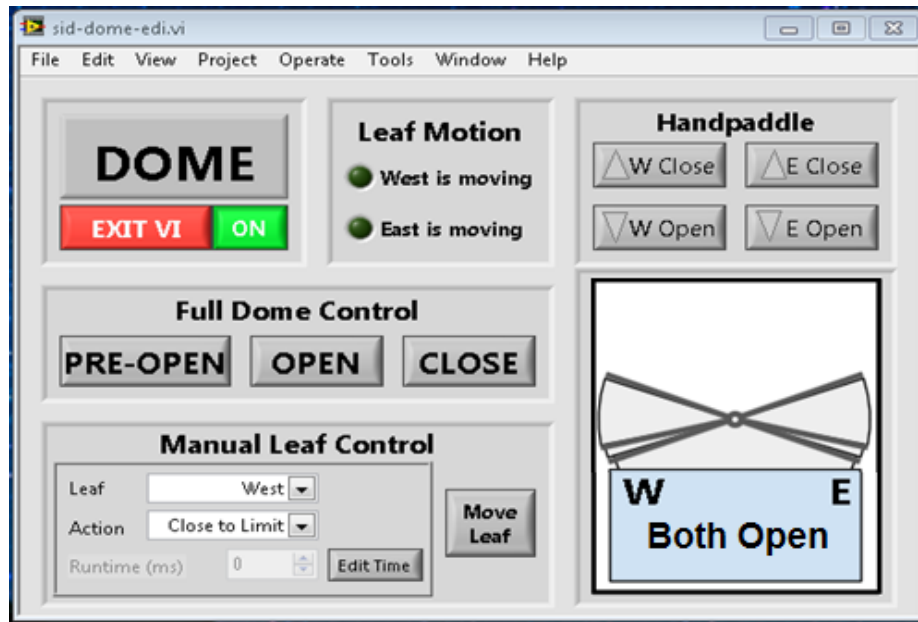


Figure 4.7: The dome widget displays feedback from the dome and allows the user to move the dome shutters using several different methods.

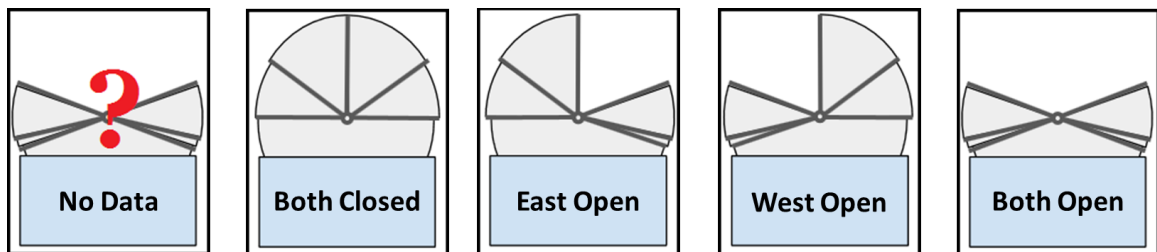


Figure 4.8: The dome widget uses a cartoon and a caption to display an easy-to-glance-at depiction of the dome's current status. The above five cartoons are the five states available.

of these is to fully open or close both halves of the dome. It has been shown through testing that the order in which the shutter are opened or closed does not matter, but because they have to opened or closed in sequence rather than in parallel, the West half was chosen to go first. The user also has the option to open or close one half at a time by using the ‘Manual Leaf Control’ box. Within the manual control, the user selects the West or East leaf and then chooses to open or close to a limit or partially. If the user chooses to open or close the leaf partially, they must input a time in milliseconds for the leaf to move. In partial open or close mode, the dome widget sends the appropriate movement command for the time duration selected. The last option is to use the ‘Handpaddle’, where the user can click and hold on the desired movement button; the dome widget will send the appropriate movement command until the user lets go of the handpaddle button.

All commands and monitoring over serial communications is accomplished via one non-reentrant VI. This prevents the widget from attempting to write to or read from the serial port in two places at once, and allows parallel control and monitoring loops within the main widget.

One last feature available via the dome widget is the ‘Pre-Open’ function. If the user presses the ‘Pre-Open’ button, the dome will move its West leaf by one step, or about three inches, open. The pre-open function is the equivalent of sending one movement command. This function is required because testing has shown that the rubber edging at the top of the outer leaves is capable of sticking to the opposite leaf. Because the dome opens by releasing tension in the belts and allowing gravity to do the work, if the edges stick together and enough tension is released in the belts before they become unstuck, the shutters may go into free-fall instead of lowering gracefully. The idea of the pre-open function is to release just enough tension from the belts so that the shutter will free-fall for only a few inches rather than a few feet in the case that the edges are stuck.

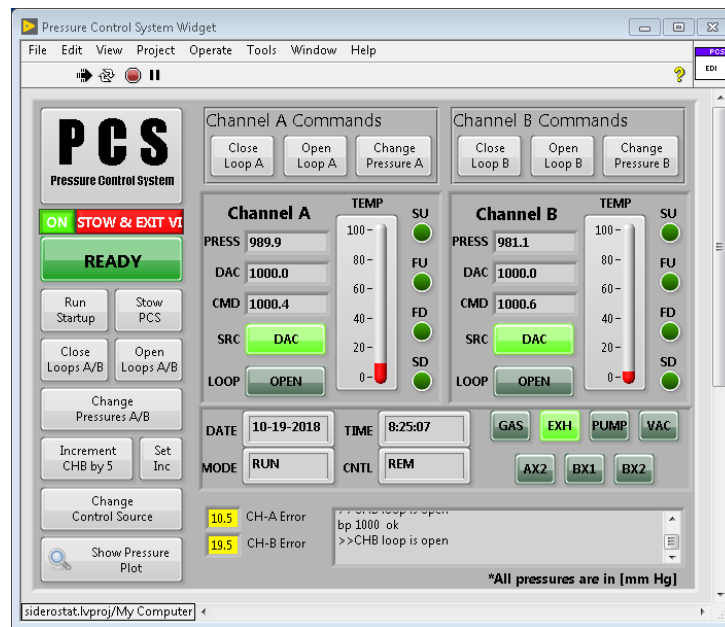


Figure 4.9: The Pressure Control Widget includes a display of Chamber A and B’s current status and plenty of buttons to help the user control the pressure chambers.

4.4.4 Pressure Control Widget

The pressure control widget allows the user to interact with and get feedback from the PCS, which is connected via gas lines to the Fabry-Perot interferometer (FPI). The pressure control widget (see Figure 4.9) is tasked with (1) reading out and displaying the current status of the Pressure Control System (PCS), including the pressure, temperature, and loop and control modes of each pressure chamber and the overall status of the system, and (2) changing the target pressure and modes of operation in each chamber. The PCS widget is started up in a running and hidden state when the Launchpad is first initialized. This is because the PCS, even when in open loops mode, is important to monitor in case of gas leaks in the physical pressure chambers or gas lines. When the PCS widget is first run, the serial connection is initialized, and the widget begins requesting status reports from the PCS on a continuous basis. When stowing, the PCS widget commands the pressure to a neutral value, 1000 torr, and opens the loops.

At the top of the left controls column, there’s a status boolean that proclaims

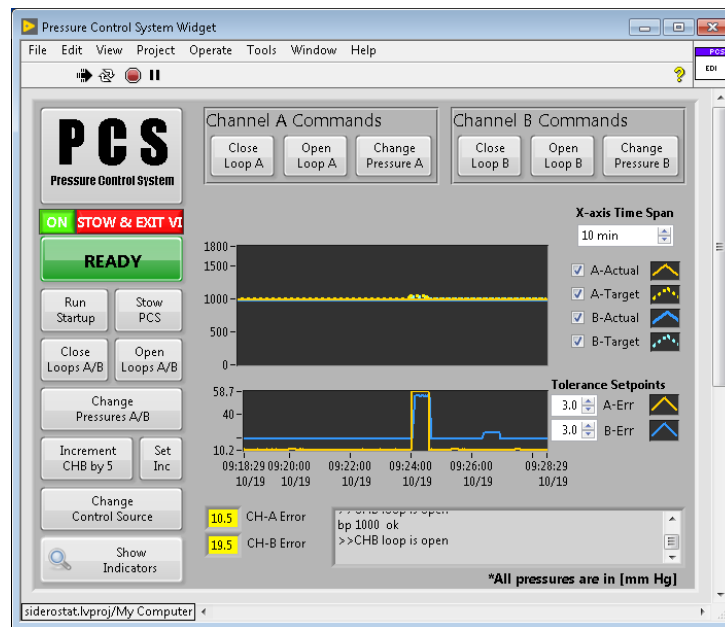


Figure 4.10: The Pressure Control Widget also has a plots view, so that the pressure in the chambers can be monitored over time, as well.

‘READY’ when the PCS is in a safe state for receiving commands and ‘WAITING’ when it is currently processing a command. The center of the front panel is actually a hidden tab that the user can flip between indicators, for a snapshot view like in Figure 4.9, or pressure plots, for a historical view of the pressure like in Figure 4.10, by pressing the ‘Show Pressure Plot/Indicators’ button. In the indicators view, the most recent status report is displayed in graphical form, with labeled LED indicators for boolean outputs and number or string indicators for analog outputs. In the plots view, the current pressures, target pressures, and error between the two are plotted over a user-defined time interval, which defaults to 10 minutes. At the bottom of the PCS widget there’s a response feed that displays the serial response from the PCS. Responses to commands consist of an echo of the command and the word ‘ok’ to let the user know that the command was received. The PCS widget also disallows certain actions under certain conditions, and in these cases, the response feed will display a message that explains the issue. For example, if the user attempts to change the pressure when the loops are not open, then a warning will be displayed

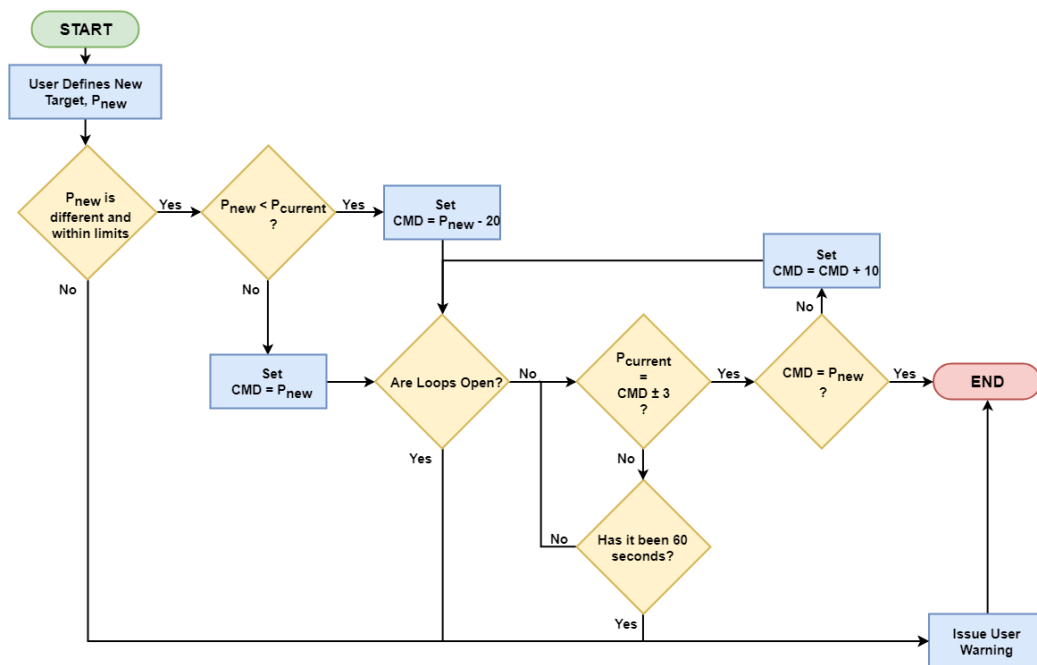


Figure 4.11: When the user chooses to change the target pressure, several checks and a feedback loop have to happen before the pressure change is successful.

in the response feed. Finally, the two numeric indicators (highlighted in yellow in Figures 4.9 and 4.10) to the left of the response feed indicate the error between the commanded pressure and the measured pressure. When the error values are above a user-defined threshold (defaults to 3 torr), the box will turn yellow to warn the user that the target pressure is not being maintained.

The main controls available to the user consist of closing and opening the loops on either or both channels, changing the pressure on either or both channels, or changing the control mode (e.g. from ‘DAC’ to ‘POT’) for both channels. In the case where two chambers’ settings are changed at one time, chamber A is dealt with before chamber B and are therefore not run in parallel. For a flowchart of the pressure change process, see Figure 4.11. When a new target pressure is defined by the user, the PCS widget immediately checks to see if the new target pressure is different from old target and if it is inside the soft limits ($50 \text{ torr} \leq P < 1800 \text{ torr}$); if it is not, the new target is thrown out and a warning is issued to the response feed. The desired final pressure value should always be approached from the same direction,

so the next check determines whether the new target is higher or lower than the current pressure. If the new target is higher, the PCS widget commands the new target pressure. If the new target is lower, the PCS commands a value that is 20 torr below the user-defined target, then 10 torr below, and then the actual target. Once any value is commanded, whether it's directly the new target value or a series of new target values, the PCS widget enters a feedback loop that exits under three conditions: (1) if the loops are open at the time of command, the feedback loop is exited and the user is issued a warning; (2) if the measured pressure matches the target pressure within the user-defined threshold (usually 3 torr), the loop is exited without any warnings; (3) if 60 seconds pass before either of the first conditions are met, then the loop is exited and a timeout warning is issued. If the new target value requires a series of increasing commands to be achieved but the first of the series does not achieve pressure successfully, then the series is canceled. Note that this scheme allows the target pressure to be set even in open loop mode, which is useful in the case that the user would like to place the target at a neutral value before enabling pressure control.

Additionally, two special functions exist that were built in for convenience. It is sometimes necessary to run a specific set of commands to initialize the PCS electronics rack (refer to Table 3.5, and so a 'Run Startup' button allows the user to run these commands automatically and in the correct sequence. The other special function is the 'Increment CHA/B by x' button, which is customizable using the 'Set Inc' button. The increment button allows the user to step through multiple pressures given a known increment, which may be useful in the case that the user would like to do a manual pressure tune. The default setting for this is to increment channel B by 5 torr.

4.5 Detector Control

Each charge-coupled device (CCD) has its own control interface. Both the Andor iKon-M934 and the SBIG STF-8300M have their own control widgets. Andor and SBIG have different drivers for controlling their cameras and go about taking and

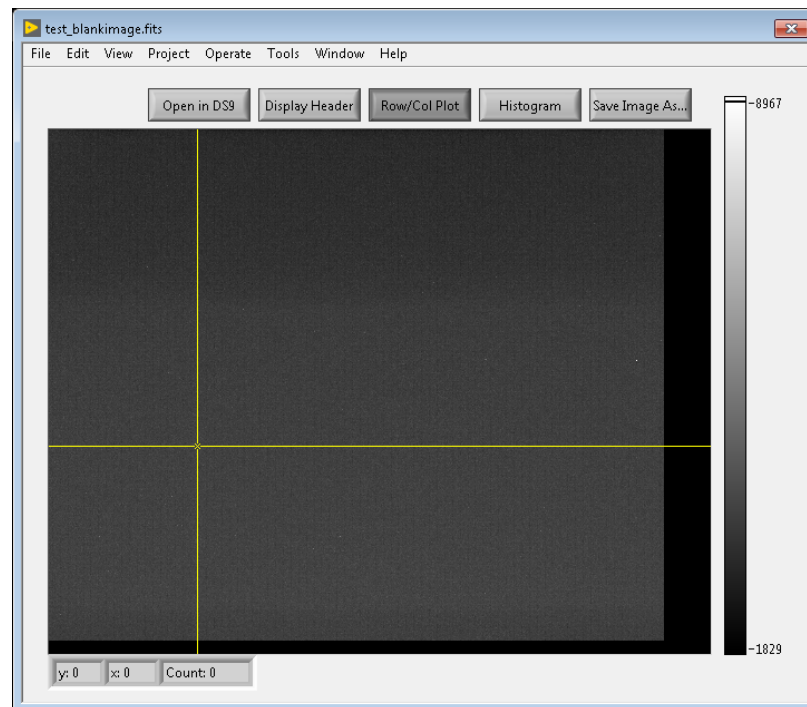


Figure 4.12: The image display VI is used no matter the detector. It includes functions for saving the image, changing the display histogram, displaying row and column cuts, displaying the header, and opening the image in a more formal FITS file viewer called DS9.

reading out exposures in different ways. However, the two widgets share several VIs having to do with displaying and saving the output image. The Astrovid Stellacam-EX is a different story; the only way to change the exposure settings on the Stellacam is to use its physical interface.

4.5.1 Image Display

Both detectors output exposures as 2-d arrays of unsigned 16-bit integers. This makes it very easy to re-use the same widget for displaying the image in both widgets. Whenever an exposure is taken, the image display VI (see Figure 4.12) appears with the new image displayed. To handle multiple images being displayed simultaneously, the image display VI is set to create a clone each time it is called. These clones do not share information and are completely independent from one another.

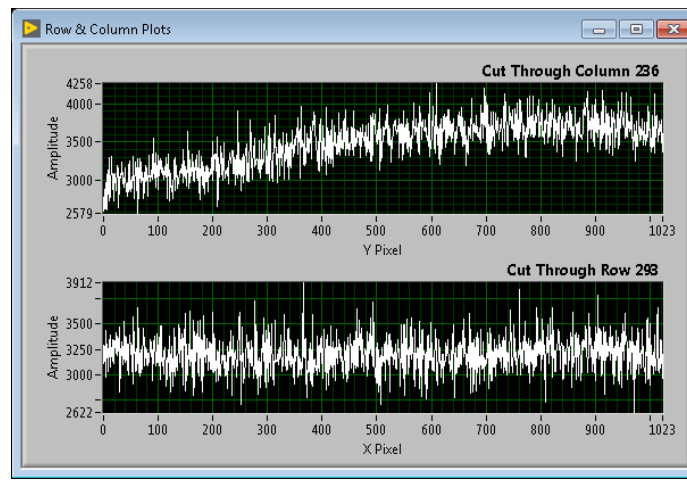


Figure 4.13: From the image display widget, the user can place a row/column crosshairs on an image to see a row and column cut plot.

Each camera outputs a different size image in pixels, so the aspect ratio is adjusted depending on which camera is being used. On the right side of the image, the colorbar is displayed. The colorbar is auto-scaled so that the best range of pixel values is displayed; however, the user can use the ‘Histogram’ button to adjust the visible pixel values. Sometimes this feature helps in seeing very faint image features or toning down a somewhat saturated image when assessing data quality by eye. The user can also use the ‘Row/Col Plot’ feature to assess data quality. When the ‘Row/Col Plot’ button is depressed, a crosshairs appears on the image, as seen in Figure 4.12, that can be moved around using the cursor. When the user has placed the crosshairs as desired, a row plot and column plot will appear in a new window, as in Figure 4.13. To update the row and column plot, the user only has to move the crosshairs to a new location. This functionality is useful in quickly assessing the background level of a fringe image.

If the image has been saved, either automatically or by using the ‘Save As...’ button available on the image display widget, then the titlebar will display the name of the image file and two of the buttons become available for use. The ‘Display Header’ button will open up the FITS file metadata and display it, as in Figure 4.14. The other button is labeled ‘Open in DS9’; this button will open the saved image

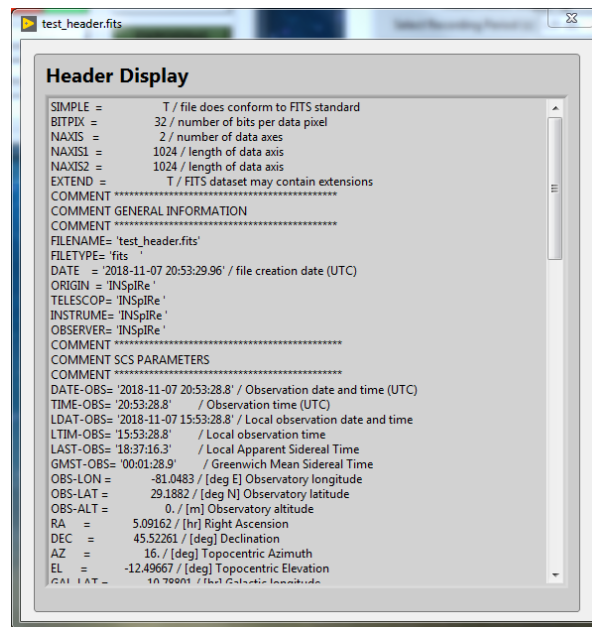


Figure 4.14: If the image has been saved, then the user may choose to display the image header from the image display widget.

in a commonly-used FITS file viewer. DS9 is a free software distributed by the Smithsonian Astrophysical Observatory in Cambridge, MA. It includes many useful image analysis functions. Beyond row and column cuts, the types of analysis available in DS9 are not generally needed for FPI observations, but it's familiar interface is unbeatable for many astronomers.

4.5.2 Autosave

The autosave functionality is useful for automated data collection and to ensure that data is saved. Autosave works in the same way for both the Andor and SBIG detectors, although there are separate FGVCs that keep track on the autosave settings for each detector. In both cases, opening the autosave settings reveals a dialog that looks like Figure 4.15. The dialog includes a file path control and a string control that allows the user to choose the directory to save files to and the prefix of the file. All images that are saved using this feature are stored as FITS files and include a timestamp after the file prefix.

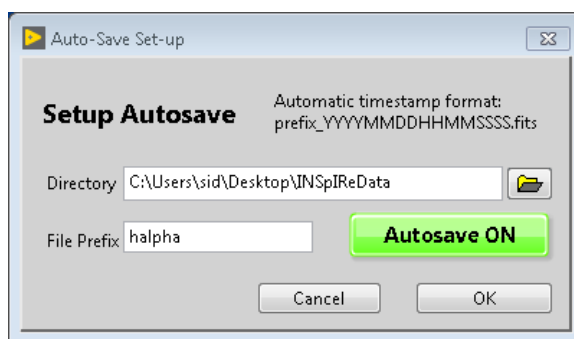


Figure 4.15: The autosave dialog is shared between the Andor and SBIG detectors.

4.5.3 Data Header Population

A Flexible Image Transport System (FITS) file consists of at least two data units: the image data and the header (or metadata). FITS files can contain more data units than these two, including multiple image data units, multiple headers, and another type of data unit called a binary table. The FITS file format is common among astronomers, and oftentimes, they will take an image and then save their data reductions as extra image extensions to the same file. NASA maintains a directory of FITS file handling libraries, one of which is a LabVIEW library called ‘gfitsio’.

The image data unit stores the image data array. The header stores information about the image; the only information that is required to be in the header are the dimensions of the image in pixels and the bit depth of each pixel. However, it is often advantageous to store as much information as possible about the conditions of the observation in the header, as it may help with data analysis later on. Everything from the pointing and timing of the observation to the temperature in the observing room and the temperature of the CCD could potentially be a useful parameter later down the road.

The timing of header data collection is important. A given exposure can be 10 seconds to 10 minutes long. Pointing information collected at the beginning of a 10 minute period might not be as relevant for the end of the 10 minute exposure. However, the latitude and longitude of the observatory isn’t going to change within that 10 minute period. Most of the header information is most useful at the halfway point of the exposure (e.g. for a 10 minute exposure, that would be 5 minutes in). At

the halfway point, information from the detector, PCS, ESS, and Siderostat Control System (SCS) are all readout and stored in corresponding header-formatted FGVCs. These FGVCs differ from the FGVCs that are used for automatic logging because the clusters are specifically formatted for writing to a header and they form a safe space for the information. While the logging FGVCs are re-written at regular intervals, the header FGVCs are only re-written at the halfway point of each exposure.

The header information collected during the exposure needs to be temporarily stored in memory so that the data is not overwritten by the next exposure event before the first exposure can be saved. With autosave turned on, this is not an issue, but if the user takes any exposure without autosave, the header data still needs to be available for when the user decides to save the image or if the user wants to save the image as a different name from the image display widget. To solve this issue, the image display widget that opens after every exposure keeps a copy of the header associated with that image that can be accessed when the user chooses to ‘Save As...’ from the front panel.

The same scheme is used for both the Andor and SBIG cameras. Writing the header is exactly the same process for both detectors, as they share the same image-saving VI. First, the image is saved to a FITS file with the basic header. Next, the header FGVCs are read out sequentially and combined with information from a configuration file that includes the keyword, datatype, unit, subsystem origin, and description associated with each row of information. The datatype of each row is used to create an appropriate row-type: booleans will be printed as True or False; floats will be printed as numbers; strings are printed with single quotation marks. The keyword, unit, and description are provide context for the person who has to interpret the metadata later on.

4.5.4 Andor iKon-M934 Widget

The Andor detector widget is very simplistic on the user frontend, but is capable of handling a wide variety and combination of exposure settings. At runtime, the widget initializes its connection with the Andor iKon-M934. Before the user can start taking

images, the exposure settings must be set-up, and so the widget is initialized with the ‘Take Exposure’ button grayed out. Once the exposure settings have been selected, the user is allowed to take an exposure. When stowing this widget, the widget will turn cooling off before disconnecting from the camera.

On the front panel of the Andor camera control widget, there are several status indicators that warrant the user’s attention (see Figure 4.16). The first is a ‘READY/BUSY’ indicator that changes status from ‘READY’ to ‘BUSY’ when the camera is in use and then back again when the camera is idle. There are two indicators, labeled ‘EXPOSING’ and ‘ACQUIRING’, that will light up when the camera is doing the respective action. While the camera is exposing (i.e. collecting photons), a string indicator informs the user of how long the the camera has been exposing for and how long the exposure was set to be. When this is finished, the ‘ACQUIRING’ phase begins, which signals to the user that the image sensor is now reading out the voltages accumulated during exposure. Depending on the readout speed selected in the exposure settings, the acquisition, or readout, phase can take a significant amount of time (up to 20 seconds), and so this indicator eases the mind of the user while waiting for the image to display. Finally, the Andor iKon-M934 has an electronic cooling feature, and so the temperature of the camera is displayed at the bottom edge of the widget, along with an indicator that shows whether cooling is on or off.

Using the widget to take exposures is quite simple. The user simply selects the desired exposure settings from the ‘Exposure Settings’ dialog, as seen in Figure 4.17. The three modes of operation (Single, Series, or Video) are selectable, as well as settings for timing, readout, and image size. If the user selects ‘Series’, then a new control appears to type in the number of images to take. The Image Type option represents all of the types of astronomical images you might want to take: object, dark, flat, bias, and calibration. For the dark and bias frame types, the shutter remains closed. The other three options are simply a label that will automatically be applied to the FITS header. In series mode, the user can select a delay time in between exposures if desired. The readout options correspond to faster or slower readout times, and applying different pre-amp gains can change the contrast of the image. The baseline clamp option places the background noise level of the image



Figure 4.16: The Andor camera control widget is very minimal. The user can change the exposure settings, turn on cooling or autosave, and take exposures. In this image, the widget is currently monitoring an exposure.

to a specific 300 counts. This level varies from image to image and pixel to pixel, but remains mostly stable when turned on. The image size options allow the user to bin data, which means the user can choose to read out pixels that are actually made up of 2 x 2 pixels or 4 x 4 pixels. Binning increases signal per binned pixel and decreases read noise, but also decreases spatial resolution. Lastly, the user may choose to readout only a subframe of the image by selecting the pixel positions of corners of the subframe.

Selecting the ‘Take Exposure’ button will immediately start the exposure(s) that were set-up in the ‘Exposure Settings’ dialog. When exposures are done, the image display widget (see Section 4.5.1) will appear with the most current image. If the user would like to cancel an exposure, they may do so by pressing the ‘ABORT’ button that appears beneath the exposure indicators. This will cancel the exposure and readout of the image sensor, so no image will be available for display.

The last two buttons are the autosave button and the temperature control button. The autosave button will take the user to the autosave dialog discussed in Section 4.5.2. The temperature control button also acts as an indicator; if the user presses the

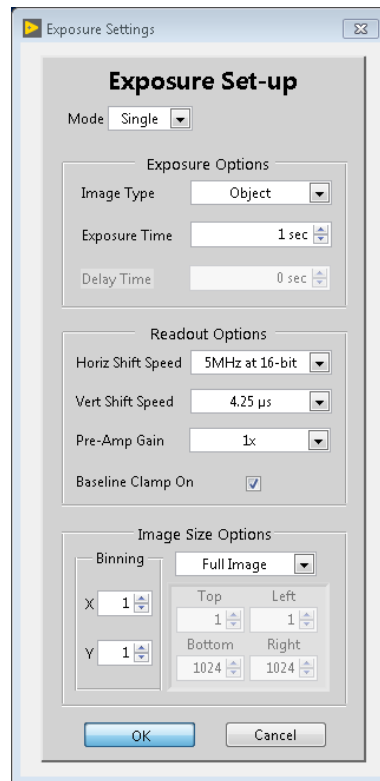


Figure 4.17: All of the parameters for taking images are available in the Exposure Setting dialog box. The user can select the mode of operation, timing, and how to bin and read out pixels.

‘ON/OFF’ button next to the temperature indicator, then the temperature control dialog will appear and the user can select what temperature to set the cooler to.

4.5.5 SBIG STF-8300M Widget

The SBIG camera control widget opens a connection with the STF-8300M detector upon startup. If the connection is not available, the widget will notify the user with a warning dialog box and then stow the widget. If the connection is successful, then the widget will be ready to send further commands. If the user chooses to stow the widget, any cooling that is currently active will be turned off and the connection with the detector is released.

Feedback from the camera is shown along the bottom edge of the widget, as shown in Figure 4.18. While the camera is exposing, the ‘READY’ indicator will change to ‘BUSY’ and the loading bar will begin to move across the screen at a rate corresponding to the exposure time. Once the exposure is done and the camera is reading out, the loading bar will start over and display that the chip is being read. The temperature and filter wheel status are also displayed. Temperature statistics are displayed as the current measured temperature, setpoint temperature, and a measure of how much work the cooler is doing to match the setpoint temperature. The power percentage will be close to 100% while it attempts to coarsely adjust to the setpoint, but once within a certain threshold determined by the camera, the power will decrease. If ambient temperature within the observing environment is much higher than the setpoint, cooling may be more difficult and the fine adjust power will be high. If this is the case, the cooler may cause extra dark current at the chip. Therefore, the power on the cooler is something that the user should be able to monitor. The filter wheel status shows whether or not the filter wheel is currently moving and what filter it is on. The filter wheel monitor uses a configuration file that determines what position in the filter wheel is filled with what type of filter.

To take images, the user has four options available: (1) grab a single frame, (2) grab a series of frames, (3) grab a continuous stream of frames in focus mode, and (4) grab a continuous stream of frames and save every n^{th} frame in finder mode. For

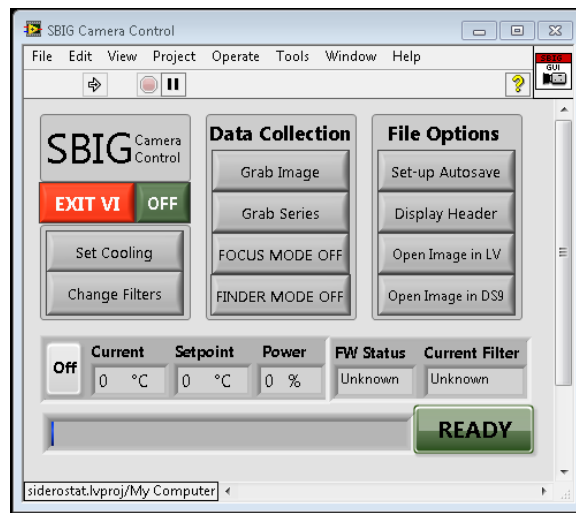


Figure 4.18: The SBIG camera control widget is compact and includes many features for taking different types of exposures, displaying images, and changing the camera settings.

the SBIG widget, each of the four options has their own exposure settings dialog, available under the ‘Data Collection’ buttons. Figure 4.19 depicts the ‘Grab Image’ dialog. The only difference between this dialog and the ‘Grab Series’ dialog is a control for the number of images to take. The user can select the exposure time, image type, and image size just as in the Andor camera control widget. Additionally, the binning option for the SBIG detector is instead called ‘Readout Mode’, where high resolution corresponds to 1x1 binning and low resolution corresponds to 2x2 binning. Two other features are built in to the dialog – the user may choose to have the image open in the LV image display widget or in DS9, and the user may set up autosave from within the exposure dialog box.

Other features of the SBIG camera control widget include setting the temperature cooling setpoint, changing the filter, and several option dealing with displaying and saving images. The available buttons under ‘File Options’ allow the user to set up autosave via the shared autosave feature, display the header of a saved image, display a saved image in the LV image display widget, or display a saved image in DS9.

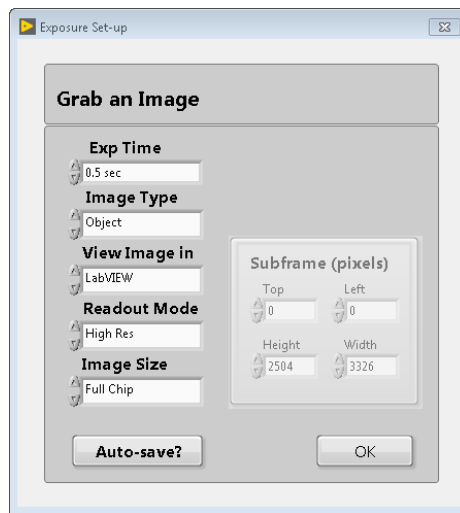


Figure 4.19: The parameters available for taking a single image with the SBIG detector include exposure time, image type, binning, and image size.

4.5.6 Astrovid Feed

The ‘View Astrovid Feed’ button on Launchpad (see Figure 4.2) opens a VLC media player window with very specific settings via the VLC command line options. VLC is a free software that is openly available online and offers many options for media viewing. There is no stowing the Astrovid, because the feed viewer passes control of the video feed to VLC. To close the connection, the user simply closes the VLC window. During observatory shutdown, the VLC window remains open.

The command line options tell VLC to look for the video capture device that converts analog video to a digital output and specifies the video parameters, modeling NTSC video, such as the frames per second (29.97 fps) and dimensions of the frame in pixels (720 x 480). The video codec used was mp2v, which is commonly used for DVDs. The VLC window is set to stream the video output and therefore does not save images. Saving images is not necessary for the use case of this detector, however, since it would only be used to visually confirm the pointing of the siderostat.

4.6 Observing Tools

Several tools have been deemed necessary to add to the control interface for the convenience of the observer. Two of these tools are in the original requirements, the cluster and scripting widgets, and the automatic tuning widget was added after the author determined that the tuning process was unnecessarily operator heavy. The following observing tools take advantage of the fact that all of the previously discussed widgets are built up from modular code blocks; this makes it very easy to grab functions from the other widgets and re-use them in automation and scripting.

4.6.1 Cluster Widget

The goal of the cluster widget is to give the user access to all of the current data from each subsystem without having to open the window for each system individually. Figure 4.20 shows the SCS tab of the cluster widget. This tab includes status updates on the current position of the siderostat and the shadow code output from the siderostat widget. The timestamp in the upper right corner of the tab shows the time and date of the most recent update from the SCS widget. If the timestamp becomes more than 60 seconds old, then the border around the timestamp display turns red. Each of the main widgets has a separate tab with with its own display of data and timestamp. A convenience feature that was built in is the ability to switch between tabs in the cluster using the left and right arrow keys on a keyboard.

4.6.2 Scripting Widget

The scripting widget, seen in Figure 4.21, allows the user to create and run scripts that have been pieced together by the user from a set of available commands. There are currently command sets for the dome, PCS, SBIG detector and Andor detector that each cover all of the available functionality that would be useful in scripting. For example, the detectors are both capable of capturing images in a continuous mode, but that mode would not be useful as a scripting function because it would run indefinitely. The scripting widget has two tab views: the ‘Script’ tab shows all



Figure 4.20: The cluster widget allows the user to check on all of the running subsystems from one place.

of the queued up actions in a scrollable list, and the ‘Add New Action...’ tab can be clicked through to find all of the scriptable actions and add them to the script.

Each action that has been determined scriptable is assigned a unique identifier (e.g. the action that opens the dome is assigned to “dome_open”) and necessary parameters (e.g. which half of the dome to open). The unique identifier and parameters are used to save scripts to a text file that can later be loaded back into the scripting widget and interpreted as a series of actions. The identifier for each action has a defined set of input parameters of specified data types. A configuration file that keeps a record of the available command identifiers and their corresponding inputs is kept on the control computer. Table 4.1 lists all of the unique actions and their input parameters.

As actions are added to the script, they are assigned a sequence number and status. The sequence number determines the order in which the actions are taken. The status is ‘Idle’ until the script is run. Once the script is running, the first action in the sequence enters ‘Running’ mode and displays a yellow indicator, as shown in Figure 4.21. When the action is complete, the indicator turns green and the action is considered ‘Completed’. This is repeated for each action in the sequence. If any action experiences an error, the script produces an error dialog and a red indicator

Table 4.1: Scripting Actions

Action ID	Inputs
sbig_init	
sbig_autosave	path=%[^\,], prefix=%[^\,]
sbig_expose	frame=%d, series=%d, exptime=%.2f, delay=%.2f, bin=%d, top=%d, left=%d, h=%d, w=%d
sbig_cooling	on=%d, setpoint=%.2f
sbig_gotofilter	filter=%d
sbig_exit	
dome_init	
dome_open	leaf=%d
dome_close	leaf=%d
dome_exit	
pcs_init	runstartup=%d
pcs_press	ch=%d, pressure=%.1f
pcs_loops	ch=%d, loops=%d
pcs_src	ch=%d, src=%d
pcs_exit	
ikonm_init	
ikonm_autosave	path=%[^\,], prefix=%[^\,]
ikonm_expose	series=%d, frame=%d, exptime=%.2f, delay=%.2f, hrr=%d, vss=%d, gain=%d, blcon=%d, xbin=%d, ybin=%d, top=%d, left=%d, h=%d, w=%d
ikonm_cooling	on=%d, setpoint=%.2f
ikonm_exit	
misc_delay	time=%.2f

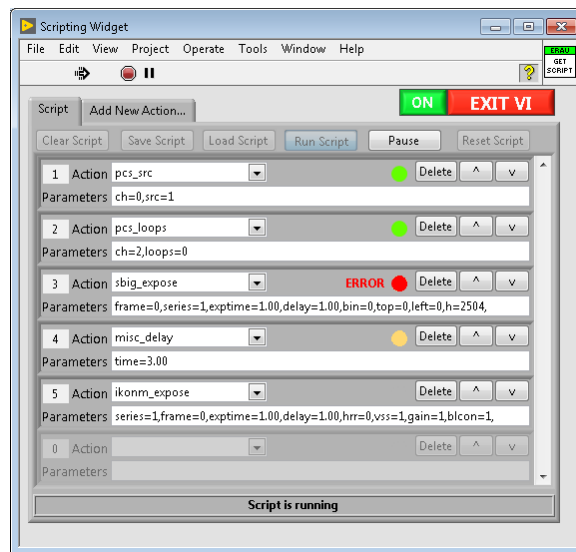


Figure 4.21: Scripts can be created, saved, loaded, run, paused, and edited using the scripting widget. When running, a green indicator means the action is completed, yellow means the action is in progress, and red means the action generated an error!

appears with the label 'ERROR'. The script will pause until the user interacts with the dialog box.

Before the script is run, and while the script is paused, all of the actions that have not yet been started are available to edit. These 'idle' actions can be deleted or moved up and down in the sequence of actions. There are some cases where moving the action up or down is not possible, such as when the action is all the way at the top or bottom of the script; in this case, the action stays put. In the case where the user has paused the script after running some commands, actions cannot be moved into the part of the script that has already been run. Also, while paused, the user may add actions to the remaining un-run part of the script.

When a script has been fully completed, the user may want to re-run the script. The 'Reset Script' button will reset all of the action indicators and allow the script to be run from the beginning again. The script can also be reset while paused. The user can also clear all of the actions in the queue with the 'Clear Script' button to start making a new script from scratch, or the user can load a saved script into the queue using the 'Load Script' button, which will replace all of the actions currently

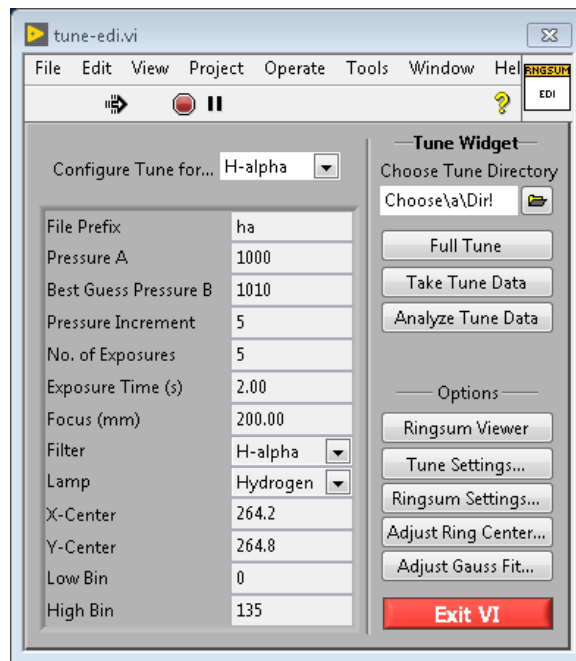


Figure 4.22: The tuner widget runs an automated tuning sequence to take data given tune settings for a specific wavelength and then analyze the data to output the optical pressure setting for that wavelength.

in the queue.

4.6.3 Tuner Widget

The main purpose of the tuning widget, depicted in Figure 4.22, is to automatically take tune data and quickly analyze it to find the optimal pressure for FPI observations of a specific wavelength. The tuning process is explained in Chapter 2. When done manually by a human operator, the process can be lengthy and repetitive, the perfect equation for human error. Automating this process is highly desirable for both efficiency of time and accuracy of execution.

The tuning widget interface displays all of the tune settings for a selected wavelength on the left, and all of the buttons for its various functionalities on the right. The tune settings are stored in a configuration file that can be edited by using the ‘Tune Settings’ dialog box, shown in Figure 4.23. Updates made to the configuration

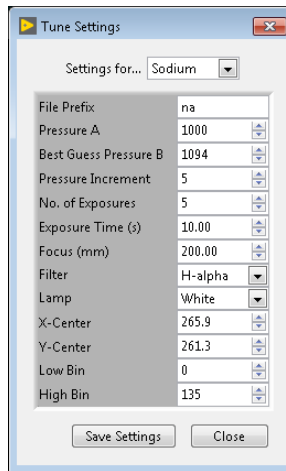


Figure 4.23: The tune settings are stored to a configuration file stored on the control computer. The tune settings dialog box saves any changes to these settings to the configuration file.

file will immediately update the tuning widget front panel with the new information. The tune settings represent all of the inputs that are needed to take and analyze data for a specific wavelength: values for initial pressures and pressure increments; camera settings; focus, filter, and lamp settings; a best guess for the ring center and cutoff bin values.

The user has to select the wavelength they would like to tune to and a tune directory where data can be stored after exposures and later accessed for analysis. If the user decides to start taking tune data, then the tuning widget will use the tune settings for the selected wavelength to set up the calibration process. The first step would be to set up the focus, filter, and lamp mechanisms given the tune settings. Although the focus, filter, and lamp mechanisms are not currently available, the tune data collection VI does leave room for them to be added in later. Next, the widget creates an array of pressures to iterate through based on the tune settings and then sets up the initial pressures in both chambers using the feedback control loop discussed in Section 4.4.4. When the pressures have stabilized in the chambers, the tuning widget takes an exposure according to the tune settings. The pressure in chamber B is then adjusted to the next pressure in the array and another exposure is taken. Each exposure is saved using the user-defined prefix and the pressure it was

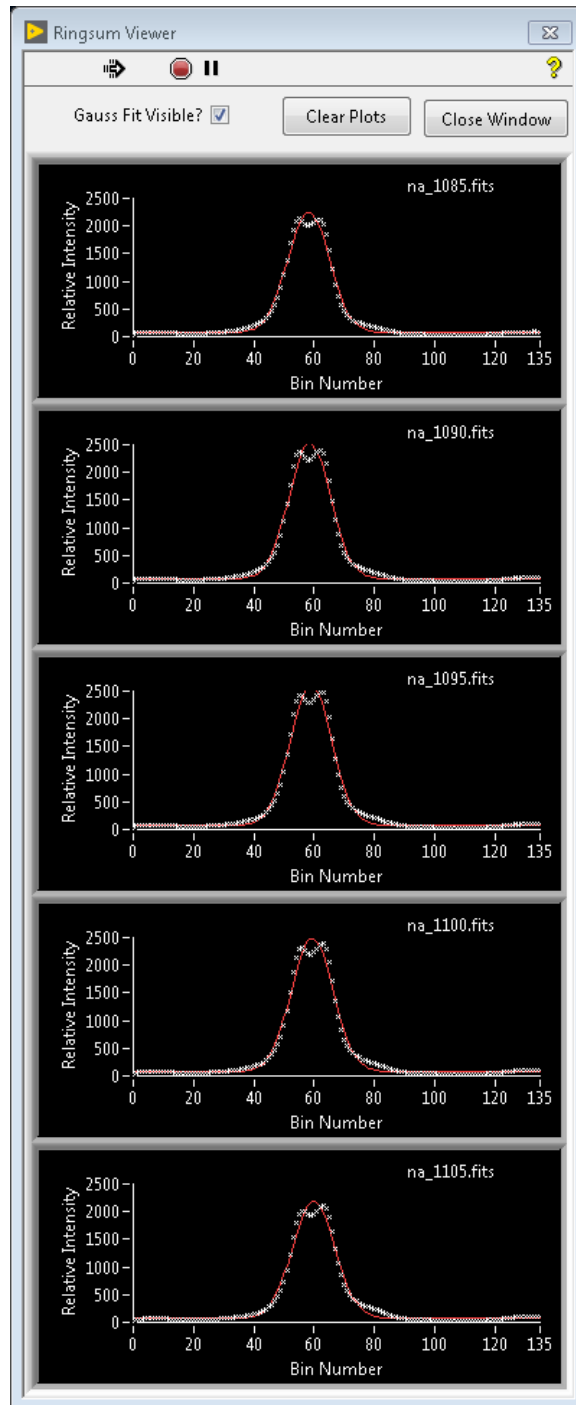


Figure 4.24: The Ringsum Viewer widget displays a stack of the five most recent ring sum outputs in the order they are analyzed.

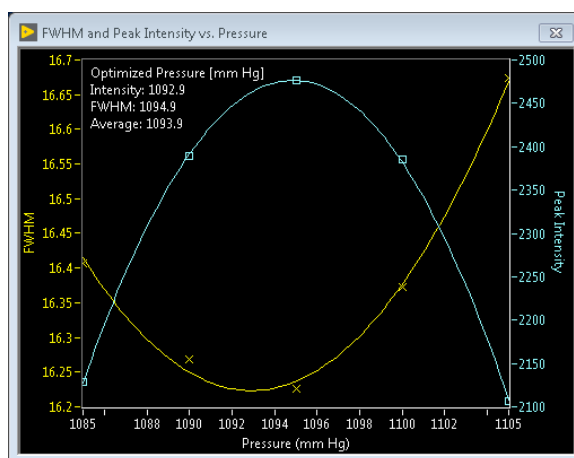


Figure 4.25: The pressure optimization plot shown here is the output of the tune analysis process.

taken at, and then the image is displayed in a separate image display widget. This is repeated until the number of exposures desired is achieved. Tune data is considered obtained at this point.

The next step is to analyze the data to determine the optimal pressure settings for the given wavelength. As described in Chapter 2, the best pressure results in the sharpest peak after ring summing. Details on ring summing are also discussed in Chapter 2. The analysis starts by generating a line profile of each image in the tune series via ring summing. Given the line profile, a gaussian fit to the curve will reveal the full-width half-maximum (FWHM) and peak intensity of the profile. As the gaussian fit is generated for each image, the output from the ring summing and Gaussian fit are displayed in the Ringsum Viewer widget, as in Figure 4.24. This way, the user can monitor the ring sums for issues. After every image is taken care of, the FWHM and peak intensity of each Gaussian fit is plotted against the pressure value in chamber B at the time of exposure, as in Figure 4.25. A parabolic curve is fitted to each the FWHM and the peak intensity values and the extrema of each curve are calculated. The pressures at the extrema and the average of the two values are all displayed in the upper left corner of the plot. The user can utilize this information to make changes to the tune settings as necessary.

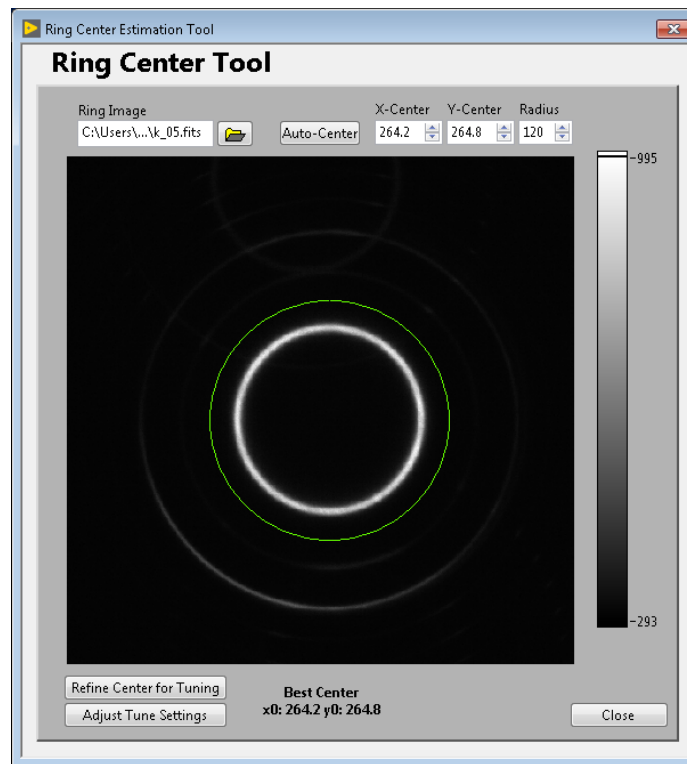


Figure 4.26: A nifty tool for finding the center of an FPI fringe image.

Ring Center Tool

Because the ring center algorithm can take a large amount of execution time, each ring sum is based on the ring center within the tune settings for that wavelength, rather than running the ring center algorithm for every image. The physical ring center does not change by enough during the tune series data collection process to necessitate the processing time it takes to run the ring center algorithm. However, given a bad ring center within the tune settings, the tune analysis will not run smoothly and the ring sums will be distorted.

For this reason, the ring center tool was created to help the user determine the best ring center for running the analysis. The ring center tool is shown in Figure 4.26 and features an image display with a green circle guide overlaid on it. The circle guide can be adjusted in both center and radius to help the user find a reasonable center guess. Two features exist for finding the ring center automatically: (1) the

‘Auto-Center’ button finds a rough center using computer vision, and (2) the ‘Refine Center’ finds a subpixel-resolution center that is best suited for ring summing.

The computer vision ring center function is based on a script written in Python that features the Python module OpenCV, which is used to accomplish computer vision tasks. The script runs pre-processing on the image that is standard for contour detection: first creating a binary image with thresholding, and then running a Gaussian blur to get rid of sharp edges. A circular Hough Transform function is used to find any circles in the image. The Hough Transform finds all possible circles for that size image given a certain threshold for minimum and maximum possible radius and then compares the pre-processed image to all of its possibilities. All of the annular fringes are concentric, and so it doesn’t really matter which circle is picked out if more than one exist. This computer vision algorithm is programmed to find the pixel location of the center of the circle in a matter of milliseconds.

The ‘Refine Center’ function of the ring center tool uses the ring center algorithm described in Chapter 2 to find the best center down to a tenth of a pixel in each direction. However, defining a good initial guess to input to this algorithm significantly decreases the execution time. The computer vision algorithm is usually accurate within one pixel, and so it makes for a good initial guess to the refining algorithm.

Chapter 5

System Testing and Future Procedures

“At that time [1909] the chief engineer was almost always the chief test pilot as well. That had the fortunate result of eliminating poor engineering early in aviation.”

Igor Sikorsky,
Russian-American Aviation Pioneer

One of the objectives of this work is to define the requirements and testing procedures for remote operations before the Investigating Near Space Interaction Regions (INSpIRe) observatory moves to its remote site. The functional requirements of the observatory’s control software and design can be found in Appendix A and are defined by the given observing method and desire for remote operations. Appendix A outlines the requirements for the launchpad, each control widget, and the scripting observing tool.

Each of the widgets, including the launchpad, have been tested individually with their corresponding hardware components and were found to provide the desired control options as per the requirements. A list of test cases and expected functionality is available in Appendix B. At the time of writing this thesis, all expected functionality is accomplished. It is recommended by the author that this checklist be used to ensure

functionality has not been compromised after future additions to the control software or changes to the control computer have been made.

Integration testing of the existing subsystems and software control, including use of observing tools such as the scripting and tuning widgets, has been accomplished. Due to delays in the Fabry-Perot interferometer (FPI) alignment process, full integrated testing involving the FPI is left for future work; however, preliminary FPI tuning tests have shown promising results. Performed and future integrated testing procedures are presented below.

5.1 First Light: Imaging the Moon

One of the major milestones of any observatory is the moment that the first meaningful data is collected. This milestone is referred to as ‘first light’ for optical observatories. First light for the INSpIRE observatory occurred on March 7th, 2017. The test involved opening the dome, homing and moving the siderostat to point at the coordinates of the moon, and recording an image and a snapshot of the observing conditions to a Flexible Image Transport System (FITS) file.

Leading up to this test, the siderostat was not responding correctly when the operator tried to send it to the desired coordinates. It was found that when the operator tried to point at usually-easy-to-find objects (such as the moon or the Pleiades cluster), the siderostat would get lost. The unmodified siderostat control software, written by Jeff Percival, was programmed under the assumption that the siderostat would be in a north-facing configuration. However, after initial testing failed, the difference in angle between the siderostat orientation and geodetic North was measured to be 17° . There are two factors contributing to this offset: (1) the shipping container that the siderostat sits atop is likely not north-south aligned and (2) the bolt pattern of the siderostat attachment to its pier only allows for a discrete set of orientations. Since the astronomical coordinate system is based around the celestial north pole, it is important to factor this offset into the pointing calculations completed by the siderostat control software. Percival assisted in working this offset into his pointing calculations and notes on this math can be found in Chapter 4.



Figure 5.1: This “First Light” image of the moon was taken from the INSpIRe Observatory in Daytona Beach using the siderostat and the SBIG STF-8300M detector.

With the new offset in place, sending the siderostat to the coordinates of the moon became an easy task. It quickly adjusted to the target coordinates and the moon came into view via the SBIG camera in the continuous ‘Focus’ imaging mode. The focus on the lens of the camera was adjusted manually and a 0.1 second exposure was recorded using the SBIG camera control widget. The image can be seen in Figure 5.1. Note that the full moon is about ~ 0.5 degrees on the sky, and so this image represents a field of view of about 6.5 by 4 degrees. Upon saving the image, the header was automatically populated with information about the image, the camera settings, siderostat pointing, environmental sensor readings, and readings from the pressure control system (even though the pressure control system did not contribute to this first light image in any other way!). The first light header is shown in Appendix C as an example of a fully populated header.

5.2 Fabry-Perot Interferometer Fringe Imaging

The next major milestone for the INSpIRE observatory is the imaging of a Fabry-Perot fringe through the dual etalons of the FPI. This does not involve the dome or siderostat, but does involve the pressure control system and the Andor camera. Preliminary fringe testing was performed with a single etalon on November 28th, 2018, and with dual etalons on November 30th, 2018. To simulate the terrestrial Balmer- α emission, a hydrogen lamp is placed at the aperture of the FPI, an H- α interference filter is placed in the optical path, and the pressure chambers are tuned to the particular wavelength using the process described in Chapter 2.

Before the FPI was installed, the tuning widget was put through ‘dummy’ tests, where the Pressure Control System (PCS) is used in feedback loop mode and the camera takes images in between pressure changes; however, even though the pressure chambers were held to pressure, the values for the pressure were ‘dummy’ values, and the images taken were blank images because there was no etalon or calibration lamp in the optical path. The tuning analysis was run on a previously taken tuning set from another FPI. These tests verified that the tuning widget includes all of the building blocks for an integrated tuning test.

The low-resolution etalon (see Chapter 2) was installed and aligned to the defined optical path on November 27th, 2018. A mercury lamp was used to verify that the FPI interference pattern would be captured at the focal plane of the charge-coupled device (CCD). The next day, the hydrogen lamp and H- α interference filter were included in the optical path. Figure 5.2 shows the four low-resolution fringes captured using a single etalon at four different pressures. For each fringe image, the pressure is increased by 50 torr. As the pressure increases, the annulus increases in radius. Pressure was increased incrementally and data was collected using the scripting widget.

On November 30th, 2018, the high-resolution etalon was installed in series with the low-resolution etalon, allowing a full test of the tuning procedure. The pressure differential between the chambers was set to 750 torr, with the high-resolution etalon chamber pressurized to 850 torr and the low-resolution etalon chamber pressurized to

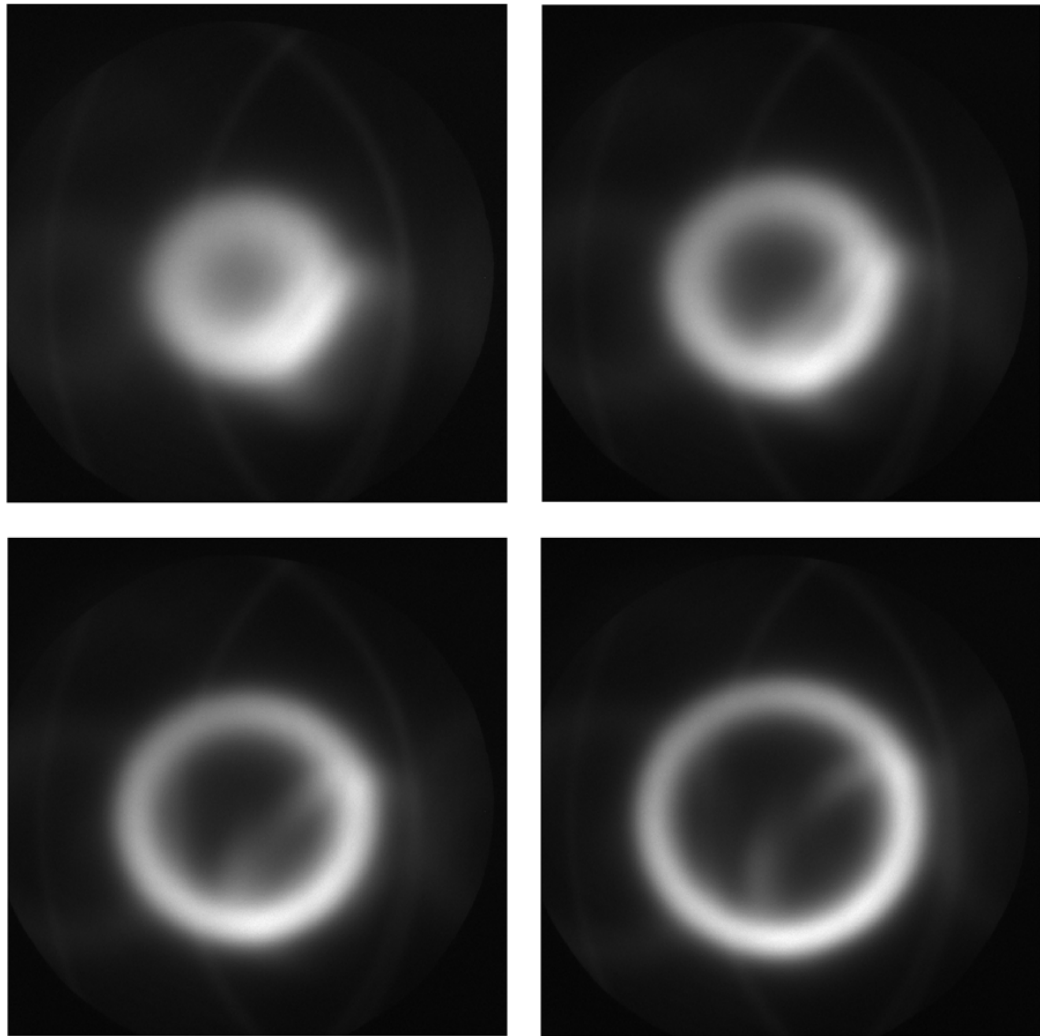


Figure 5.2: Low resolution H- α fringes taken with a single FPI etalon. The radius of the circular fringe pattern increases with increasing pressure (stepped through 1400, 1450, 1500, and 1550 torr). A reflection ring is visible in each image towards the bottom right of the central fringe.

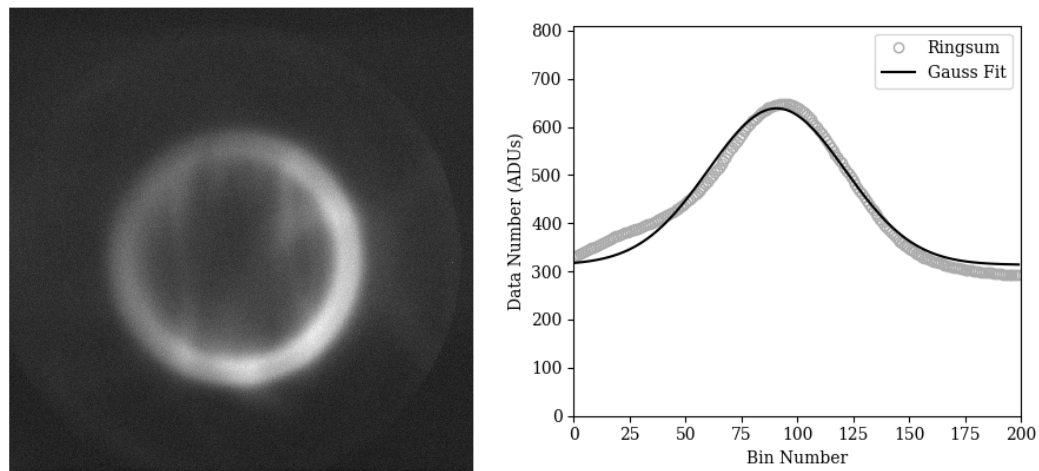


Figure 5.3: An H- α fringe, left, taken with a dual etalon FPI, and its ringsum, right. The fringe image was taken at 835 torr in the high resolution etalon chamber and 1600 torr in the low resolution etalon chamber. The ringsum was taken with an initial bin radius of 25 pixels and 200 bins. Ghostly reflections are visible at the center of the fringe.

1600 torr. The tune was set up to step through five pressures in the high-resolution etalon chamber, centered on 850 torr with increments of 5 torr. Figure 5.3 shows the first image of the tune and its ringsum. The tuning widget was used to increment pressure, take the tune images, and run tuning analysis. Analysis of this preliminary tune did not result in an optimal pressure value. Figure 5.4 shows that the full-width half-maximum (FWHM) optimization curve doesn't have a significant minimum and the peak intensity optimization curve only decreases (see Figure 4.25 in Chapter 4 for an example of ideal optimization curves). Some considerations for this include the stability and isolation of the etalon's environment during installation: this first test was done quite soon after the etalon was installed, but in a practical scenario, the etalon should be allowed to acclimate to its environment, and the etalon chambers, having been opened and closed during installation, may have had some air and moisture mixed into the dry nitrogen. Future fringe testing with the FPI will improve as the etalons acclimate to their new environment.

The first tune using the INSpIRE FPI was inconclusive, as shown in Figure 5.4,

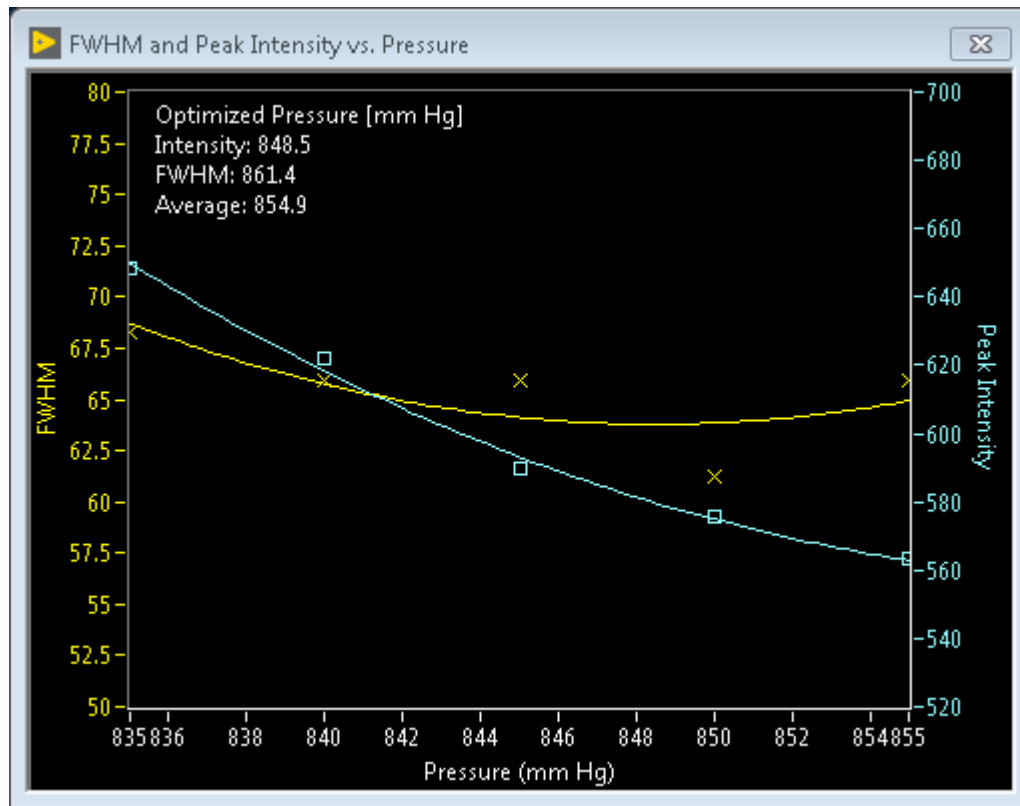


Figure 5.4: The tune analysis window after running tune analysis on the set of tune images. The FWHM hovers around 65 bins, and the peak intensity falls off with increased pressure. This tune is inconclusive.

but successfully demonstrated that the INSpIRE control software is capable of collecting and analyzing FPI tune data. Not only does this integration test check the functionality of the PCS, Andor camera, and their control widgets, but it also acts as a final check of the alignment of the FPI. As seen in Figures 5.2 and 5.3, the central fringe is fully visible in the field of view; however, the annuli are unevenly illuminated and there are many reflections in the image. Future testing of the FPI will benefit from adjustments to the alignment and better beam filling of each etalon's field of view. It is very important to note that when the INSpIRE observatory is moved to its remote site, this procedure will be absolutely necessary before deployment is finished, since the FPI optics are not remotely controllable.

5.3 FPI on the Sky

The final test will be the “FPI First Light” test, where the FPI is coupled to the siderostat for fringe imaging. In this test case, two fold mirrors will be in place, one beneath the siderostat and one atop the FPI, that will bounce light from the siderostat into the FPI aperture. This test could potentially involve all of the hardware components and control widgets, although it could be accomplished with just two (the scripting widget and the Siderostat Control System (SCS) widget) since everything but the siderostat is controllable via the scripting widget.

An easy way to accomplish this would be to open the dome, home the siderostat, and then point at the zenith by rotating the altitude axis by 90 degrees (since the home position is slightly below the horizon). Assuming that the FPI is already tuned to H- α and has an H- α interference filter in place, long exposure time (~ 10 minutes) images can be taken to look for FPI fringes in H- α . This test must be done at night, but closer to dusk or dawn will provide the brightest fringe.

5.4 Remote Testing

It is fully recommended by the author that each of the above tests be done under local, partially local, and fully remote conditions before the INSpIRE observatory is

deployed. Local means that the test is run with the operator sitting in the observatory. Partially local means that the test is run by the operator from a remote location, but that there is a human assistant inside the observatory during the test to handle any manual processes or potential emergency situations. Full remote means that the test is run by the operator from a remote location without any immediate local assistance.

In order to do full remote testing, there are quite a few components that still need to be installed to the observatory. The obvious components would be a robotic focuser, rotatable fold mirrors, and power switched calibration lamps. The less obvious components (which will be useful but not as necessary for partially local testing) are peripheral eyes and ears for the operator, such as cameras and microphones. The local operator has an extra advantage in that regard, since they can hear the siderostat motor speed ramping up and feel the bump of the dome leaves when they hit a hard limit; a remote operator must rely on feedback from the control computer instead.

Chapter 6

A Case Study on INSpIRe Capabilities

“The most incomprehensible thing about the universe is that it is comprehensible.”

Albert Einstein,
Theoretical Physicist

In the following section, a case study is presented investigating the seasonal trends in geocoronal H- α emission intensity as observed by the same Fabry-Perot interferometer (FPI) that is currently being installed in the Investigating Near Space Interaction Regions (INSpIRe) observatory. First, an introduction to geocoronal hydrogen modeling and the expectations of diurnal variation in Balmer- α emission intensities will be provided. Radiative transport models of H- α intensity will be compared to an established dataset taken by *Mierkiewicz et al.* [39] over seasonal and diurnal timescales.

The investigation described here is a testimony to the scientific contributions that a dedicated geocoronal hydrogen observatory can accomplish. The faint geocoronal Balmer series emissions are only visible from the ground given a highly sensitive instrument (e.g. an FPI), and seasonal trends can be investigated more efficiently given the high observing cadence allowed by a dedicated facility. Diurnal and seasonal trends in Balmer- α emission intensity are shown to be observable given the FPI in

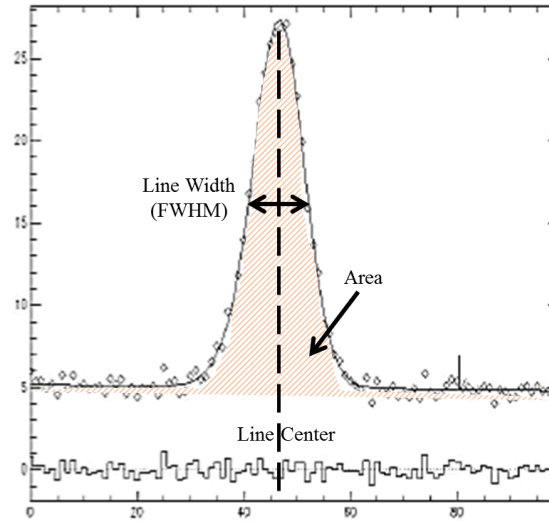


Figure 6.1: Area, line width, and line center are the three measurements that can be made from the FPI fringe data. Figure modified from [38]

this study, and the seasonal trend in observed H- α intensity diurnal asymmetry is presented for the first time. A publication on this investigation is in submission to the *Journal of Geophysical Research: Space Physics* [49].

6.1 From Spectral Data to Balmer- α Intensity

Single-line spectroscopy data from a high spectral resolution FPI can be used to measure (either directly or indirectly) three physical parameters: (1) the number of scatterers or absorbers present is proportional to the area under the line profile; (2) effective temperature of the population is proportional to the line width; and (3) bulk flow of the population is proportional to the change in line center. See Figure 6.1 for a visualization of these parameters in the data.

This work focuses on the intensity of the Balmer- α line profile, which corresponds to the number of H- α emissions received during a given observation. Each observation is taken over a column that follows the line of sight of the instrument, so the resulting emission intensity is an integration along that column. Since observations are taken at night, part of the column will be within the shadow (see Section 2.1.1) and part

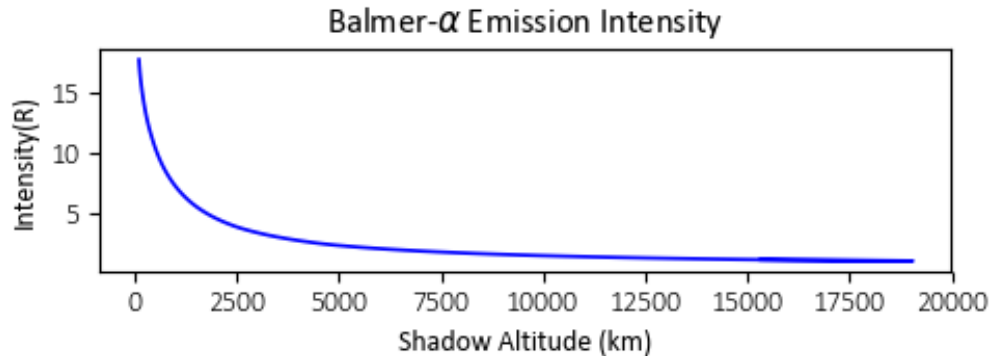


Figure 6.2: A model of intensity vs. shadow altitude shows the nightly trend of higher intensity at dawn or dusk and lower intensity at midnight.

of it will be in the sunlit atmosphere (except for in the anti-solar direction, for which the line of sight (LOS) is parallel to Earth’s shadow). Shadow altitude is defined by the altitude of the point where the observer’s LOS crosses the shadow. If the observer points the instrument at zenith from dusk to dawn, shadow altitude increases towards midnight and decreases towards dawn, meaning that a similar amount of sunlit atmosphere is within the observing column at both dusk and dawn. For this reason, one night of intensity observations is commonly plotted on one increasing shadow altitude axis, as seen in Figure 6.2. In this figure, the intensity is given in rayleighs ($1R = 10^6 / 4 \pi \text{ photons s}^{-1} \text{ cm}^{-2} \text{ sr}^{-1}$), and the shadow altitude is given in kilometers.

As expected, when the observing column includes more of the sunlit atmosphere (lower shadow altitude), the intensity is higher due to the integration of emission intensity over the column. At midnight, the LOS is in the anti-solar direction, meaning that there should be no sunlit atmosphere in the observing column and therefore no intensity. However, an emission type called multiple scattering is capable of generating Balmer- α signal from within the shadow. As explained in Chapter 1, H- α emission originates in the sunlit atmosphere due to interactions between atomic hydrogen and incoming solar Lyman- β photons. However, the radiation from that emission can be absorbed and re-emitted (and absorbed and re-emitted again!) on its journey to the

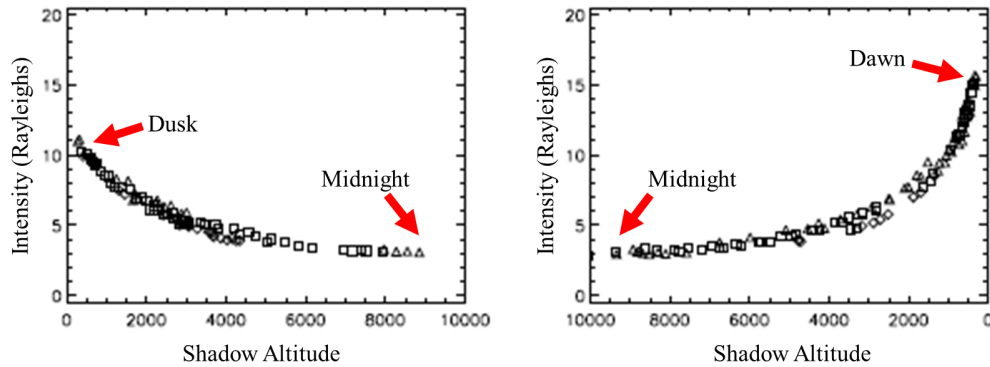


Figure 6.3: Diurnal asymmetry in the intensity can vary by several rayleighs. Figure modified from [38].

observer. The total observed intensity is actually a summation of the single and multiple scattering within the observing column. Modeling the expected H- α emission intensity requires radiative transport calculations, which account for both single and multiple scattering interactions.

It is expected, as shown in Figure 6.2, that the observed intensity will be lowest at midnight and highest at dawn or dusk due to observing geometry. However, an asymmetry between dusk and dawn has been observed and noted in several studies [23, 26, 27]. Figure 6.3 shows data taken by *Mierkiewicz et al.* [38]. Note the symmetrical shadow altitude axes; the left panel shows intensity variation from dusk to midnight, and the right panel shows midnight to dawn. The difference in intensity between dusk and dawn is on the order of several rayleighs for this observation set. Diurnal variation in intensity is indicative of a change in the atomic hydrogen density between evening and morning. In Section 6.3, a case is made for a seasonal variation in the diurnal asymmetry (i.e. the difference in intensity between dusk and dawn may wax and wane over the course of a year).

6.2 Radiative Transport Modeling

H- α emission intensity is modeled using the Lyman Atmospheric Observations Radiative Transport (`lyao_rt`) code of *James Bishop* [1], which generates LOS radiances based on an input scattering atmosphere. The `lyao_rt` code is often coupled with mesospheric/thermospheric temperature and density profiles generated by the Mass Spectrometer and Incoherent Scatter model (MSIS) model [10, 29], although it also allows for a user-specified hydrogen profile (based on exobase density, mesopause density, and vertical flux parameters) to be substituted for the MSIS hydrogen profile (see e.g. [50]). The thermospheric model atmosphere is extended to higher altitudes using either the *Chamberlain* model exosphere [7] or the *Bishop* analytic exosphere model [51]. Here the evaporative case of the Bishop analytic model is employed, where the exospheric satellite atom population (see e.g. [7]) is characterized by the kinetic distribution of the ballistic atom population, calculated using the exobase density and temperature from the input thermospheric model atmosphere. The evaporative case is used here as a simplifying assumption, as the exobase hydrogen density and temperature inputs come directly from NRLMSISE-00, thus limiting the number of free parameters in the study.

The `lyao_rt` code can be described as having two distinct stages: (1) the spherically symmetric thermospheric model atmosphere is extended to exospheric altitudes and global radiative transport is applied to obtain a Balmer- α source function, and (2) observational viewing geometry is used to calculate a LOS irradiance (refer to Figure 6.4). The LOS output is used as a direct comparison to observed intensity. If the model shows good agreement with observations, then the atomic hydrogen density profile input (whether given from NRLMSISE-00 or otherwise defined) is considered to be nominally correct. Note that the atomic hydrogen density profile has not been directly measured, it in itself is also a model. This kind of approach is called forward modeling.

Within the first stage of the `lyao_rt` code, the input thermospheric model is provided by NRLMSISE-00, including vertical temperature, O₂, and H profiles. If the `lyao_rt` input observation time and observer longitude information provided for MSIS

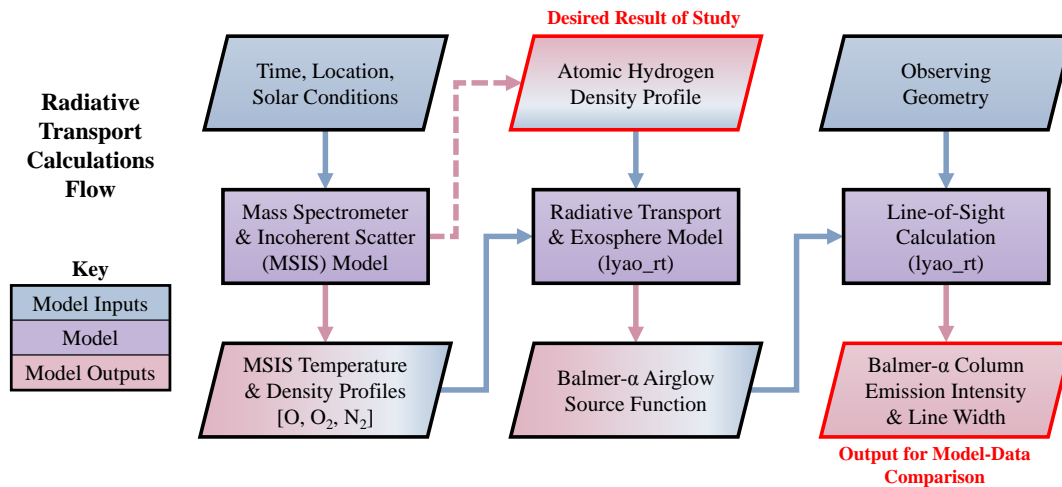


Figure 6.4: The two stage lyao_rt process is initialized with an estimate for hydrogen density from NRLMSISE-00, and then radiative transport and line-of-sight calculations can be completed.

indicates a solar zenith angle (SZA) that is below the horizon ($SZA > 100.5^\circ$), then the latitude and longitude of the MSIS call is re-adjusted to represent the atmosphere near the dawn or dusk terminator ($SZA = 100.5^\circ$). The re-adjustment to the thermospheric model atmosphere allows lyao_rt to account for single scattering in the direction from which sunlight is entering the atmosphere with atmospheric conditions representative of that location. Because Balmer- α intensities are highly dependent on the Sun-Earth geometry at the time of data collection, nautical twilight model run times were chosen to provide better consistency in the Sun's position over the year for the seasonal model/data comparisons presented here. Figure 6.5 indicates MSIS call latitude and longitude adjustments based on lyao_rt nautical twilight input times.

6.3 Model-Data Comparison

The INSPIRE Observatory is poised to collect data on a long timeline in order to explore atmospheric trends over the course of a year or the course of a solar cycle (~ 11 years). As an exploration of the expected results from such observing campaigns, predicted and observed seasonal trends are investigated here. The modeled trends are

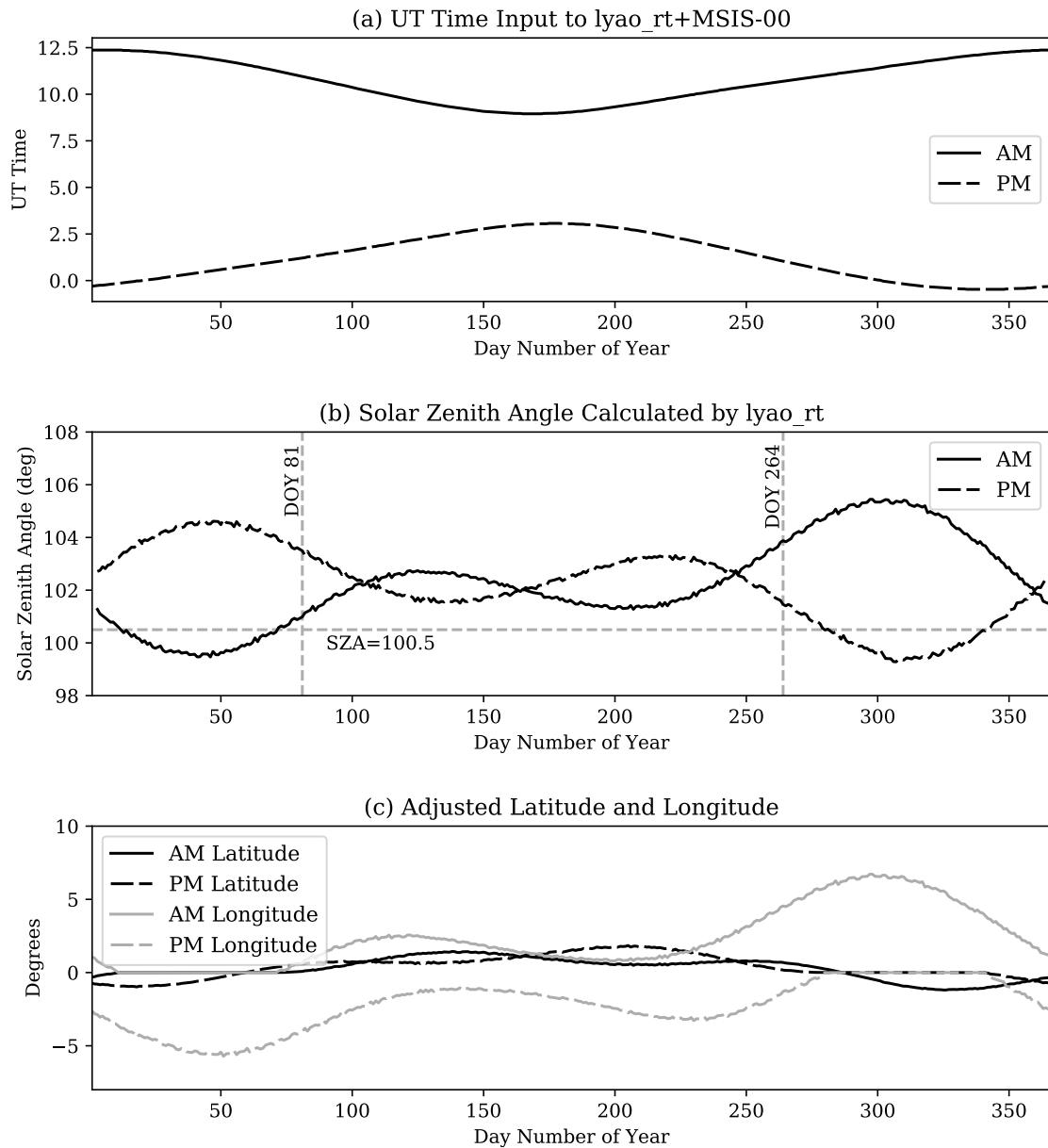


Figure 6.5: (a) To account for changes in Sun-Earth geometry over the course of the year, the UT time input to the lyao_rt code was adjusted to nautical twilight dusk and dawn for every day of year (DOY). (b) The lyao_rt code calculates a solar zenith angle (SZA) using the date, time, and observer location inputs. If the SZA is greater than the SZA at the terminator ($SZA=100.5^\circ$), then the observer location is adjusted to match the terminator. (c) By using nautical twilight as the input time, the latitude is adjusted by no more than 2 degrees and the longitude is adjusted by no more than 7 degrees away from the observer's location.

generated using inputs based on the conditions of observation. The observations were taken by Ed Mierkiewicz on the same FPI that is used in the INSpIRE observatory over 20 months in the 2000-2001 time frame [39]. Model predictions and data selection are described below, along with the results and implications of the model-data comparisons.

6.3.1 Seasonal Trend in H- α Intensity Predictions

To explore both diurnal and seasonal trends, `lyao_rt + NRLMSISE-00` was run in the morning (at nautical twilight dawn) and evening (at nautical twilight dusk) for every day of the year using solar maximum and geomagnetically quiet conditions (f10.7 index, a measure of the 10.7 cm radio flux from the Sun which directly corresponds to solar activity, is set to 170; Ap index, a measure of the magnetic effects of solar activity on Earth, is set to 5). The observer's geographic location is identical to the location of observations at Pine Bluff Observatory (PBO), WI, but adjustments to latitude and longitude are made within `lyao_rt` to account for the relevant scattering environment (refer to Section 6.2). Adjustments made fall within 2 degrees in latitude and 7 degrees in longitude, as shown in Figure 6.5. Because the observations were taken at solar maximum, the solar Lyman- β line center flux is assumed to be 9×10^9 photons $\text{cm}^{-2} \text{s}^{-1} \text{\AA}^{-1}$, as used in the modeling study by Anderson et al. [52]. Model inputs for seasonal trend analysis are summarized in Table 6.1. Modeled LOS calculations are accomplished using simulated zenith pointings for making consistent analyses of seasonal trends. When analyzing direct model-data comparisons for a particular subset of the data, the actual LOS pointings from the observation are used in modeling.

Figure 6.6 (a) and (b) show the predicted variation of modeled H- α emission intensity over the course of the year for low shadow altitudes at nautical twilight dusk and dawn times. In Figure 6.6 (c), the difference between post-midnight morning intensity and pre-midnight evening intensity was taken as a measure of diurnal variation over the year. From Figure 6.6, it is apparent that a seasonal trend in the H- α emission intensity diurnal asymmetry is expected.

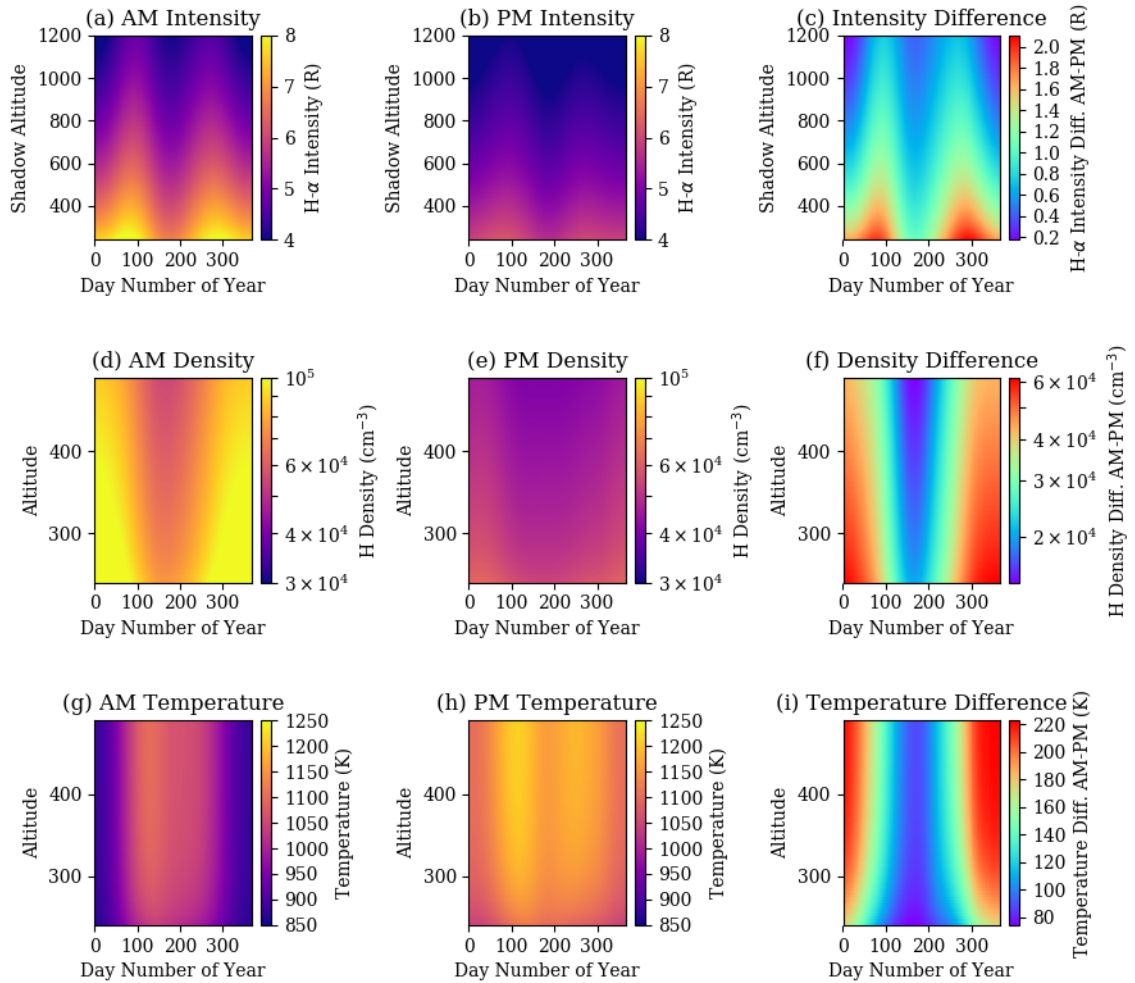


Figure 6.6: Predicted seasonal variation in H- α emission intensity only varies by as much as a few Rayleighs during solar maximum with maxima at different intensities for morning versus evening predictions. (a) A semi-annual oscillation is visible in the AM modeled intensity and (b) in the PM modeled intensity up to 1200 km shadow altitude. (c) The ratio of AM intensity to PM intensity shows semi-annual oscillation with maxima near the equinoxes and local minima near summer and winter. All panels show that intensity falls off with shadow altitude. Hydrogen density, on the other hand shows an annual oscillation in (d) morning H density and (e) evening H density up to the exobase (~ 500 km). This also results in a diurnal density difference (f) that shows an annual variation. Temperature up to the exobase is also shown here: morning temperatures in panel (g), evening temperatures in panel (h), and the diurnal temperature difference is shown in panel (i).

Table 6.1: lyao_rt + NRLMSISE-00 Model Inputs

Atomic Physics Parameter	Value(s)
Solar Emission Line	Lyman- β (1026 \AA)
Solar Line Center Flux	9×10^9 photons $\text{cm}^{-2} \text{s}^{-1} \text{\AA}^{-1}$
H- α Branching Ratio	0.128
Observing Parameter	Value(s)
Latitude, Longitude*	43.0776° N, 89.6717° W
Day of Year**	1 thru 366
Year	2000
Morning Time	Local Nautical Dawn
Evening Time	Local Nautical Dusk
f10.7, f10.7a**	170
Ap**	5

* Adjusted to terminator (see Figure 6.5).

** When generating model runs for comparison to individual datasets, these parameters are determined from the conditions of the observations (see Table 6.2).

Diurnal intensity variation is predicted to be at a maximum near day of year (DOY) 87 and DOY 278. The spring maximum occurs ~ 6 days after vernal equinox (DOY 81), and the autumn maximum occurs ~ 13 days after autumnal equinox (DOY 265). A local minimum exists in the summer, around DOY 168, and the overall minimum is in winter, near DOY 6. The summer minimum occurs ~ 5 days before summer solstice (DOY 173) and the winter minimum occurs ~ 16 days after winter solstice (DOY 356). The extrema are predicted to fall within half of a month of the equinoxes or solstices under the specified observing conditions.

Figure 6.6 (d) and (e) show the modeled seasonal trend in hydrogen density with altitude for both the morning and evening, and (f) shows the diurnal difference in hydrogen density. The model predicts that, while hydrogen density shows a clear annual oscillation, H- α intensity has a semi-annual oscillation. Hydrogen density is predicted to be highest near winter solstice (DOY 356) and lowest near summer solstice (DOY 173). The minimum in hydrogen density aligns well with the summer minimum in H- α intensity, but where there is a maximum in hydrogen density, there

Table 6.2: 2000-2001 Balmer- α Observing Conditions

Series	Month, Year	AM Spc ^a	PM Spc ^a	Avg. DOY ^b	Avg. f10.7	Avg. Ap
1	Jan, 2000	2	7	9	160.3	5.5
2*	Feb, 2000	16	21	34	149.1	15.6
3*	Mar, 2000	45	14	64	209.7	7.9
4	Apr, 2000	9	23	94	194.2	28.9
5*	May, 2000	27	41	122	159.4	16.1
6*	Jun, 2000	35	23	159	184.6	10.9
7*	Aug, 2000	15	12	246	173.2	12.1
8	Sep, 2000	0	1	272	205.9	17.4
9	Oct, 2000	11	5	303	181.3	12.7
10	Nov, 2000	34	0	332	178.1	9.5
11*	Jan, 2001	33	31	21	152.2	10.8
12	Feb, 2001	16	21	52	133.4	4.5
13	Mar, 2001	0	12	59	272.0	40.0
14	Apr, 2001	0	3	117	193.0	4.0
15*	May, 2001	25	11	139	145.0	10.0
16	Jul, 2001	0	6	195	145.3	11.7
17*	Aug, 2001	28	48	232	160.5	9.6
18	Sep, 2001	13	0	269	274.2	22.6
19	Oct, 2001	5	6	290	218.0	4.2
20	Nov, 2001	4	5	321	196.8	6.9

^aNumber of Spectra with: Shadow Altitudes < 1,000 km, observation zenith distance $\leq 45^\circ$, galactic latitudes $> 10^\circ$ from the galactic plane ($l = 0$)

^b Day of Year (DOY): year 2000 is a leap year, as such 02/29/00 is day 60

* Indicates selected datasets

is another minimum in intensity.

As temperature likely plays a significant role in hydrogen density seasonal trends, Figure 6.6 (g) and (h) show the predicted temperature trend in the morning and evening, and Figure 6.6 (i) shows the diurnal temperature difference. The highest temperatures are in the summer, with two maxima on either side of summer solstice and a deep minimum in winter. Whereas hydrogen density and H- α intensity tend to fall off with altitude, temperature increases with altitude in the upper thermosphere.

6.3.2 Data Selected

In a series of 20 observing runs taken between 2000 and 2001 at PBO, Wisconsin (43.07° N, 270.33° E), *Mierkiewicz et al.* [39] collected Balmer- α line profiles using a dual etalon Fabry-Perot spectrometer with a resolving power of $R \approx \lambda/\Delta\lambda \approx 80,000$ at Balmer- α (spectral resolution $\sim 0.08 \text{ \AA}$). The spectral resolution of the instrument is sufficient for separation of the galactic H- α emission from geocoronal emissions. All observations considered here were taken at least 10 degrees away from the Galactic plane and on clear nights within a week of new moon. The instrument is coupled to a siderostat that allows for precise target pointing and tracking; throughout all data sets, the observations were taken as close to zenith as possible given the constraint of avoiding the galactic plane. See [39, 38] for further details.

The 20 monthly datasets cover 11 out of the 12 months of the year between 2000 and 2001, near solar maximum. Solar conditions vary between 122 and 277 in f10.7 (average 181) and geomagnetic conditions vary between 2 and 82 in Ap index (average 13). Each dataset includes multiple nights of observations within the two-week period centered on new moon. For this reason, a weighted average for f10.7, Ap, and day of year (DOY) has been calculated for each series of observations and can be found in Table 6.2. A complete table of observations and observing conditions can be found in [39].

Data were selected for model-data comparison from the observations with considerations for solar and geomagnetic conditions, observation viewing geometry, and number of observations taken at low shadow altitudes, where diurnal asymmetry is most apparent. Observations that were taken outside of geomagnetically normal and solar maximum conditions ($145 < f10.7 < 230$ & $Ap < 25$) were not considered in order to prevent outliers due to geomagnetic activity. Observations that were taken within ten degrees of the galactic plane and observations that were taken outside of 45 degrees of zenith were removed. Data are grouped into post-midnight morning (AM) if the time of observation is after local midnight or pre-midnight evening (PM) if the time of observation is before local midnight. All datasets with less than five observations between 400 and 800 km shadow altitude were not included in this study.

Within these selection criteria, seven series were selected to investigate diurnal

and seasonal trends in emission intensity. The data selected for analysis comes from Series 11 (DOY 21) and Series 2 (DOY 34) near the winter solstice, Series 3 (DOY 64) and Series 5 (DOY 122) near the vernal equinox, Series 6 (DOY 159) near the summer solstice, and Series 17 (DOY 232) and Series 7 (DOY 246) near the autumnal equinox. The average f10.7 index for the selected datasets is 171.1, and the average Ap index is 11.0. In Figure 6.7, four of the selected intensity datasets (Series 11, 5, 6, and 7) are plotted against shadow altitude along with an `lyao_rt + NRLMSISE-00` modeled intensity that corresponds to the average DOY and solar conditions of the dataset using a zenith LOS pointing for all shadow altitudes. Note that Figure 6.7 plots morning and evening on the same shadow altitude axis, with observations taken closer to midnight near the highest shadow altitudes and observations taken closer to dawn or dusk at the lowest shadow altitudes. A linear fit was made to each dataset between 400 and 800 km, where diurnal variation is most apparent in observations. The linear fit to the data is used in data analysis later on (see e.g. Figure 6.10).

6.3.3 Results

From Figure 6.7, it is immediately apparent that the magnitude of the intensities generated by `lyao_rt + NRLMSISE-00` are several rayleighs lower than the observed intensities. The discrepancy has been noted in previous studies and has yet to be fully resolved [3, 30, 50]. To investigate further, an observed-to-MSIS intensity ratio was calculated for each of the selected series datasets, seen in Figure 6.8. In order to account for varying coverage in altitude from series to series, the AM and PM observations and `lyao_rt + NRLMSISE-00` modeled intensities for each dataset have been binned into 100 km shadow altitude increments and then the ratio is taken between the two. For each of the selected datasets in Figure 6.8, the AM and PM observed-to-MSIS intensity ratio demonstrates that observed intensity is consistently 1.5 to 2.5 times higher than `lyao_rt + NRLMSISE-00` predicted intensities for both morning and evening model-data comparisons. Interestingly, from fall to spring (Series 7, 11, and 5), the morning modeled intensities appear to have a higher ratio than the evening modeled intensities, and in the summer (Series 6), the evening ratio is

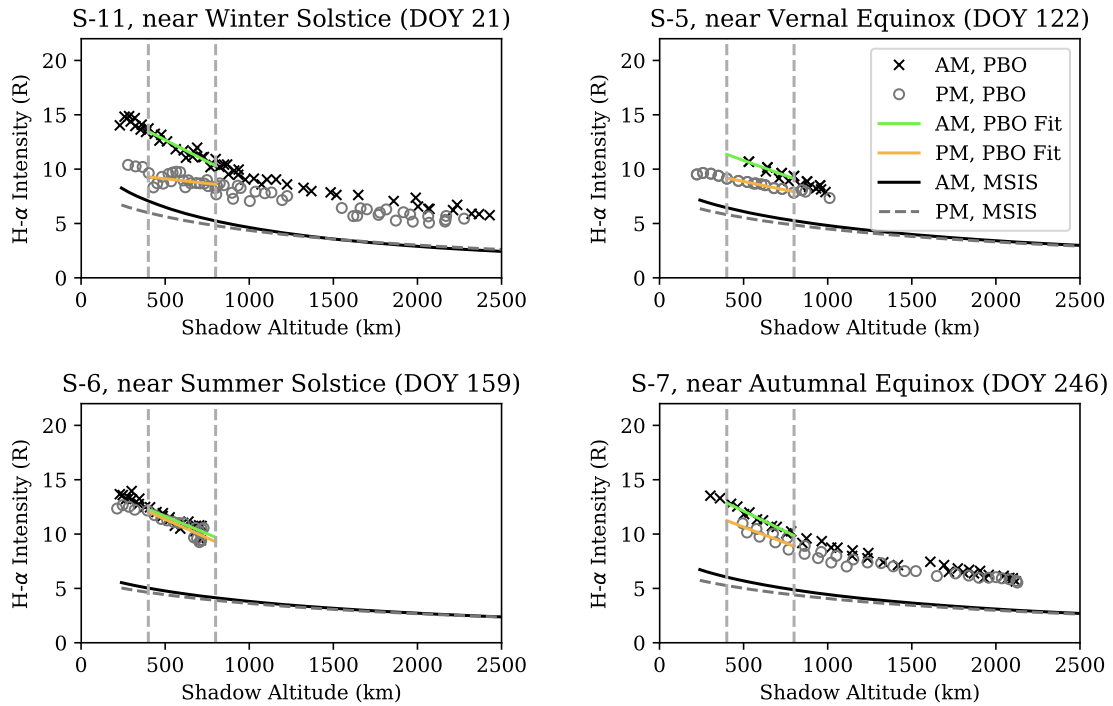


Figure 6.7: Selected observations from the *Mierkiewicz et al.* [39] series of data are plotted (\times for AM and \circ for PM) alongside lyao_rt + NRLMSISE-00 modeled intensities (solid for AM and dashed for PM). Both morning and evening runs are plotted on the same shadow altitude axis. Model runs are based on average DOY and solar conditions of each observation run (see Table 6.2). Grey dotted lines indicate the shadow altitude boundaries for analysis, between 400 and 800 km (see Figure 6.10), where diurnal asymmetry has been shown to be most apparent in observations. Solid green (AM) and orange (PM) lines indicate a linear fit to the observations between these boundaries.

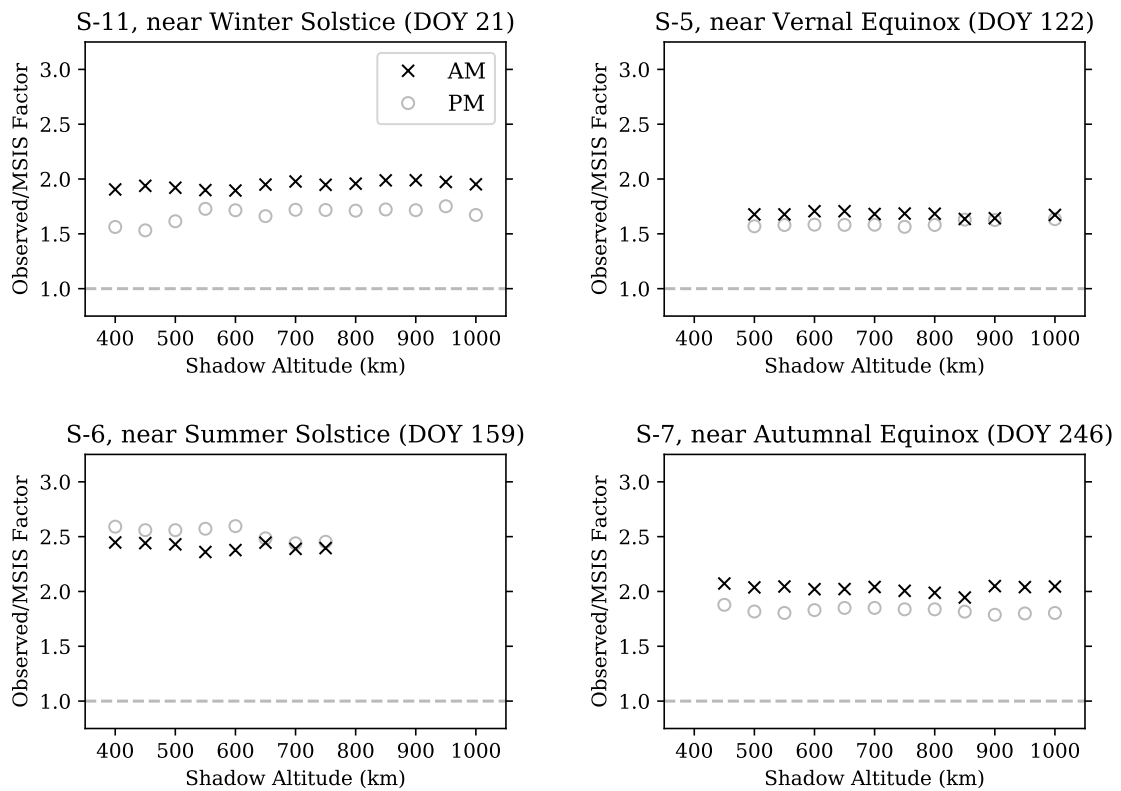


Figure 6.8: Observed-to-MSIS ratios are calculated for AM intensity (indicated by \times) and PM intensity (indicated by \circ) and plotted against shadow altitude. Due to each observation having varying shadow altitude coverage (see Figure 6.7, each point is an average over 100 km shadow altitude).

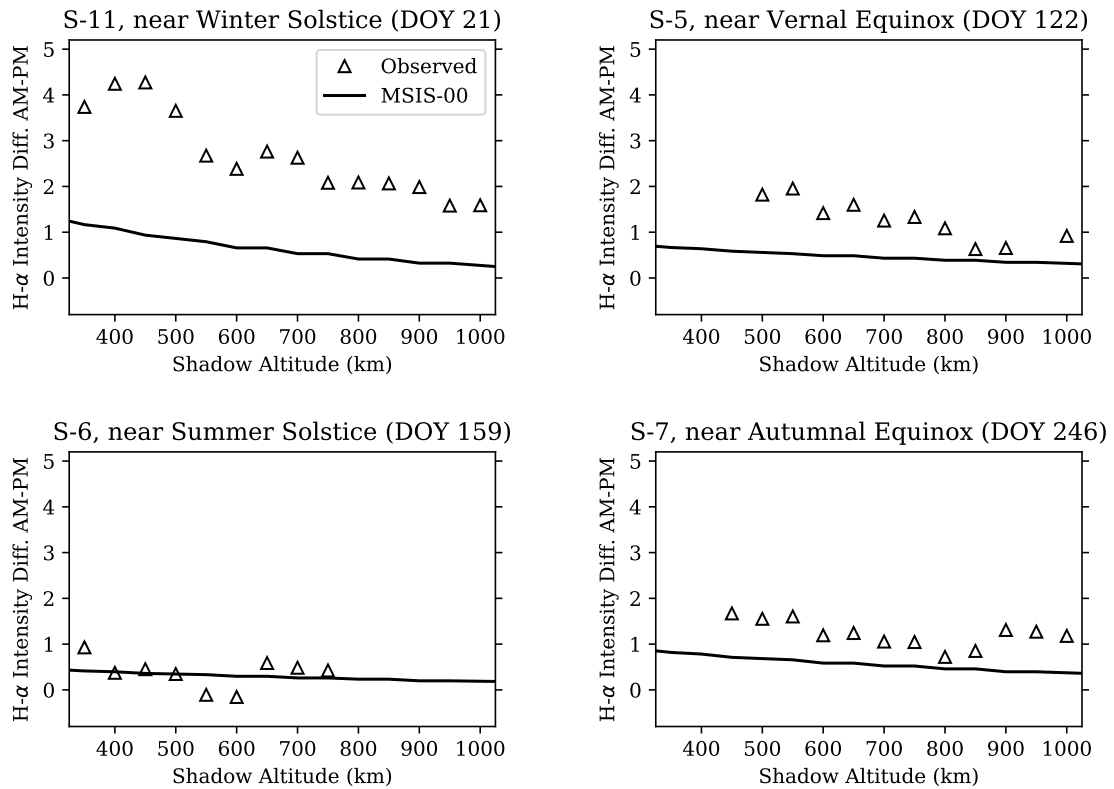


Figure 6.9: The difference of morning and evening intensity is plotted against shadow altitude for observed and modeled intensity. Due to each observation having varying shadow altitude coverage (see Figure 6.7), each observed data point is an average over 100 km shadow altitude.

higher.

In Figure 6.9, the difference between morning and evening observed intensity is again binned over 100 km shadow altitude increments and now plotted alongside the lyao_rt + NRLMSISE-00 intensity difference. Although the magnitude of overall intensity is lower for MSIS, the magnitude of the diurnal asymmetry between observed and modeled intensities is in good agreement for several of the datasets (e.g. Series 5, 6, and 7). Note, modeled intensity differences were generated using each series datasets' unique observing conditions. The summer solstice dataset (Series 6) shows the best agreement between observed and modeled diurnal asymmetry for all shadow altitudes below 1000 km. The datasets at the equinoxes (Series 5 and 7) show good agreement at some altitudes, but not all, and the winter solstice dataset (Series 11) is not in agreement.

A seasonal trend is apparent within the selected datasets. In Figure 6.10, lyao_rt + NRLMSISE-00 modeled intensities between 450 and 750 km shadow altitude are averaged and plotted over DOY for a simplified picture of the seasonal trend at low altitudes. In this case, an average value is used for solar conditions during the observing period (refer to Table 6.1 for model inputs). As a measure of diurnal variation, the difference between morning and evening values for intensity are plotted over DOY. Averages for the AM intensity, PM intensity, and diurnal difference have also been calculated for each of the selected observation datasets between 400 and 800 km shadow altitude. Error bars shown in Figure 6.10 indicate $\pm 1\sigma$ from the mean for each observed dataset.

The average intensity shown in Figure 6.10 (a) reiterates the factor of two difference between model and observations. Beyond that, a semi-annual trend is predicted in both AM and PM intensity observations, but neither AM nor PM data sets show such a clear trend. The AM/PM intensity difference shown in Figure 6.10 (b) shows the best agreement between model and observations between the spring and autumn maxima (series 5, 6, 17, and 7), but the winter observations (series 11, 2, and 3) do not align with the seasonal prediction. It should be noted that the nonconformist observation sets, series 11, 2, and 3, are from the same two-month period but set a year apart, which may indicate that the model is not accurately reflecting winter

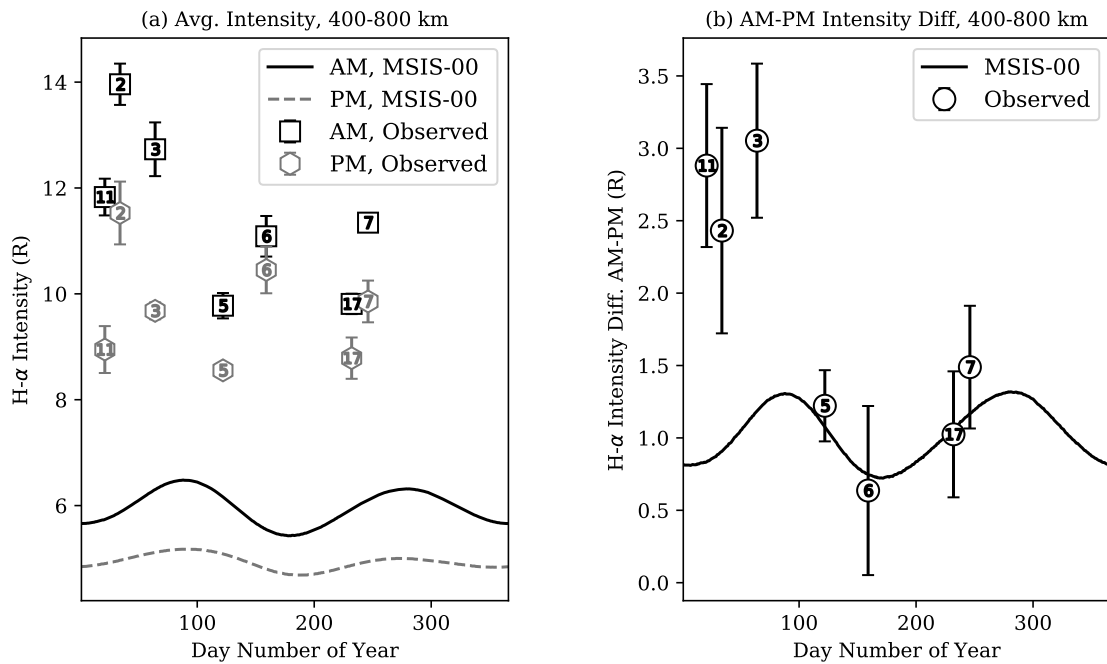


Figure 6.10: Intensities generated by `lyao_rt + NRLMSISE-00` are averaged from 400 to 800 km shadow altitude. (a) Morning and evening intensity averages are plotted over day of year for model and observed data. (b) Difference between AM and PM intensity for model and observed data. Observed differences are plotted using open symbols for each selected series dataset (square for AM, hexagon for PM, and circle for the difference). Error bars indicate $\pm 1\sigma$ from the mean.

conditions.

6.3.4 Implications

The `lyao_rt` + NRLMSISE-00 predicted intensity for both morning and evening are 1.5 to 2.5 times lower than the morning and evening intensity observations from PBO. This is consistent with previous studies that have seen the same result in comparisons between MSIS hydrogen and Fabry-Perot observations [30], as well as between MSIS hydrogen and radar data [3]. The factor of two difference between the observed signatures of hydrogen density and the MSIS-derived quantities indicates a discrepancy with the hydrogen density output of NRLMSISE-00. This likely stems from the indirect method from which hydrogen density is inferred within the NRLMSISE-00 model using charge exchange relations. Atmosphere Explorer-C (AE-C) took measurements of hydrogen and oxygen ion density, as well as neutral atomic oxygen density, at ~ 300 km. The uncertainty on the ion density measurements were each 10% [17], and the uncertainty of the neutral atomic oxygen density measurements were no more than 30% [53]. The AE-C mass spectrometer data are the sole datasets that contribute to NRLMSISE-00 hydrogen density output [12, 29, 54, 10]. However, each of the datasets were taken between late December and early February [18, 19], where the largest discrepancy in our model-data comparison lies. Additionally, the work done by *Kotov et al.* [3, 4] is based on ground-based radar measurements taken in Northern hemisphere winter during solar minimum, and their result also shows a discrepancy between MSIS and observations of a factor of ~ 2 . The AE-C measurements were also taken during solar minimum [18, 19], so there is no hydrogen density data included in NRLMSISE-00 for solar maximum. At this time, the only conclusion that can be made is that absolute H- α intensity derived from radiative transport is a factor of ~ 2 lower than observed intensity.

The intensity observations are consistent with higher densities post-midnight compared to those in the evening twilight. This result is consistent with modeled densities in the middle thermosphere as shown in [33]. Compared to *Tinsley's* estimate of a 20% increase in brightness between evening and morning [25, 23], the *Mierkiewicz et*

al. [39] dataset shows a $\sim 20\%$ increase in H- α intensity in the winter and a $\sim 5\%$ increase in the summer months between evening and morning. This value becomes $\sim 18\%$ at vernal equinox and $\sim 12\%$ at autumnal equinox for the same dataset. The estimate by *Shih et al.* [26] of 10% also falls within the range measured here. Meanwhile, `lyao_rt` + NRLMSISE-00 modeled intensity variation predicts an increase from evening to morning of 15% at the solstices and 20% at the equinoxes. The exobase density changes in the NRLMSISE-00 input atomic hydrogen density between evening and morning were close to ~ 1.9 in the winter and ~ 1.4 in the summer, which agrees with MSIS [29]. Exobase density estimations through forward modeling analysis (see e.g. [27]) have not been obtained for the *Mierkiewicz et al.* [39] intensity observations.

A seasonal trend in observed diurnal intensity variation difference is clearly shown in Figure 6.10 (b). The difference between morning and evening intensities is highest during the winter months of the year and lowest during the summer months. The `lyao_rt` code calls NRLMSISE-00 to obtain temperature, hydrogen density, and hydrogen column density in order to make calculations for radiative transport. Figure 6.11 shows these parameters calculated from the NRLMSISE-00 output. The seasonal trend in the MSIS-generated temperature and hydrogen density taken at 494.0 km altitude, seen in Figure 6.11 (a-d), clearly shows the anti-correlation between temperature and hydrogen density within the thermosphere. Where temperature at the exobase is lower in winter, hydrogen density is higher, and vice versa in summer. Note that the diurnal difference in temperature and hydrogen density are both highest in the winter and lowest in the summer.

Figure 6.11 (a-d) may reflect the role that temperature gradients play in the vertical distributions of hydrogen over diurnal and seasonal timescales. Past research has indicated that diffusive equilibrium is not enough to explain neutral composition in the thermosphere [55, 56, 33]. Instead, vertical advection may have a stronger effect. Upward vertical winds in the summer results in a redistribution of the light species (e.g. hydrogen) over altitude. This decreases the density of atomic hydrogen at the exobase. The opposite effect happens in the winter, when downward vertical winds occur due to cooler exospheric temperatures. The temperature variation over the day-night cycle can also cause vertical advection; pre-midnight evening temperatures are

higher and hydrogen density is lower, and post-midnight morning temperatures are lower and hydrogen density is higher (see e.g. Figure 6 from *Qian et al.* [33])

Since the observations presented in this study represent a column emission rather than a particular altitude, Figure 6.11 also includes the modeled hydrogen column density in panels (e-f), taken over ~ 100 to 60,000 km altitude. Although there appears to be a seasonal anti-correlation between temperature and column density, hydrogen column density exhibits a semi-annual variation in both absolute column density and the diurnal difference instead of an annual oscillation. Regardless, the seasonal trend in the diurnal difference of hydrogen column density still indicates a higher difference in winter than summer. Modeled intensities, both absolute and the diurnal difference, also show a semi-annual variation with DOY, but extrema in H- α intensity do not correspond to the same DOYs as extrema in hydrogen column density. The semi-annual trend in predicted intensity is shown in Figure 6.10. The summer minimums in diurnal intensity and diurnal hydrogen column density variation align during summer, but the hydrogen column density difference is predicted to be close to maximum during winter when modeled H- α intensity difference is at a second minimum. Although several of the observed intensity datasets in Figure 6.10 do not fit the predicted trend (e.g. Series 11, 2, and 3), many of the datasets fit within 0.5 R. The model of diurnal variation in intensity appears to underestimate the data in winter by ~ 1.5 -2 R. More data coverage between autumn and spring are needed to find a significant result, but current analysis indicates a much larger diurnal asymmetry than predicted during the winter months.

The plot of diurnal hydrogen column density variation in Figure 6.11 (e) shows the highest column density difference in winter, with a small dip early in the year, and the lowest column density difference in the summer. The modeled diurnal intensity variation in Figure 6.10 (b) has deep minima at both winter and summer. Although the seasonal trend in intensity observations does not always follow the lyao_rt + NRLMSISE-00 model prediction, the intensity observations do appear to follow a similar seasonal trend as hydrogen column density and hydrogen column density at the exobase. Figure 6.12 shows observed H- α intensity plotted against the predicted hydrogen density at 494 km, (a) and (b), and against the modeled hydrogen column

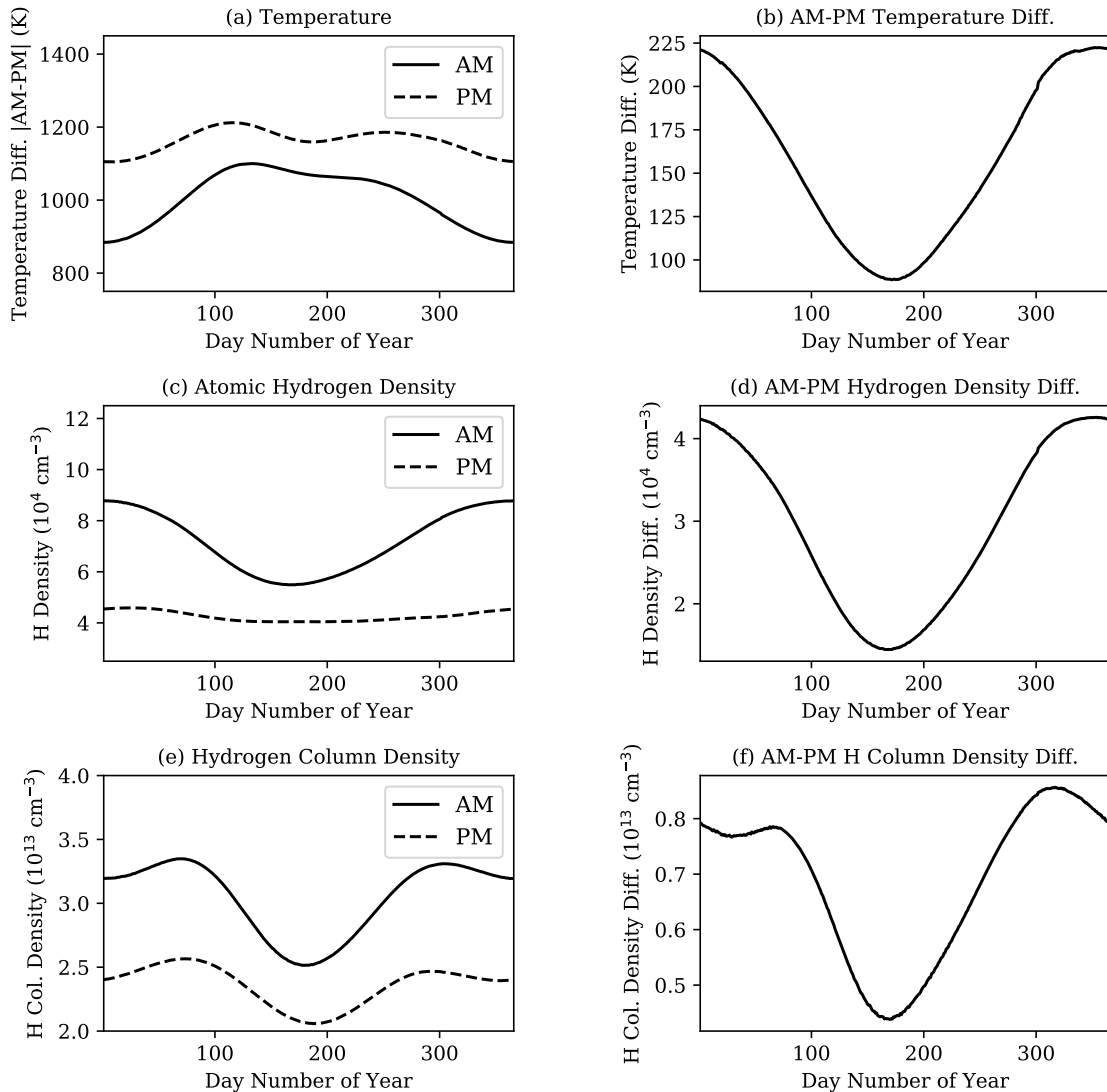


Figure 6.11: Within the radiative transport execution of the `lyao_rt` code, NRLMSISE-00 is called to generate the thermospheric background atmosphere that is then used to calculate the H- α source function. The top two left panels, (a) and (c), show the temperature and hydrogen density NRLMSISE-00 outputs at 494.0 km altitude for morning and evening times. The bottom left panel (e) is the hydrogen column density NRLMSISE-00 output. The right panels, (b), (d), and (f), are the absolute difference between morning and evening NRLMSISE-00 outputs.

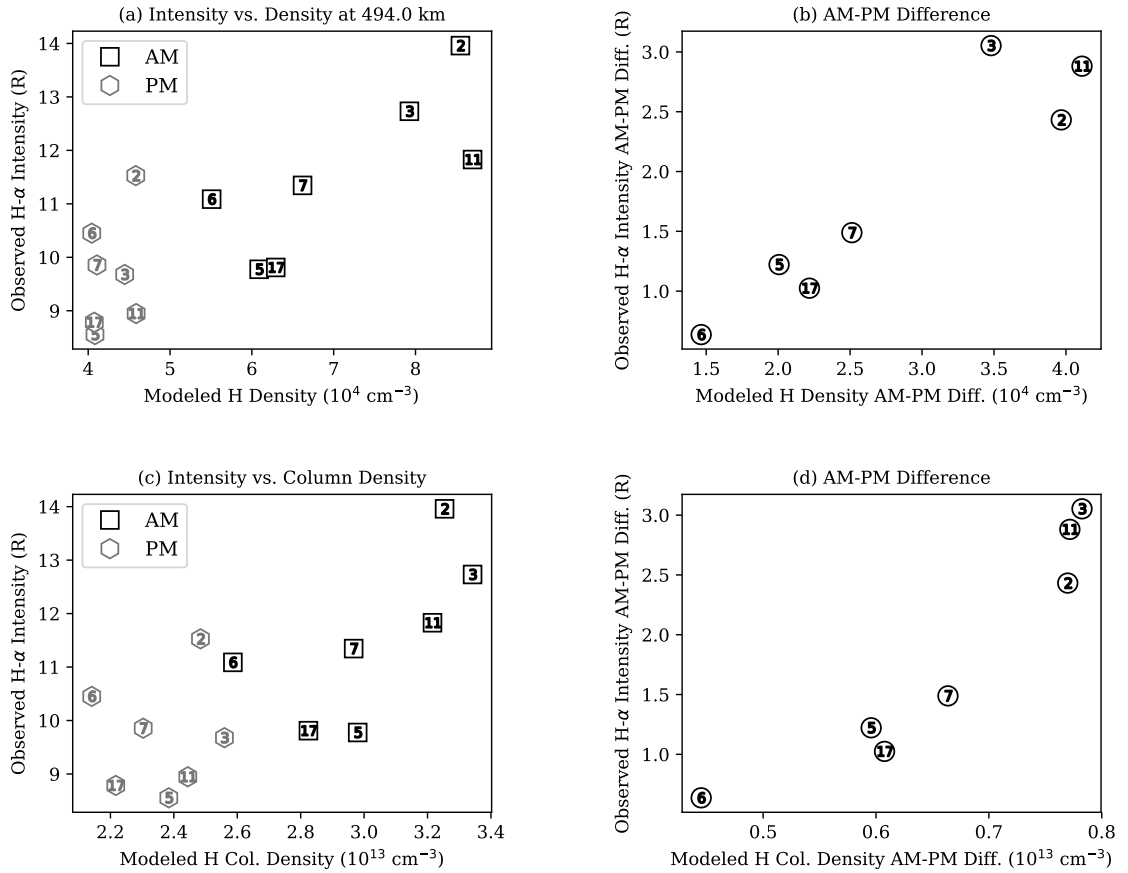


Figure 6.12: Although the predicted seasonal trend in H- α intensity is semi-annual, the observed intensity appears to fit an annual trend, similar to the hydrogen density seasonal trend. (a) The average intensity between 450-750 km shadow altitude for each observation is plotted against the hydrogen density at 494.0 km for the corresponding DOY. (b) Following the same scheme as (a), the diurnal intensity difference is plotted against the diurnal hydrogen density difference. (c) and (d) are the same as the above, but instead of hydrogen density at a particular altitude, intensity is plotted against hydrogen column density.

density, (c) and (d). The observed intensity is averaged between 400 and 800 km shadow altitude. The modeled hydrogen density at 494 km and hydrogen column density corresponds to the DOY of each observation. Figure 6.12 (a) depicts a positive slope in the morning correlation and very little variation in hydrogen density in the evening correlation, but Figure 6.12 (b) shows a clear correlation between the diurnal differences. Similarly, Figure 6.12 (c) depicts a lot of scatter in the absolute parameters, but (d) shows positive correlation in the diurnal differences.

Observed H-alpha intensities appear to be linearly correlated to `lyao_rt + NRLMSISE-00` exobase (494 km) hydrogen densities as well as the full (~ 100 to 60,000 km) hydrogen column density (Figure 6.12), indicating that low shadow altitude H-alpha observations are likely dominated by hydrogen signatures in the upper thermosphere and lower exosphere. Although H- α intensity falls off with altitude, the seasonal trend that is very prominent at low shadow altitudes is predicted to continue well into the exosphere (as seen in Figure 6.6). Exospheric hydrogen is highly coupled to the population of thermospheric hydrogen, and therefore, it is very important that our models of thermospheric hydrogen density accurately reflect our observations.

6.4 Recommendations

A major improvement to this study would involve collecting the same type of data over an extended period of time with the intent of filling in the seasonal gaps. It would also be interesting to repeat data collection at solar maximum and solar minimum to see the effects of solar cycle on hydrogen emission, but this would require consistent observing practices over decades of data collection. The above investigation into seasonal trends only adds to the need for a dedicated laboratory for geocoronal hydrogen studies. The INSpIRe observatory, with its remote operations and dual wavelength capabilities, will eventually fill that need.

6.4.1 Assessing Current Models

The model-data comparisons shown here indicate two discrepancies between observed Balmer- α intensities and models generated using MSIS as an input for radiative transport. There is an overall factor of ~ 2 difference between observed and predicted absolute intensities, and there is a disproportionately higher diurnal asymmetry than predicted for winter observations than for summer observations. The model for atomic hydrogen that comes from the MSIS series of models needs to be investigated further. Making the same model-data comparisons with data taken from the INSpIRE observatory will likely confirm the results of this study.

Repeating this study with a different atomic hydrogen and temperature input may provide different results; for example, one could do this with the Whole Atmosphere Community Climate Model eXtended (WACCM-X), which is a physics-based model instead of empirical. As mentioned in Chapter 1, the study done by *Qian et al.* [33] found that WACCM-X provided better agreement to TIMED/SABER hydrogen data than NRLMSISE-00. This is likely because WACCM-X accounts for a variety of climatological effects, whereas MSIS relies almost completely on diffusive equilibrium [33].

6.4.2 Interhemispheric Collaboration

The INSpIRE observatory is planned to deploy to a midlatitude Northern hemisphere location, where winter occurs near December and summer occurs near July. However, there exists another hydrogen FPI observatory in the Southern hemisphere that could take data simultaneously. The other observatory is called the Wisconsin Hydrogen-Alpha Mapper (WHAM), and its primary directive is to study galactic H- α emissions; in other words, terrestrial H- α is a noise source for WHAM [57]. The WHAM FPI is not as high resolution as the planned INSpIRE FPI, but it has a high enough resolution to pick out the terrestrial hydrogen line for noise removal [57]. WHAM is also capable of remote observations.

Model intensity predictions for conjugate latitude points at Kitt Peak National Observatory (KPNO) in Arizona and the Cerro Telolo Inter-American Observatory

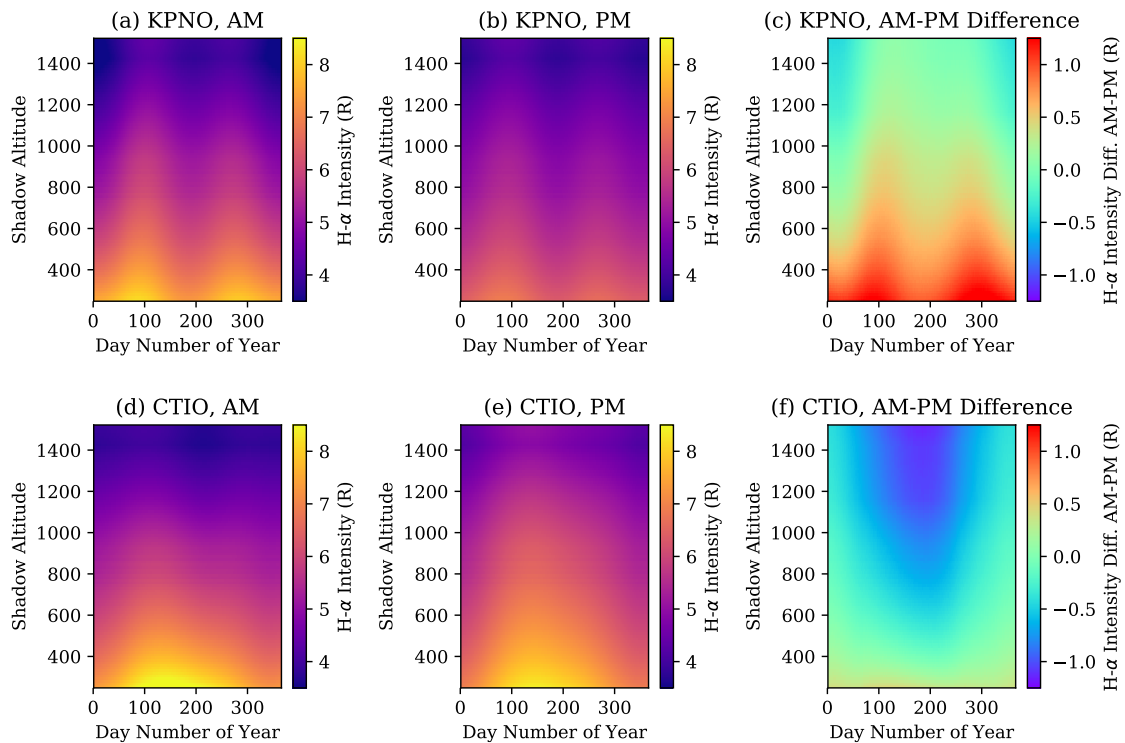


Figure 6.13: (a, b, c) The AM, PM, and diurnal difference in H- α emission intensity as modeled by `lyao_rt + NRLMSISE-00` at Kitt Peak National Observatory (KPNO), Arizona. (d, e, f) Same plots but modeled for an observer at Cerro Telolo Inter-American Observatory (CTIO) in Chile.

(CTIO) in Chile, the current site of WHAM, are shown in Figure 6.13. The seasonal variation in intensity at each of these locations is expected to be anti-correlated, due to the anti-correlation in temperature between the two hemispheres (e.g. winter occurs in December for the northern hemisphere and July for the southern hemisphere). In Figure 6.13, it is clear that the minimum in H- α intensity is predicted to occur in the summer hemisphere, and the maximum is predicted to occur in the winter hemisphere.

INSPIRe and WHAM could be used to take observations in parallel from conjugate latitudes, given that the remote site of the INSPIRe observatory in the northern hemisphere is similar to WHAM's in the southern hemisphere. This could provide data in support of spatial variations of hydrogen density over time.

Chapter 7

Conclusions

“Art is never finished, only abandoned.”

Leonard da Vinci,
Italian Polymath

7.1 Summary of Development

The Investigating Near Space Interaction Regions (INSpIRe) observatory has been provided with the building blocks for remote operations. For this thesis, the author has completed the following required objectives:

1. defined the requirements and testing procedures for remote operations of the INSpIRe observatory,
2. implemented control solutions for each the dome, Pressure Control System (PCS), SBIG detector, and Andor detector,
3. modified and documented the solutions of Jeff Percival for each the Environmental Sensor System (ESS) monitoring system and the Siderostat Control System (SCS),
4. developed key observing tools to assist in geocoronal hydrogen observations, including the cluster, scripting, and tuner tools,

5. accomplished automatic logging and power monitoring alerts,
6. executed the automatic recording of observing conditions and parameters to data file headers,
7. individually tested the desired functionality of each control and monitoring widget and observing tool, and
8. confirmed integration of PCS, Andor detector, and the aligned INSpIRE Fabry-Perot interferometer (FPI).

Because of the completion of these objectives, the INSpIRE observatory is now capable of remote operations.

The design and implementation of the INSpIRE control software has proven to be modular, as demonstrated by the scripting and tuning widgets, and scalable, as shown in the implementation of image display and header population shared by both detectors. This is important for future additions to the control software. The utilization of functional global variable cluster (FGVC) for each widget allows for easy access in the case that new instruments added in to the observatory need environmental or peripheral information from INSpIRE. It was of utmost importance to the author that good LabVIEW programming practices were followed, such as using code blocks and easily readable programming structures, to ensure that future students working on the INSpIRE observatory would be able to make additions with ease.

7.1.1 Future Expansions of Remote Operations

FPI alignment was initially delayed due to missing hardware (see Section 3.6.1), so full remote testing of the FPI is left for future work, although preliminary testing with a lamp light source has shown that the INSpIRE control software is capable of data collection while coupled to the FPI. Two conditions need to be met before full remote operations testing can begin: (1) several peripheral components need to be installed and integrated into remote operations procedures, and (2) the FPI needs to be fully aligned and tested in remote operations. The peripheral components (a robotic focuser, calibration lamps, and a filter wheel) are not any more complicated

than any of the components in this thesis and should not have any trouble integrating into remote operations. For minimal remote testing, the only active component that needs to be installed is a controllable calibration lamp; the focus and filter can be permanently set for a single wavelength (H- α , for example!).

Regarding future implementations, the ultimate goal of having two FPIs is an innovative solution to collecting dual-wavelength observations, and this observatory is in the unique circumstance of having access to more than one dual-etalon FPI (a single etalon pair can be quite expensive). When a second FPI is installed, the remote operations software will need to be scaled up or duplicated wherever the FPI needs its own components (e.g. PCS, detector, robotic focuser).

In the case of the spatial heterodyne spectrometer (SHS) that is already installed, the SHS operations software, which is maintained on a separate control computer, will need to be integrated with the INSpIRE Launchpad for environmental sensor readings. This will require setting up communications between the two systems, although grabbing data from INSpIRE should be made easier by the FGVC system.

7.2 Summary of Scientific Contributions: Achieved and Expected

The INSpIRE observatory is designed around the objective of answering questions about geocoronal science. The collection of long timeline datasets and eventually dual wavelength datasets will undoubtedly contribute to the current body of knowledge on neutral atomic hydrogen in our upper atmosphere. As part of this thesis, an original model-data comparison is presented between the *Mierkiewicz et al.* [39] FPI observations and radiative transport models generated using Lyman Atmospheric Observations Radiative Transport (lyao_rt) + NRLMSISE-00 [49]. Observed diurnal variation in H- α emission intensity exhibits an annual variation with the highest diurnal variation in winter and the lowest in summer. The model underestimates the diurnal variation in the winter by more than $\sim 2 R$, and that the modeled absolute H- α emission intensity is lower than observations by a factor of 2. Additionally, by using

data from the same instrument that will be installed in INSpIRe, it is made quite clear that the observatory will be capable of measuring the sometimes sub-rayleigh difference between morning and evening observations.

7.2.1 Recommended Data Collection Strategies for INSpIRe

Once the INSpIRe observatory is deployed and ready for remote operations, data collection can begin. As an initial observing campaign, the author suggests taking data on at least three nights per new moon period each month for a year, taking care to collect data at both dusk and dawn immediately after and before sunset at a high cadence over all three nights. The pointing of the siderostat should be as close to zenith as possible while also avoiding the galactic plane (where there are bright sources of galactic Balmer- α). Calibration images should be taken nightly, at the beginning, middle, and end of the night, as possible.

If the described observing pattern is repeated on a yearly basis for several years, a longterm dataset will be built up from the same geodetic latitude and longitude with the same instrumentation. Collecting a large amount of data throughout dusk and dawn will help in analyzing the diurnal variation over seasonal trends. At low shadow altitudes, the intensity changes quite rapidly, and so high cadence of data collection during this time period is necessary to get a good representation of the intensity curve. In order to study the effects of multiple scattering more closely, it would also be important to collect data through midnight.

The best possible data will be carefully tuned and well-documented. Fortunately, this is made more efficient by the INSpIRe control software. It is now easier than ever to complete a tuning procedure with the automated tuning widget. Observing notes that would normally need to be carefully recorded by hand are instead automatically recorded and stored with each image file. Additionally, it is highly recommended that the scripting tool be utilized for efficiency of repetitive measurements to minimize the inefficiencies of human observers late into the night (the author is particularly notorious for forgetting to hit the ‘Start Exposure’ button during manual observations).

Bibliography

- [1] J. E. Bishop, “Transport of Resonant Atomic Hydrogen Emissions in the Thermosphere and Geocorona: Model Description and Applications,” *Journal of Quantum Spectroscopy and Radiative Transfer*, vol. 61, no. 4, pp. 473–491, 1999.
- [2] E. Chaisson and S. McMillan, *Astronomy Today*. Pearson Education, Inc., 8 ed., 2014.
- [3] D. V. Kotov, P. G. Richards, V. Truhlik, O. V. Bogomaz, M. O. Shulha, N. Maruyama, M. Hairston, Y. Miyoshi, Y. Kasahara, A. Kumamoto, F. Tsuchiya, A. Matsuoka, I. Shinohara, M. Hernandez-Pajares, I. F. Domnin, T. G. Zhivolup, L. Y. Emelyanov, and Y. M. Chepurnyy, “Coincident Observations by the Kharkiv IS Radar and Ionosonde, DMSP and Arase (ERG) Satellites, and FLIP Model Simulations: Implications for the NRLMSISE-00 Hydrogen Density, Plasmasphere, and Ionosphere,” *Geophysical Research Letters*, vol. 0, no. 0, 2018.
- [4] D. V. Kotov, P. G. Richards, O. V. Bogomaz, L. F. Chernogor, V. Truhlik, L. Y. Emelyanov, Y. M. Chepurnyy, and I. F. Domnin, “The importance of neutral hydrogen for the maintenance of the midlatitude winter nighttime ionosphere: Evidence from IS observations at Kharkiv, Ukraine, and field line interhemispheric plasma model simulations,” *Journal of Geophysical Research: Space Physics*, vol. 121, no. 7, pp. 7013–7025, 2016.

- [5] I. A. Daglis, R. M. Thorne, W. Baumjohann, and S. Orsini, “The terrestrial ring current: Origin, formation, and decay,” *Reviews of Geophysics*, vol. 37, no. 4, pp. 407–438, 1999.
- [6] Y. Korenkov, V. Klimenko, V. Surotkin, F. Bessarab, N. Natsvalyan, and M. Forster, “Effect of the global neutral hydrogen distribution on the spatial structure and thermal balance in the upper ionosphere,” *Journal of Atmospheric and Solar-Terrestrial Physics*, vol. 59, no. 11, pp. 1311 – 1320, 1997.
- [7] J. W. Chamberlain, “Planetary coronae and atmospheric evaporation,” *Planetary and Space Science*, vol. 11, no. 8, pp. 901 – 960, 1963.
- [8] “U.S. Standard Atmosphere,” Oct 1976.
- [9] L. G. Jacchia, “Thermospheric Temperature, Density, and Composition: New Models,” *SAO Special Report*, vol. 375, Mar. 1977.
- [10] J. M. Picone, A. E. Hedin, D. P. Drob, and A. C. Aikin, “NRLMSISE-00 empirical model of the atmosphere: Statistical comparisons and scientific issues,” *Journal of Geophysical Research: Space Physics*, vol. 107, pp. SIA 15–1 – SIA 15–16, dec 2002.
- [11] J. W. Chamberlain and D. M. Hunten, *Theory of Planetary Atmospheres: An Introduction to Their Physics and Chemistry*. Academic Press, Inc., second ed., 1987.
- [12] A. E. Hedin, “A Revised thermospheric model based on mass spectrometer and incoherent scatter data: MSIS-83,” *Journal of Geophysical Research: Space Physics*, vol. 88, no. A12, pp. 10170–10188, 1983.
- [13] W. Stephens, “Mass Spectrometer,” sept 1952.
- [14] M. Rodriguez, N. Paschadlidis, S. Jones, E. Sittler, D. Chornay, P. Uribe, T. Cameron, and B. Nanan, “A Compact Ion and Neutral Mass Spectrometer for CubeSat/SmallSat Platforms.” Poster, 2014.

- [15] T. C. Winter and T. A. Chubb, "The determination of the profile of the night sky hydrogen Lyman alpha emission line," *Journal of Geophysical Research*, vol. 72, no. 17, pp. 4405–4414, 1967.
- [16] G. R. Carruthers and T. Page, "Apollo 16 far ultraviolet imagery of the polar auroras, tropical airglow belts, and general airglow," *Journal of Geophysical Research*, vol. 81, no. 4, pp. 483–496, 1976.
- [17] H. C. Brinton, L. R. Scott, M. W. Pharo, and J. T. Coulson, "The Bennett ion-mass spectrometer on Atmosphere Explorer-C and -E," *Radio Science*, vol. 8, no. 4, pp. 323–332, 1973.
- [18] H. C. Brinton, H. G. Mayr, and W. E. Potter, "Winter Bulge and Diurnal Variations in Hydrogen Inferred from AE-C Composition Measurements," *Geophysical Research Letters*, vol. 2, pp. 389–392, sep 1975.
- [19] E. L. Breig, W. B. Hanson, J. H. Hoffman, and D. C. Kayser, "In situ measurements of hydrogen concentration and flux between 160 and 300 km in the thermosphere," *Journal of Geophysical Research*, vol. 81, no. 16, pp. 2677–2686, 1976.
- [20] P. V. Sheglov, "Concentration of nightglow H α -emission to the ecliptic and the radial velocity of this line," *Nature*, vol. 199, p. 990, sep 1963.
- [21] B. Tinsley, "Initial results of geocoronal Balmer Alpha observations," *Planetary and Space Science*, vol. 15, no. 11, pp. 1757 – 1775, 1967.
- [22] B. A. Tinsley, "Temporal variations in geocoronal Balmer alpha," *Journal of Geophysical Research*, vol. 73, no. 13, pp. 4139–4149, 1968.
- [23] B. A. Tinsley, "Variations of Balmer alpha emission and related hydrogen distributions," *Space Res.*, vol. 10, pp. 582–590, 1970.
- [24] B. A. Tinsley, A. B. Christensen, J. Bittencourt, H. Gouveia, P. D. Angreji, and H. Takahashi, "Excitation of oxygen permitted line emissions in the tropical nightglow," *Journal of Geophysical Research*, vol. 78, no. 7, pp. 1174–1186, 1973.

- [25] B. A. Tinsley, R. R. Hodges, and D. F. Strobel, “Diurnal variations of atomic hydrogen: Observations and calculations,” *Journal of Geophysical Research*, vol. 80, no. 4, pp. 626–634, 1975.
- [26] P. Shih, F. L. Roesler, and F. Scherb, “Intensity variations of geocoronal Balmer alpha emission: 1. Observational results,” *Journal of Geophysical Research: Space Physics*, vol. 90, no. A1, pp. 477–490, 1985.
- [27] J. E. Bishop, J. Harlander, S. M. Nossal, and F. L. Roesler, “Analysis of Balmer α intensity measurements near solar minimum,” *Journal of Atmospheric and Solar-Terrestrial Physics*, vol. 63, pp. 341–353, 2001.
- [28] J. Harlander and F. Roesler, “Observations of geocoronal Balmer-alpha from Mt. Haleakala, Hawaii,” 1989. 1238.
- [29] A. E. Hedin, “MSIS-86 Thermospheric Model,” *Journal of Geophysical Research: Space Physics*, vol. 92, no. A5, pp. 4649–4662, 1987.
- [30] S. M. Nossal, E. J. Mierkiewicz, and F. L. Roesler, “Observed and modeled solar cycle variation in geocoronal hydrogen using NRLMSISE-00 thermosphere conditions and the Bishop analytic exosphere model,” *Journal of Geophysical Research*, vol. 117, no. A03311, 2012.
- [31] L. Waldrop and L. J. Paxton, “Lyman α airglow emission: Implications for atomic hydrogen geocorona variability with solar cycle,” *Journal of Geophysical Research: Space Physics*, vol. 118, pp. 5874–5890, 2013.
- [32] J. H. Zoennchen, U. Nass, H. J. Fahr, and G. J., “The response of the H geocorona between 3 and 8 R_e to geomagnetic disturbances studied using TWINS stereo Lyman- α data,” *Annales Geophysicae*, vol. 35, pp. 171–179, 2017.
- [33] L. Qian, A. G. Burns, S. S. Soloman, A. K. Smith, J. M. McInerney, L. A. Hunt, D. R. Marsh, H. Liu, M. G. Mlynczak, and F. M. Vitt, “Temporal Variability of Atomic Hydrogen From the Mesopause to the Upper Thermosphere,” *Journal of Geophysical Research: Space Physics*, jan 2018.

- [34] C. R. Englert, J. M. Harlander, J. T. Emmert, D. D. Babcock, and F. L. Roesler, "Initial ground-based thermospheric wind measurements using Doppler asymmetric spatial heterodyne spectroscopy (DASH)," *Opt. Express*, vol. 18, pp. 27416–27430, Dec 2010.
- [35] J. M. Harlander, C. R. Englert, D. D. Babcock, and F. L. Roesler, "Design and laboratory tests of a Doppler Asymmetric Spatial Heterodyne (DASH) interferometer for upper atmospheric wind and temperature observations," *Opt. Express*, vol. 18, pp. 26430–26440, Dec 2010.
- [36] R. J. Oliverson, N. Doane, F. Scherb, W. M. Harris, and J. P. Morgenthaler, "Measurements of [C I] Emission from Comet Hale-Bopp," *The Astrophysical Journal*, vol. 581, pp. 770–775, Dec. 2002.
- [37] D. C. P. Kurupparatchi, E. J. Mierkiewicz, R. J. Oliverson, M. Sarantos, N. J. Derr, M. A. Gallant, S. A. Rosborough, C. W. Freer, L. C. Spalsbury, D. D. Gardner, O. L. Lupie, and F. L. Roesler, "High-Resolution, Ground-Based Observations of the Lunar Sodium Exosphere During the Lunar Atmosphere and Dust Environment Explorer (LADEE) Mission," *Journal of Geophysical Research: Planets*, vol. 123, no. 9, pp. 2430–2444, 2018.
- [38] E. J. Mierkiewicz, F. L. Roesler, , S. M. Nossal, and R. J. Reynolds, "Geocoronal hydrogen studies using Fabry-Perot interferometers, part 1: Instrumentation, observations, and analysis," *Journal of Atmospheric and Solar Terrestrial Physics*, vol. 68, pp. 1520–1552, 2006.
- [39] E. J. Mierkiewicz, F. L. Roesler, and S. M. Nossal, "Observed seasonal variations in exospheric effective temperatures," *Journal of Geophysical Research*, vol. 117, no. A06313, 2012.
- [40] M. M. Coakley, F. L. Roesler, R. J. Reynolds, and S. M. Nossal, "Fabry Perot CCD annular-summing spectroscopy: study and implementation for aeronomy applications," *Applied Optics*, vol. 35, pp. 6479–6493, nov 1996.

- [41] F. L. Roesler, “Fabry-Perot Instruments for Astronomy,” in *Methods of Experimental Physics: Astrophysics*, vol. 12, ch. 12, New York: Academic Press, second ed., 1974.
- [42] C. Fabry and A. Perot, “On a new form of interferometer,” *The Astrophysical Journal*, vol. 13, p. 265, 1901.
- [43] T. N. Olney, N. Cann, G. Cooper, and C. Brion, “Absolute scale determination for photoabsorption spectra and the calculation of molecular properties using dipole sum-rules,” *Chemical Physics*, vol. 223, no. 1, pp. 59 – 98, 1997.
- [44] E. R. Peck and B. N. Khanna, “Dispersion of Nitrogen,” *J. Opt. Soc. Am.*, vol. 56, pp. 1059–1063, Aug 1966.
- [45] R. Kallio., “Recommissioning REDDI: Reviving a Doppler Asymmetric Spatial Heterodyne Spectrometer for Observing Thermospheric Winds,” Master’s thesis, Embry-Riddle Aeronautical University, 2018.
- [46] S. M. Nossal, F. L. Roesler, M. M. Coakley, and R. J. Reynolds, “Geocoronal hydrogen Balmer- α line profiles obtained using Fabry-Perot annular summing spectroscopy: Effective temperature results,” *Journal of Geophysical Research*, vol. 102, pp. 14541–14553, jul 1997.
- [47] S. M. Nossal, F. L. Roesler, and M. M. Coakley, “Cascade excitation in the geocoronal hydrogen Balmer α line,” *Journal of Geophysical Research*, vol. 103, pp. 381–390, jan 1998.
- [48] E. J. Mierkiewicz, F. L. Roesler, J. E. Bishop, and S. M. Nossal, “Systematic program for ground-based Fabry-Perot observations of the neutral hydrogen exosphere,” *Proc. SPIE*, vol. 3756, pp. 323–336, 1999.
- [49] M. A. Gallant, E. J. Mierkiewicz, A. R. Zacharias, S. A. Nossal, L. Qian, and A. G. Burns, “Signatures of thermospheric-exospheric coupling of hydrogen in observed seasonal trends of Balmer-alpha intensity,” *Journal of Geophysical Research: Space Physics*, 2018.

- [50] J. E. Bishop, E. J. Mierkiewicz, F. L. Roesler, J. F. Gomez, and C. Morales, “Data-model comparison search analysis of coincident PBO Balmer α , EURD Lyman β geocoronal measurements from March 2000,” *Journal of Geophysical Research: Space Physics*, vol. 109, no. A5, 2004. A05307.
- [51] J. Bishop, “Analytic exosphere models for geocoronal applications,” *Planetary and Space Science*, vol. 39, no. 6, pp. 885 – 893, 1991.
- [52] D. E. Anderson, R. R. Meier, R. R. Hodges, and B. A. Tinsley, “Hydrogen Balmer Alpha Intensity Distributions and Line Profiles From Multiple Scattering Theory Using Realistic Geocoronal Models,” *Journal of Geophysical Research*, vol. 92, pp. 7619–7642, jul 1987.
- [53] A. O. Nier, W. E. Potter, and D. C. Kayser, “Atomic and molecular oxygen densities in the lower thermosphere,” *Journal of Geophysical Research*, vol. 81, no. 1, pp. 17–24, 1976.
- [54] A. E. Hedin, “Extension of the MSIS Thermosphere Model into the middle and lower atmosphere,” *Journal of Geophysical Research: Space Physics*, vol. 96, no. A2, pp. 1159–1172, 1991.
- [55] A. G. Burns, T. L. Killeen, and R. G. Roble, “Processes responsible for the compositional structure of the thermosphere,” *Journal of Geophysical Research: Space Physics*, vol. 94, no. A4, pp. 3670–3686, 1989.
- [56] A. G. Burns, S. C. Solomon, W. Wang, L. Qian, Y. Zhang, L. J. Paxton, X. Yue, J. P. Thayer, and H. L. Liu, “Explaining solar cycle effects on composition as it relates to the winter anomaly,” *Journal of Geophysical Research: Space Physics*, vol. 120, no. 7, pp. 5890–5898, 2015.
- [57] L. M. Haffner, R. J. Reynolds, S. L. Tufte, G. J. Madsen, K. P. Jaehnig, and J. W. Percival, “The Wisconsin H α Mapper Northern Sky Survey,” *Astrophys. J.*, vol. 149, pp. 405–422, Dec. 2003.

Appendix A

Requirements for Remote Operations

1. Fundamental INSpIRe Observatory Requirements

- 1.1. INSpIRe (Investigating Near Space Interaction Regions) shall work as a locally and remotely operable observing platform.
 - 1.1.1. The INSpIRe observatory shall allow users to access all available sensor readouts when under remote control.
 - 1.1.2. All of the remotely operable features of the INSpIRe observatory shall be remotely accessible via the centralized control computer(s).
 - 1.1.3. All of the remotely operable features shall also be accessible when under local control via the centralized control computer(s).
- 1.2. INSpIRe shall be deployed to a dark, clear-sky location after remote operations are developed.
 - 1.2.1. The INSpIRe observatory will be a customized shipping container for ease of deployment.
 - 1.2.2. The location will allow for remote connection via the internet.
- 1.3. INSpIRe shall provide shelter from weather for any instruments housed within.
 - 1.3.1. A motor-controlled dome will allow full sky access to the siderostat when fully open, and full coverage when fully closed.

- 1.3.2. Two clear immoveable domes will allow access to outside light for smaller optics.
- 1.3.3. Temperature, humidity, and wind sensors will be placed indoors and outdoors throughout the observatory and used as indicators of unsafe observing weather.
- 1.4. INSpIRe shall house at least one remotely operable, pressure-tuned Fabry-Perot Interferometer (FPI) that is capable of acquiring Balmer series intensity observations.
 - 1.4.1. Each FPI will be mounted in a stationary configuration.
 - 1.4.2. Each FPI will have the ability to couple to the same fully steerable siderostat to collect light from sky targets.
 - 1.4.3. Each FPI will be coupled to a Charge-Coupled Device (CCD) detector for image acquisition.
 - 1.4.4. Each FPI pressure chamber will be controlled via a UW-Madison Pressure Control System (PCS).
 - 1.4.5. Each FPI will have the ability to couple to the same calibration lamp suite that is appropriate for Balmer- α intensity observations.
 - 1.4.6. Each FPI will couple to a filter wheel that is appropriate for Balmer- α intensity observations.
2. INSpIRe Launchpad Requirements
 - 2.1. The INSpIRe Launchpad will allow the user to run any subsystem widget or open the window of a subsystem widget in the hidden state.
 - i. A boolean indicator shall display whether each subsystem widget is running or not.
 - 2.2. While running, the INSpIRe Launchpad will record available FGVC sensor data to a log file.
 - 2.2.1. All available sensor data shall be recorded at regular intervals not to exceed 10 minutes between recordings.

- 2.2.2. A new log file will be generated every 24 hours.
- 2.2.3. Sensor data shall be recorded to the appropriate 24-hour log file for the corresponding UT time and date.
- 2.3. The INSpIRE Launchpad will generate and distribute 24-hour plots of sensor data nightly.
 - 2.3.1. The plots shall include all environmental sensor data and pressure values from any FPI Pressure Control System(s).
 - 2.3.2. The plots shall be generated as a PDF, not to exceed three pages.
 - 2.3.3. The plots PDF shall be distributed via email.
- 2.4. The INSpIRE Launchpad will monitor and display the status of the Uninterruptible Power Supply (UPS).
 - 2.4.1. The UPS shall be monitored for battery status at regular intervals, not to exceed 2 minutes between readings.
 - 2.4.2. A boolean indicator shall display whether the UPS has gone on battery.
 - 2.4.3. Whenever the UPS switches to battery during a power outage, the INSpIRE Launchpad shall immediately distribute an alert email.
 - 2.4.4. Whenever the UPS switches back to normal after a power outage, the INSpIRE Launchpad shall immediately distribute an alert email.
- 2.5. The INSpIRE Launchpad will have the ability to force all running subsystems to run their shutdown procedure sequentially, also known as observatory shutdown.
 - 2.5.1. The INSpIRE Launchpad shall have an EXIT button accessible to the user that runs observatory shutdown.
 - 2.5.2. Observatory shutdown shall attempt to occur if the user tries to close the INSpIRE Launchpad window.
 - 2.5.3. Any shutdown attempt shall trigger a warning dialog box that informs the user of what the shutdown procedure entails for the entire observatory and allows the user to cancel shutdown.

3. General Widget Requirements

- 3.1. If applicable, running a widget will initialize any associated hardware and begin available sensor monitoring and display.
- 3.2. Multiple widgets will be able to run simultaneously.
- 3.3. No two widgets will communicate with the same hardware simultaneously.
- 3.4. In its running state, each widget shall save all of its hardware's available sensor data to its own FGVC at regular intervals, not to exceed the interval used in recording data to the daily log file.
- 3.5. Widgets will be able to run in hidden states to take up less monitor space.
 - 3.5.1. While in a hidden state, the widget will continue to run as it normally would without user interaction.
- 3.6. Each widget shall have an EXIT button that runs their respective shutdown procedure.
 - 3.6.1. Any widget shutdown attempt may trigger a warning dialog box that informs the user of what the shutdown procedure entails and allows the user to cancel shutdown.

4. Detector Control Requirements

- 4.1. Detector sensor monitoring shall include temperature and filter information when available, as well as whether or not the camera is currently exposing.
- 4.2. Detector data output to the Detector FGVC will also include current settings for exposure time, image type, image size and binning, gain, and focal distance.
- 4.3. There may be multiple widgets and multiple FGVCs for different detectors.
- 4.4. Each Detector widget shall allow the user to take images one-at-a-time, in series, or in a continuous mode.

- 4.5. Each Detector widget shall allow the user to take object, bias or dark frames.
 - 4.6. Each Detector widget shall allow the user to adjust the exposure time, readout rates, and image size, as available.
 - 4.7. Each Detector widget shall allow the user to adjust the camera temperature as available.
 - 4.8. Each Detector widget shall allow the user to adjust the filter wheel as available.
 - 4.9. Each Detector widget shall display any images taken.
 - 4.10. Each Detector widget shall allow the user to change display settings for displayed images.
 - 4.11. Each Detector widget shall allow the user to save the image as a FITS file.
 - 4.12. Each Detector widget shall automatically update the FITS file header with sensor data from the functional global variable clusters for each relevant subsystem widget.
5. Environmental Sensor System (ESS) Requirements
 - 5.1. ESS sensor monitoring shall include internal and external temperature and humidity, wind speed and direction, internal barometric pressure, and siderostat voltage values.
 - 5.2. The ESS widget shall allow the user to adjust the sensor readout rate.
 - 5.3. The ESS widget shall display all temperature, humidity, wind, and pressure information.
6. Siderostat Control System (SCS) Requirements
 - 6.1. SCS sensor monitoring shall include current motor position in voltage units.

- 6.2. SCS sensor data output to the SCS Cluster shall include calculations of current motor position in the following astronomical reference frames: altitude and azimuth, right ascension and declination, galactic latitude and longitude, and target azimuth, target zenith distance, and target hour angle.
- 6.3. SCS sensor data output to the SCS Cluster shall also include several calculations that are useful for atmospheric observations: solar azimuth, solar zenith distance, shadow distance, shadow altitude and VLSR.
- 6.4. The SCS widget controls shall include individual motion in each the altitude and azimuth axis, slewing to targets using both axes simultaneously, and target tracking.
- 6.5. The SCS widget shall display all SCS sensor data and required calculations as in 6.1., 6.2., and 6.3.

7. Dome Control Requirements

- 7.1. Dome sensor monitoring shall consist of the current dome position as available from the dome serial communication port.
- 7.2. The Dome Control widget shall allow the user to open or close the dome completely or partially.
- 7.3. The Dome Control widget shall include a “Pre-Open” function which opens the dome by its smallest increment.
- 7.4. The Dome Control widget shall display the current dome position as available from the dome serial communication port.
- 7.5. The Dome Control widget shall display whether the dome is in motion or not.

8. Pressure Control System (PCS) Requirements

- 8.1. PCS sensor monitoring shall include all available data in the status return packet from the PCS serial communication port.

- 8.2. The PCS widget shall allow the user to open or close the pressure control loop and change the target pressure for each pressure chamber.
- 8.3. The PCS widget shall display all available PCS sensor data.
- 8.4. The PCS widget may allow the user to turn on the vacuum pump.
- 8.5. The PCS widget may allow the user to open a valve to the vacuum pump.
- 8.6. the PCS widget may allow the user to open a valve to the gas tank.

9. Scripting Requirements

- 9.1. The Scripting widget shall allow the user to create and run user-made scripts that specify sequential actions for different INSpIRE subsystems.
- 9.2. The Scripting widget shall allow the user to save a script to a text file.
- 9.3. The Scripting widget shall allow the user load a script from a pre-made text file.
- 9.4. The Scripting widget shall allow the user to pause a running script.
- 9.5. The Scripting widget shall allow the user to edit, remove actions from, or move actions up or down in a newly loaded or paused script.
- 9.6. The Scripting widget shall display the sequential list of actions and their parameters for a given script.
- 9.7. The Scripting widget shall indicate whether an action has been run or not.
- 9.8. The Scripting widget shall indicate when an action encounters an error.

Appendix B

Test Actions

Test Actions 1. Launchpad

<i>Test</i>	<i>Action</i>	<i>Result</i>
UPS	Press Test button on UPS	UPS indicator changes from normal to on backup Emergency alert email distribution
Exit	Press EXIT on Launchpad	Each running VI stows sequentially Launchpad stops running
Stow	Press Stow on Launchpad	Each running VI stows sequentially
Open Widget	Open all widgets individually	Each widget front panel opens Each widget runs automatically Each hardware control widget initializes hardware automatically
DS9	Run DS9	Open DS9 program
Logging	Run at 120 sec intervals	Log file is populated with data from 120 second intervals

Test Actions 1. Launchpad (Continued)

<i>Test</i>	<i>Action</i>	<i>Result</i>
		Countdown/loading bar updates appropriately
	Run through midnight	Log file is plotted and distributed via email

Test Actions 2. Environmental Sensor Monitoring

<i>Test</i>	<i>Action</i>	<i>Result</i>
Home Tab	Run at 30 sec intervals	Countdown/loading bar updates appropriately Graphs on Temp, Humidity, Weather tabs update appropriately
Stow	Press Stow on ESS	Shut down ESS monitor Close front panel

Test Actions 3. Dome Control

<i>Test</i>	<i>Action</i>	<i>Result</i>
Indicators	During motion	Appropriate Leaf motion light turns on for each above action
	After motion	Appropriate image appears on front panel after each above action
Full Dome Ctrl	Press Pre-Open	Dome moves one increment (about 3 inches, west half)
	Press Open	Both halves of dome open (first west, then east)
	Press Close	Both halves of dome close (first east, then west)

Test Actions 3. Dome Control (Continued)

<i>Test</i>	<i>Action</i>	<i>Result</i>
Handpaddle	Press & hold	West moves towards closed for button hold
	West Close	
	Press & hold	West moves towards open for button hold
	West Open	
	Press & hold	East moves towards closed for button hold
	East Close	
	Press & hold	East moves towards open for button hold
	East Open	
Manual Leaf Ctrl	Close to Limit	Moves E or W to closed
	Close Partially	Move E or W towards closed for given time
	Open Partially	Move E or W toward open for given time
	Open to Limit	Moves E or W to open
Stow	Press Stow	Disconnect serial connection
		Shutdown Dome widget
		Close front panel

Test Actions 4. Pressure Control

<i>Test</i>	<i>Action</i>	<i>Result</i>
Indicators	As often as possible	Update status panel, plot panel
	Show Pressure Plot	Changes status panel to plot panel
	Show Indicators	Changles plot panel to status panel
Startup	Run Startup	Popup, (If user chooses) Run intialization sequence
Close Loops	Close Loops A/B	A closes loop, B closes loop, status reflects this
	Close Loop A	A closes loop, status reflects this

Test Actions 4. Pressure Control (Continued)

<i>Test</i>	<i>Action</i>	<i>Result</i>
	Close Loop B	B closes loop, status reflects this
Open Loops	Open Loops A/B	A opens loop, B opens loop, status reflects this
	Open Loop A	A opens loop, status reflects this
	Open Loop B	B opens loop, status reflects this
Change Press	Change Press A/B	Popup, (if user chooses) A changes, wait, B changes, wait, status reflects this
	Change Press A	Popup, (if user chooses) A changes, wait, status reflects this
	Change Press B	Popup, (if user chooses) B changes, wait, status reflects this
Inc CHB	Inc CHB by X	Change B pressure by X, wait, status reflects this
	Set Inc	Popup, (if user chooses) change inc value
Ctrl Src	Change Ctrl Source	Popup, (if user chooses) change control source, status reflect this
Stow	Stow PCS	Disconnects user commands, continues to update status
Stow & Exit	Stow & Exit PCS	Disconnects user commands, shutdown PCS widget, close front panel

Test Actions 5. Siderostat Control

<i>Test</i>	<i>Action</i>	<i>Result</i>
Indicators	As often as possible	Update time, RA/Dec, Shadow Code output
	During Motion	Update Motor position, RA/Dec, Alt/Az, Shadow Code output

Test Actions 5. Siderostat Control (Continued)

<i>Test</i>	<i>Action</i>	<i>Result</i>
Target RA/Dec	New Target or Offset	Update Target RA/Dec, Az/El
Target Az/El	New Target or Offset	Update Mount Command Az/El
Manual Control	Handpaddle	Move in appropriate direction at selected speed
	Home	Move axis to appropriate home position
	Stow	Move axis to appropriate stow position
Control Source	Set to None	Only manual motion allowed
	Set to Mount	Immediately move to Mount Command Az/El
	Set to Target	Immediately move to Target Command Az/El
STOP	Press STOP sign button	Immediately stop motion indefinitely
	Release the STOP	Allow motion after a stop
Quit	Press Quit	Shutdown SCS widget, close front panel

Test Actions 6. SBIG Camera Control

<i>Test</i>	<i>Action</i>	<i>Result</i>
Indicators	As often as possible	Update FW Status, Cooling status
	During Exposure	Update exposure loading bar
	During Action	Change "Ready" to "Busy"
Cooling	Set Cooling	Popup, (if user chooses) turn on/off cooling, change setpoint
Filter Wheel	Change Filters	Popup, (if user chooses) change filter

Test Actions 6. SBIG Camera Control (Continued)

<i>Test</i>	<i>Action</i>	<i>Result</i>
	(Popup) Choose filter	Show vendor-provided transmission curve
Data Collection	Grab Image	Popup, (if user chooses) take single image with given setting, display as desired
	Grab Image With Autosave	Same as above, save after
	Grab Series	Popup, (if user chooses) take image series with given setting, display as desired, save
	Focus Mode OFF -> ON	Popup, (if user chooses) begin taking focus images, display as taken
	Focus Mode ON -> OFF	Stop taking focus images
	Finder Mode OFF -> ON	Popup, (if user chooses) begin taking finder images, display as taken, save
	Finder Mode ON -> OFF	Stop taking finder images
File Options	Set-up Autosave	Popup, (if user chooses) set autosave settings
	Display header	(if user chooses image), display header of FITS file
	Open image in LV	(if user chooses image), display image in LabVIEW popup
	Open image in DS9	(if user chooses image), display image in DS9 window
Exit	Press Exit VI	Popup, (if user chooses) turn off cooling, disconnect camera, shutdown widget, close front panel

Test Actions 7. Andor Camera Control

<i>Test</i>	<i>Action</i>	<i>Result</i>
Indicators	As often as possible	Update cooling status, autosave status
	During Exposure	Update exposure loading bar and boolean
	During Readout	Update readout boolean
	During Action	Change “Ready” to “Busy”
Cooling	Set Cooling	Popup, (if user chooses) turn on/off cooling, change setpoint
Data Collection	Exposure Settings	Popup, (if user chooses) update exposure settings cluster Updated settings will reflect in subsequent presses of the settings button
	Take Exposure	Take exposure(s) as specified by exposure settings
File Options	Set-up Autosave	Popup, (if user chooses) set autosave settings
Exit	Press Exit VI	Popup, (if user chooses) turn off cooling, disconnect camera, shutdown widget, close front panel

Test Actions 8. Image Display

<i>Test</i>	<i>Action</i>	<i>Result</i>
Indicators	At runtime	Most recent exposure or selected image should appear
	Cursor motion over image	Update x,y,count indicator
Image Options	Save Image as...	(if user chooses), save image as user choice
	Display Options	Popup, (if user chooses) set display options

Test Actions 8. Image Display (Continued)

<i>Test</i>	<i>Action</i>	<i>Result</i>
	Display header	(if user chooses image), display header of FITS file
	Open image in DS9	(if user chooses image), display image in DS9 window
Exit	Close window	Popup, (if user chooses), shutdown widget, close front panel

Test Actions 9. Cluster Display

<i>Test</i>	<i>Action</i>	<i>Result</i>
Indicators	As often as FGVCs are updated	Update FGVC information for each widget
Time Stamps	No update for 60 sec	Outline timestamp in red
Exit	Press Exit VI	Shutdown widget, close front panel

Test Actions 10. Scripting Tool

<i>Test</i>	<i>Action</i>	<i>Result</i>
Indicators	If script loaded/created	Display script
	If script edited	Update script display
	If script is running	Light up actions that have occurred on the script display
	If error on specific action	Popup, show error indicator on action
Add new action	Choose subsystem	Change action drop-down box to appropriate subsystem

Test Actions 10. Scripting Tool (Continued)

<i>Test</i>	<i>Action</i>	<i>Result</i>
	Choose action	Show action parameters
	Add action	Add action and parameters to bottom of script display
Script	Delete an action	Remove action from script display
	Move action up/down	Switch action with the above or below action in script display
	Move action up/down at limit	Action does not change position
	Clear Script	Popup, (if user chooses) Remove all actions from script display
	Save Script	(if user chooses) Save all actions in order from script display to a text file
	Load Script	Popup, (if user chooses) Remove all actions from script display, replace with actions from text file
	Run Script	Start running the script in the script display from the beginning, disables “Run Script” button
	Pause	Stops a currently running script at the most recent action
	Resume	Resumes a paused script
	Reset Script	Restarts the script at the beginning of the script display, clears errors and “already-run” indicators, does not run the script
Exit	Exit VI	If script isn’t running, popup, (if user chooses) shutdown widget, close front panel

Test Actions 11. Tuning Tool

<i>Test</i>	<i>Action</i>	<i>Result</i>
Indicators	At runtime	Most recent tune settings shown
	Change tune configuration	Displayed tune settings will change to match tune configuration
Tune	Take Tune Data	Set up pressure on PCS, take number of exposures on Andor, save exposures to specified directory, all according to tune settings
	Analyze Tune Data	Ring sum each image in specified directory that matches tune settings, fit Gaussian to each, calculated FWHM and peak intensity for each, display popup of each spectra and Gaussian fit, display calculation of FWHM and peak intensity
	Full Tune	The result of Take Tune Data, followed by the result of Analyze Tune Data
	Take Tune Data with bad directory	Popup, back to idle
	Take Tune Data with PCS open loops	Popup, back to idle
	Take Tune Data with Andor disconnected	Popup, back to idle
	Abort	Cancel any running exposures and back to idle
Ringsum Viewer	At runtime	Popup display of last five spectra and Gaussian fits

Test Actions 11. Tuning Tool (Continued)

<i>Test</i>	<i>Action</i>	<i>Result</i>
	Show Gauss Fit	If on, display each Gaussian fit; if off do not display any Gaussian fits
Close	Close popup	
Tune Settings	At runtime	Most recent tune settings shown
	Change tune configuration	Displayed tune settings will change to match tune configuration
	Save Settings	Settings are written to a configuration file and updated on the main Tuner VI
	Close	Close popup
Ringsum Settings	At runtime	Most recent ringsum settings shown
	Save Settings	Settings are written to a configuration file
	Close	Close popup
Ring Center Tool	At runtime	No image displayed
	Choose image file	Image displayed with guide circle centered at center pixel of image
	X-Center, Y-Center up/down	Move guide circle center in appropriate direction
	Radius up/down	Change radius of guide circle
	Auto-Center	Runs computer vision algo to find center, moves guide circle center to best guess
	Refine Center for Tuning	Runs search algo using current X/Y-Center and displays best guess below image
	Adjust Tune Settings	Opens Tune Settings dialog
	Close	Close popup
Gauss Fit Tool	At runtime	No spectra displayed

Test Actions 11. Tuning Tool (Continued)

<i>Test</i>	<i>Action</i>	<i>Result</i>
	Choose image	Run ringsum and Gaussian fit algo and display spectra and fit on chart
	Move cursor	Low/High indicators reflect cursor movement in bin number space
	Low/High up/down	Cursor reflects Low/High indicators in bin number space
	Re-fit	Runs gauss fit on spectra using Low/High bin numbers
	Adjust Tune Settings	Opens Tune Settings dialog
	Close	Close popup
Exit	Exit VI	Shutdown widget, close front panel

Appendix C

Sample Header (FIRSTLIGHT.fits)

```
SIMPLE = T / file does conform to FITS standard
BITPIX = 32 / number of bits per data pixel
NAXIS = 2 / number of data axes
NAXIS1 = 3325 / length of data axis
NAXIS2 = 2503 / length of data axis
EXTEND = T / FITS dataset may contain extensions
COMMENT *****
COMMENT GENERAL INFORMATION
COMMENT *****
FILENAME= 'FIRSTLIGHT.fits'
FILETYPE= 'fits '
DATE = '2017-03-08 00:34:33' / file creation date (UTC)
ORIGIN = 'INSpIRe '
TELESCOP= 'INSpIRe '
INSTRUME= 'INSpIRe '
OBSERVER= 'INSpIRe '
COMMENT *****
COMMENT SCS PARAMETERS
COMMENT *****
DATE-OBS= '2017-03-08 00:33:52.4' / Observation date and time (UTC)
```

TIME-OBS= '00:33:52.4' / Observation time (UTC)
 LDAT-OBS= '2017-03-07 19:33:52.4' / Local observation date and time
 LTIM-OBS= '19:33:52.4' / Local observation time
 LAST-OBS= '06:13:17.3' / Local Apparent Sidereal Time
 GMST-OBS= '11:37:29.3' / Greenwich Mean Sidereal Time
 OBS-LON = -81.0483 / [deg E] Observatory longitude
 OBS-LAT = 29.1882 / [deg N] Observatory latitude
 OBS-ALT = 0. / [m] Observatory altitude
 RA = 7.45618 / [hr] Right Ascension
 DEC = 18.14786 / [deg] Declination
 AZ = -61.28 / [deg] Topocentric Azimuth
 EL = 110.405 / [deg] Topocentric Elevation
 GAL-LAT = 13.35654 / [hr] Galactic longitude
 GAL-LON = 15.90986 / [deg] Galactic latitude
 TARGETAZ= 118.7 / [deg] Target Azimuth
 TARGETZD= 20.4 / [deg] Target Zenith Distance
 TARGETHA= 22.74902 / [hr] Target Hour Angle
 SUN-AZ = -87.1 / [deg] Sun Azimuth
 SUN-ZD = 105.2 / [deg] Sun Zenith Distance
 AZ-DIFF = 154.2 / [deg] Azimuth Difference
 SHDIST = 401.336 / [km] Shadow Distance
 SHHEIGHT= 372.722 / [km] Shadow Height
 VLRSR = 36.9496 / [km/s] Geocentric velocity of the LSR
 COMMENT *****
 COMMENT CAMERA PARAMETERS
 COMMENT *****
 CAMERA = 'STF Camera' / Camera Name
 FOC-LEN = 180 / [mm] Focal length
 GAIN = 2000 / [e/ADU] Amplifier gain
 EXPTYPE = 'Object' / Exposure Type
 SERIES = ' ' / Series _ out of _

EXPTIME = 0.12 / [s] Length of Exposure
 FIRSTCOL= 0 / [pixel] First column of CCD to readout
 FIRSTROW= 0 / [pixel] First row of CCD to readout
 XBINNING= 1 / [pixel] X-axis binning factor
 YBINNING= 1 / [pixel] Y-axis binning factor
 XPIXSIZE= 9 / [micron] X-axis pixel size
 YPIXSIZE= 9 / [micron] Y-axis pixel size
 FNAME = 'SII ' / Filter Name
 FIDN = 2459432 / Filter Identification Number
 FCENTER = 6724. / [Ang] Filter Center wavelength
 CCDTEMP = 9.781 / [deg C] CCD temperature
 COMMENT *****
 COMMENT ESS PARAMETERS
 COMMENT *****
 DATE-ESS= '2017-03-08 00:33:08' / ESS sample date and time (UTC)
 TEMP01 = 21.75 / [deg C] Outside temperature
 TEMP02 = 23.28 / [deg C] Dome temperature
 TEMP03 = 23.34 / [deg C] Siderostat temperature
 TEMP04 = 24.26 / [deg C] Instrument room temperature
 TEMP05 = 23.21 / [deg C] Control room temperature
 TEMP06 = 35.26 / [deg C] AC air temperature
 TEMP07 = 37.83 / [deg C] Altitude motor temperature
 TEMP08 = 30.22 / [deg C] Azimuth motor temperature
 TEMP09 = 28.64 / [deg C] Lower cabinet temperature
 TEMP10 = 12.07 / [deg C] Upper cabinet temperature
 HUMID01 = 77.07 / [%] Outside relative humidity
 HUMID02 = 77.44 / [%] Dome relative humidity
 HUMID03 = 75.34 / [%] Siderostat relative humidity
 HUMID04 = 46.17 / [%] Instrument room relative humidity
 HUMID05 = 47.16 / [%] Control room relative humidity
 WINDSPD = 6.60 / [mph] Wind speed

WINDDIR = 158.66 / [deg] Wind direction
ATMPRESS= 767.55 / [mm Hg] Atmospheric pressure
COMMENT *****
COMMENT PCS PARAMETERS
COMMENT *****
DATE-PCS= '2017-03-08 00:33:52.1' / PCS sample date and time (UTC)
PACMD = 1000.4 / [mm Hg] Chamber A setpoint
PBCMD = 1000.6 / [mm Hg] Chamber B setpoint
PAMON = 753.7 / [mm Hg] Chamber A actual pressure
PBMON = 738.1 / [mm Hg] Chamber B actual pressure
PAERR = -246.7 / [mm Hg] Chamber A error
PBERR = -262.5 / [mm Hg] Chamber B error
PATEMP = 0. / [deg C] Chamber A temperature
PBTEMP = 0. / [deg C] Chamber B temperature
PALOOP = F / Chamber A loops closed?
PBLOOP = F / Chamber B loops closed?
END